REPUBLIC OF TÜRKİYE
YILDIZ TECHNICAL UNIVERSITY
GRADUATE SCHOOL OF SCIENCE AND ENGINEERING

IMPROVED MICROWAVE IMAGING OF NONLINEAR SCATTERERS USING HARMONIC RADAR AND MACHINE LEARNING

Onur ARI

DOCTOR OF PHILOSOPHY THESIS
Department of Electronics and Communication Engineering
Program of Communication

Supervisor
Prof. Dr. Ahmet KIZILAY

Co-supervisor
Assoc. Prof. Dr. Cüneyt UTKU

April, 2024

REPUBLIC OF TÜRKİYE
YILDIZ TECHNICAL UNIVERSITY
GRADUATE SCHOOL OF SCIENCE AND ENGINEERING

IMPROVED MICROWAVE IMAGING OF NONLINEAR SCATTERERS USING HARMONIC RADAR AND MACHINE LEARNING

A thesis submitted by Onur ARI in partial fulfillment of the requirements for the degree of **DOCTOR OF PHILOSOPHY** is approved by the committee on 16.04.2024 in Department of Electronics and Communication Engineering, Program of Communication.

Prof. Dr. Ahmet KIZILAY
Yildiz Technical University
Supervisor

Assoc. Prof. Dr. Cüneyt UTKU
TÜBİTAK BİLGEM
Co-supervisor

Approved By the Examining Committee

Prof. Dr. Ahmet KIZILAY, Supervisor
Yildiz Technical University _____

Prof. Dr. Nurhan TÜRKER TOKAN, Member
Yildiz Technical University _____

Prof. Dr. Mustafa Emre AYDEMİR, Member
Istanbul Arel University _____

Asst. Prof. Dr. Alper ÇALIŞKAN, Member
Yildiz Technical University _____

Asst. Prof. Dr. Necdet Tuğrul ARTUĞ , Member
Istanbul University-Cerrahpasa _____

I hereby declare that I have obtained the required legal permissions during data collection and exploitation procedures, that I have made the in-text citations and cited the references properly, that I haven't falsified and/or fabricated research data and results of the study and that I have abided by the principles of the scientific research and ethics during my Thesis Study under the title of Improved Microwave Imaging Of Nonlinear Scatterers Using Harmonic Radar and Machine Learning supervised by my supervisor, Prof. Dr. Ahmet KIZILAY. In the case of a discovery of false statement, I am to acknowledge any legal consequence.

Onur ARI

Signature

Dedicated to my family

ACKNOWLEDGEMENTS

To begin with, my advisors, Prof. Dr. Ahmet KIZILAY, and my co-advisor, Assoc. Prof. Dr. Cüneyt UTKU have my sincere gratitude for all of his time, help, suggestions, patience, and mentoring throughout the years. I especially want to express my gratitude to them for giving me fatherly guidance.

I will always be grateful to my family for their love and support as I pursue my education.

I would like to express my gratitude to my colleagues at TÜBİTAK BİLGEM and professors at Yıldız Technical University. I would like to thank my professors, Prof. Dr. Nurhan TÜRKER TOKAN and Prof. Dr. Mustafa Emre AYDEMIR, in my thesis committee for their time and advice.

Onur ARI

TABLE OF CONTENTS

LIST OF SYMBOLS viii

LIST OF ABBREVIATIONS x

LIST OF FIGURES xii

LIST OF TABLES xviii

ABSTRACT xix

ÖZET xxi

1 INTRODUCTION 1

1.1 Literature Review 1

1.2 Objective of the Thesis 3

1.3 Hypothesis 4

2 THE FUNDAMENTALS OF NONLINEAR RADARS 6

2.1 Nonlinear Behavior of System and Harmonic Generation Mechanisms 7

2.2 Derivation of Nonlinear Radar Equation and Nonlinear Cross Section 9

3 DEVELOPMENT OF HARMONIC BEAMFORMING MEASUREMENT SYSTEM 14

3.1 Transmitter Front-End Components and Operational Mechanism . . 14

3.1.1 Oscilloscope Based Harmonic Radar Measurement System . 15

3.1.2 Sofware-Defined Radio (SDR) Based Harmonic Radar Measurement System 18

3.2 Receiver Front-End Components and Operational Mechanism . . . 21

3.3 Innovative Antenna Design for Enhanced Harmonic Beamforming Performance 24

3.4 Mechanical Design Considerations for Harmonic Beamforming Systems 36

4 MICROWAVE IMAGING AND ADAPTIVE BEAMFORMING TECHNIQUES 39

4.1 Delay and Sum Algorithm (DSB) 41
4.2 Capon Algorithm (SCB) 47
4.3 The Robust Capon Algorithm (RCB) 57
4.4 Radial Basis Function Neural Network (RBFNN) 63
4.4.1 RBFNN Based 1-D Beamforming Pattern Simulations and Results 65
4.5 Discussion 72

5 EXPERIMENTAL RESULTS AND DISCUSSION 73
5.1 HBF Image Construction 73
5.2 Experimental Analysis of Microwave Imaging for Nonlinear Scatterers Using Conventional Beamformer Techniques 77
5.2.1 Measurement-1 78
5.2.2 Measurement-2 80
5.2.3 Measurement-3 81
5.2.4 Measurement-4 83
5.2.5 Measurement-5 84
5.2.6 Measurement-6 85
5.2.7 Measurement-7 87
5.2.8 Measurement-8 88
5.2.9 Summary of Conventional Beamformer 2-D Image Formation Result 89
5.3 Experimental Studies on RBFNN Based Microwave Imaging of Nonlinear Scatterers 90
5.3.1 Measurement-1 92
5.3.2 Measurement-2 94
5.3.3 Measurement-3 95
5.3.4 Measurement-4 96
5.3.5 Measurement-5 97
5.3.6 Measurement-6 99
5.3.7 Measurement-7 100
5.3.8 Measurement-8 101
5.3.9 Summary of 2-D DSB and RBFNN Based Image Formation Results 103
5.4 Image Formation Timing Analysis of Conventional and Neural Network Based Beamformers 103
5.4.1 Summary of 2-D Conventional and RBFNN Based Beamformer Timing Results 108

6 CONCLUSION 110

REFERENCES **113**

PUBLICATIONS FROM THE THESIS **119**

LIST OF SYMBOLS

α, β	Arbitrary constants
d	Array Element spacing
ω	Angular frequency
$\mathbf{w}$	Beamforming weights
d	Characteristic length
$\mathbf{R}$	Covariance matrix
I	Current
$\boldsymbol{\varphi}$	Design matrix of RBFNN
θ	Direction of arrival
E	Electric field
$E(\theta, \phi)$	Element pattern
$\boldsymbol{f}_{n\omega}$	Far-field vector pattern of antenna
$\mathbf{s}_f$	Focusing vector
$H(f)$	Frequency response
f_0	Fundamental frequency
$\mathbf{I}$	Identity matrix
$\hat{\boldsymbol{\kappa}}$	Input matrix of RBFNN
a_n, b_n	Linear coefficients
L	Linear system operator
σ'	Modified linear RCS
σ_n	Nonlinear radar cross section (RCS)
$\boldsymbol{\kappa}$	Normalized input matrix of RBFNN
M	Number of array elements

δ_x	Number of pixel on x-axis
δ_z	Number of pixel on z-axis
P	Number of pixel on scanning area
$\boldsymbol{d}$	Output matrix of RBFNN
$y(t)$	Output signal
y_1, y_2	Output signals
$P(\theta)$	Power pattern
$\boldsymbol{\varphi}^{\dagger}$	Pseudo-inverse of RBFNN design matrix
$x(t)$	Received signal
G_r	Receive antenna gain
δ	Regularization scalar
$\mathbf{R}_{\text{robust}}$	Robust Capon covariance matrix
A	Signal amplitude
c	Speed of light
$\mathbf{a}(\theta)$	Steering vector
G_t	Transmit antenna gain
P_t	The transmitted power of the radar signal
λ	Wavelength
$\mathbf{w}_{\text{MVDR}}$	Weight vector for MVDR

LIST OF ABBREVIATIONS

1-D	One Dimensional
2-D	Two Dimensional
AOA	Angle of Arrival
DSB	Delay and Sum Algorithm
DOA	Direction of Arrival
DSP	Digital Signal Processing
FMCW	Frequency-Modulated Continuous-Wave
FPGA	Field-Programmable Gate Array
HBF	Harmonic Beamforming
HPA	High-power Amplifier
HPBW	Half Power Beamwidth
HRCS	Harmonic Radar Cross Section
HSAR	Harmonic Synthetic Aperture Radar
MUSIC	Multiple Signal Classification
NN	Neural Network
NLS	Nonlinear scatterer
RCB	Robust Capon Algorithm
RBF	Radial Basis Function
RBFNN	Radial Basis Function Neural Network
RBFNN-RCB	RCB Based RBFNN
RBFNN-SCB	SCB Based RBFNN
RCS	Radar Cross Section
SAR	Synthetic Aperture Radar

SCB	Standard Capon (MVDR) Algorithm
SLL	Side Lobe Level
SNR	Signal to Noise Ratio
TOI	Targets of Interest

LIST OF FIGURES

Figure 2.1 Nonlinear behavior of the diode 7
Figure 2.2 Harmonic response of a nonlinear target 8
Figure 2.3 Illusration of harmonic response of a high power amplifier (HPA) 8
Figure 2.4 Nonlinear scatterers and harmonic radar illustration 10
Figure 2.5 The comparison of received power P_{rn} and Range R 13
Figure 3.1 Harmonic beamforming measurement system 1 block diagram . 15
Figure 3.2 HBF measurement system 1 16
Figure 3.3 The transmitter block output power at 2.4 GHz 17
Figure 3.4 The measurement of the S21 result of cavity filter 17
Figure 3.5 Harmonic beamforming measurement system 2 block diagram . 18
Figure 3.6 Blade RF xA4 19
Figure 3.7 Blade RF xA4 block diagram [28] 20
Figure 3.8 Harmonic beamforming measurement system 2 and motor-controlled scanning system 21
Figure 3.9 One VHF 4400 (left) and two VHF 4400 (right) S21 measurement results 22
Figure 3.10 Measurement system schematic 22
Figure 3.11 Receiver channel measured gain (top), the measured result of the 2.4 GHz at output port of the receive channel when the input power of 0 dB at 2.4 GHz (below) 23
Figure 3.12 S21 measured result of the cavity filter placed on receiver block 24
Figure 3.13 (a) Simulation model of the SEMVA (b) Evolution model of the all-metal Vivaldi antenna; reference model, slotted edge model, and *Rexolite* inserted slotted edge model, respectively. 25
Figure 3.14 a) The current distribution of proposed antenna b) real and imaginary part of the proposed antennas 27
Figure 3.15 Measured and simulated reflection coefficient results (b) Group delay measurement setup and results of the proposed antenna . 29
Figure 3.16 (a) Rogers MWI-2019 calculation parameters (b) E-field distribution of the proposed antenna at 8GHz 31
Figure 3.17 Radiation pattern measurement setup of the SEMVA inside the spherical near field chamber. 32

Figure 3.18 Comparison of Simulated and Measured Antenna Radiation Patterns at 1.5 GHz, 2 GHz, 8 GHz, and 12 GHz 33
Figure 3.19 The proposed antenna gain comparison 34
Figure 3.20 Perspective view of the mechanical design model of the HBF scanning system 37
Figure 3.21 Constructed HBF scanning system 37
Figure 3.22 Step motor integration 38
Figure 3.23 HBF-2 system mechanical switch 38
Figure 4.1 N-th element array arriving signals 39
Figure 4.2 DSB beam pattern for a single source signal at 30° with SNR level of 0 dB (top), DSB beam patterns for three uncorrelated signals for -50°, 0°, and 30° degree at SNR level of 0 dB, respectively (bottom) 42
Figure 4.3 Beamforming result with 0 dB SNR from -10°-0°-10° angles . 43
Figure 4.4 DSB beam pattern for a single source signal at 30° with SNR level of 5 dB (top), DSB beam patterns for three uncorrelated signals for -50°, 0°, and 30° degree at SNR level of 5 dB, respectively (bottom) 43
Figure 4.5 Beamforming result with 5 dB SNR from -10°-0°-10° angles . 44
Figure 4.6 DSB beam pattern for a single source signal at 30° with SNR level of 10 dB (top), DSB beam patterns for three uncorrelated signals for -50°, 0°, and 30° degree at SNR level of 10 dB, respectively (bottom) 45
Figure 4.7 Beamforming result with 10 dB SNR from -10°-0°-10° angles 45
Figure 4.8 DSB beam pattern for a single source signal at 30° with SNR level of 20 dB (top), DSB beam patterns for three uncorrelated signals for -50°, 0°, and 30° degree at SNR Level of 20 dB, respectively (bottom) 46
Figure 4.9 Beamforming result with 20 dB SNR from -10°-0°-10° angles 47
Figure 4.10 SCB beam pattern for a single source signal at 30° with SNR level of 0 dB (top), SCB beam patterns for three uncorrelated signals for -50°, 0°, and 30° degree at SNR level of 0 dB, respectively (bottom) 51
Figure 4.11 Beamforming result with 0 dB SNR from -10°-0°-10° angles . 52
Figure 4.12 SCB beam pattern for a single source signal at 30° with SNR level of 5 dB (top), SCB beam patterns for three uncorrelated signals for -50°, 0°, and 30° degree at SNR level of 5 dB, respectively (bottom) 53
Figure 4.13 Beamforming result with 5 dB SNR from -10°-0°-10° angles . 53

Figure 4.14 SCB beam pattern for a single source signal at 30° with SNR level of 10 dB (top), SCB beam patterns for three uncorrelated signals for -50°, 0°, and 30° degree at SNR level of 10 dB, respectively (bottom) 54
Figure 4.15 Beamforming result with 10 dB SNR from -10°-0°-10° angles 55
Figure 4.16 SCB beam pattern for a single source signal at 30° with SNR level of 20 dB (top), SCB beam patterns for three uncorrelated signals for -50°, 0°, and 30° degree at SNR level of 20 dB, respectively (bottom) 56
Figure 4.17 Beamforming result with 20 dB SNR from -10°-0°-10° angles 56
Figure 4.18 RCB beam pattern for a single source signal at 30° with SNR level of 0 dB (top), RCB beam patterns for three uncorrelated signals for -50°, 0°, and 30° degree at SNR level of 0 dB, respectively (bottom) 58
Figure 4.19 RCB Beamforming result with 0 dB SNR from -10°-0°-10° angles 59
Figure 4.20 RCB beam pattern for a single source signal at 30° with SNR level of 5 dB (top), RCB beam patterns for three uncorrelated signals for -50°, 0°, and 30° degree at SNR level of 5 dB, respectively (bottom) 60
Figure 4.21 RCB Beamforming result with 5 dB SNR from -10°-0°-10° angles 60
Figure 4.22 RCB beam pattern for a single source signal at 30° with SNR level of 10 dB (top), RCB beam patterns for three uncorrelated signals for -50°, 0°, and 30° degree at SNR level of 10 dB, respectively (bottom) 61
Figure 4.23 RCB Beamforming result with 10 dB SNR from -10°-0°-10° angles 62
Figure 4.24 RCB beam pattern for a single source signal at 30° with SNR level of 20 dB (top), RCB beam patterns for three uncorrelated signals for -50°, 0°, and 30° degree at SNR level of 20 dB, respectively (bottom) 62
Figure 4.25 RCB Beamforming result with 20 dB SNR from -10°-0°-10° angles 63
Figure 4.26 The architecture of RBFNN [56] 64
Figure 4.27 The one-dimensional uniform linear array structure 65

Figure 4.28 RBFNN beam pattern for a single source signal at 30° with SNR level of 0 dB (top), RBFNN beam patterns for three uncorrelated signals for -50°, 0°, and 30° degree at SNR level of 0 dB, respectively (bottom) 67
Figure 4.29 RBFNN Beamforming result with 0 dB SNR from -10°-0°-10° angles 67
Figure 4.30 RBFNN beam pattern for a single source signal at 30° with SNR level of 5 dB (top), RBFNN beam patterns for three uncorrelated signals for -50°, 0°, and 30° degree at SNR level of 5 dB, respectively (bottom) 68
Figure 4.31 RBFNN Beamforming result with 5 dB SNR from -10°-0°-10° angles 69
Figure 4.32 RBFNN beam pattern for a single source signal at 30° with SNR level of 10 dB (top), RBFNN beam patterns for three uncorrelated signals for -50°, 0°, and 30° degree at SNR level of 10 dB, respectively (bottom) 69
Figure 4.33 RBFNN Beamforming result with 10 dB SNR from -10°-0°-10° angles 70
Figure 4.34 RBFNN beam pattern for a single source signal at 30° with SNR Level of 10 dB (top), RBFNN beam patterns for three uncorrelated signals for-50°, 0°, and 30° degree at SNR level of 20 dB, respectively (bottom) 71
Figure 4.35 RBFNN Beamforming result with 20 dB SNR from -10°-0°-10° angles 71
Figure 5.1 Imaging of nonlinear scatterer with synthesized uniform linear array 74
Figure 5.2 Nonlinear scatterers used in measurements 78
Figure 5.3 NLS-1 placement on styrofoam 79
Figure 5.4 HBF results with image formation algorithm from NLS-1 at x=0cm, y=84.5cm, z=197cm 79
Figure 5.5 The placement of the NLS-1 and an aluminium pipe in the scanning area 80
Figure 5.6 HBF results with image formation algorithm from NLS-1 at x=-17.5cm, y=84.5cm, z=118cm 81
Figure 5.7 The placement of the NLS-2 in the scanning area 82
Figure 5.8 HBF results with image formation algorithm from NLS-2 at x=0cm, y=84.5cm, z=144cm 82
Figure 5.9 The placement of the NLS-1 in the scanning area for measurement-4 83

Figure 5.10 HBF results with image formation algorithm from NLS-1 at x=3cm, y=84.5cm, z=118cm 83
Figure 5.11 The placement of the NLS-1 in the scanning area for measurement-5 84
Figure 5.12 HBF results with image formation algorithm from NLS-3 at x=-20 cm, y=86 cm, z=130 cm 85
Figure 5.13 The placement of the NLS-3 and RCS-2 in the scanning area for measurement-6 86
Figure 5.14 HBF results with image formation algorithm from NLS-3 at x=-20 cm, y=86 cm, z=130 cm 86
Figure 5.15 The placement of the NLS-1 in the scanning area for measurement-7 87
Figure 5.16 HBF results with image formation algorithm from NLS-1 at x=10cm, y=86cm, z=130cm 88
Figure 5.17 The placement of the NLS-1 in the scanning area for measurement-8 88
Figure 5.18 HBF results with image formation algorithm from NLS-1 at x=-20 y=88 z=130cm 89
Figure 5.19 Measurement area of scenario-1 and NLS-1 at x=0 y=84.5 z=197cm 93
Figure 5.20 HBF Imaging Comparisons: DSB (Left), SCB (Mid) and RCB (Right) Trained RBFNN Beamformers Analyzing NLS-1 at coordinates x=0, y=84.5, z=197 cm 93
Figure 5.21 Measurement area of scenario-2 and NLS-1 and RCS-1 at x=-17.5 y=84.5 z=118 cm 94
Figure 5.22 HBF Imaging Comparisons: DSB (Left), SCB (Mid) and RCB (Right) Trained RBFNN Beamformers Analyzing NLS-1 and RCS-1 at coordinates x=-17.5, y=84.5, z=118 cm 94
Figure 5.23 Measurement area of scenario-3 and NLS-2 at x=0 y=84.5 z=144 cm 95
Figure 5.24 HBF Imaging Comparisons: DSB (Left), SCB (Mid) and RCB (Right) Trained RBFNN Beamformers Analyzing NLS-2 at coordinates x=0, y=84.5, z=144 cm 96
Figure 5.25 Measurement area of scenario-4 and NLS-1 at x=0 y=84.5 z=118 cm 96
Figure 5.26 HBF Imaging Comparisons: DSB (Left), SCB (Mid) and RCB (Right) Trained RBFNN Beamformers Analyzing NLS-1 at coordinates x=0, y=84.5, z=118 cm 97

Figure 5.27 Measurement area of scenario-5 and NLS-3 at at x=-20 y=86 z=130cm 98
Figure 5.28 HBF Imaging Comparisons: DSB (Left), SCB (Mid) and RCB (Right) Trained RBFNN Beamformers Analyzing NLS-3 at coordinates x=-20, y=86, z=130 cm 98
Figure 5.29 Measurement area of scenario-6 and NLS-3 and RCS-2 at x=-20 y=86 z=130cm 99
Figure 5.30 HBF Imaging Comparisons: DSB (Left), SCB (Mid) and RCB (Right) Trained RBFNN Beamformers Analyzing NLS-3 and RCS-2 at coordinates x=-20, y=86, z=130 cm 100
Figure 5.31 Measurement area of scenario-7 and NLS-3 at x=10 y=86 z=130cm 100
Figure 5.32 HBF Imaging Comparisons: DSB (Left), SCB (Mid) and RCB (Right) Trained RBFNN Beamformers Analyzing NLS-1 at coordinates x=10, y=86, z=130 cm 101
Figure 5.33 Measurement area of scenario-8 and NLS-1 at x=-20 y=86 z=130cm 102
Figure 5.34 HBF Imaging Comparisons: DSB (Left), SCB (Mid) and RCB (Right) Trained RBFNN Beamformers Analyzing NLS-1 at coordinates x=-20, y=86, z=130 cm 102

LIST OF TABLES

Table 3.1 Antenna design parameters 25
Table 3.2 Performance comparison of the Vivaldi antennas 35
Table 5.1 Scenario-1 timing results of the beamformers 104
Table 5.2 Scenario-2 timing results of the beamformers 105
Table 5.3 Scenario-3 timing results of the beamformers 105
Table 5.4 Scenario-4 timing results of the beamformers 106
Table 5.5 Scenario-5 timing results of the beamformers 106
Table 5.6 Scenario-6 timing results of the beamformers 107
Table 5.7 Scenario-7 timing results of the beamformers 107
Table 5.8 Scenario-8 timing results of the beamformers 108

ABSTRACT

Improved Microwave Imaging Of Nonlinear Scatterers Using Harmonic Radar and Machine Learning

Onur ARI

Department of Electronics and Communication Engineering
Doctor of Philosophy Thesis

Supervisor: Prof. Dr. Ahmet KIZILAY
Co-supervisor: Assoc. Prof. Dr. Cüneyt UTKU

This thesis examines the potential of synthetic aperture harmonic radar technology for identifying nonlinear scatterers and conducting microwave imaging. The research focuses on the emission properties of harmonic frequency components from nonlinear components such as diodes, transistors, amplifiers, and mixers. When illuminated by radio frequency signals, these components exhibit nonlinear scattering properties caused by p-n junctions. This property enables harmonic radar systems to distinguish signals from nonlinear sources from those of naturally occurring objects and to effectively suppress linear clutter. Another major challenge in harmonic radar systems requires a high-power radio frequency signal to achieve a high signal-to-noise ratio and produce a clean, harmonic-free fundamental signal. Therefore, a band-pass filter that suppresses the harmonic components of the fundamental frequency is required in the transmitter channel.

A single-tone narrowband software-defined radio-based harmonic synthetic aperture radar system is developed for detailed experimental microwave imaging of nonlinear scatterers. In order to synthesize uniform linear array, the computer-controlled motorized mechanical structure of the radar system has been carefully optimized to achieve an optimal balance between resolution, scanning speed, and accuracy. This harmonic microwave imaging system is an innovative approach to microwave harmonic imaging that provides one-dimensional scanning in the near-field region and two-dimensional mapping.

In the development of image formation techniques to identify and localize nonlinear scatterers, the delay and sum algorithm and the more advanced Capon and Robust Capon algorithms have been employed. Furthermore, this work presents an important innovation that involves the integration of these algorithms with a Radial Basis Function Neural Network (RBFNN) structure to improve the beamforming process. Several experimental studies have been conducted under eight different scenarios using three different nonlinear scatterers and two linear Radar Cross-section (RCS) targets. These extensive tests and analyses have successfully formed 2-D images of the nonlinear scatterers with data collected from the near-field of the beamforming system. The images have been analyzed and interpreted regarding key performance parameters, including resolution, localization, accuracy, and noise suppression capability. This performance evaluation process is critical in determining the efficiency and accuracy of the imaging process. In addition to the performance parameters, radial basis neural networks trained with standard Capon and Robust Capon algorithms have been compared with conventional beamforming methods in terms of image formation time, and the findings obtained as a result of these comparisons have been evaluated.

Keywords: Harmonic radar, microwave imaging, nonlinear scatterers, nonlinear radar, nearfield microwave imaging, neural networks

ÖZET

Harmonik Radar ve Makine Öğrenmesi Kullanılarak Doğrusal Olmayan Saçıcıların Geliştirilmiş Mikrodalga Görüntülemesi

Onur ARI

Elektronik ve Haberleşme Mühendisliği Ana Bilim Dalı
Doktora Tezi

Danışman: Prof. Dr. Ahmet KIZILAY
Eş-Danışman: Doç. Dr. Cüneyt UTKU

Bu tez, sentetik açıklıklı harmonik radar teknolojisini kullanarak doğrusal olmayan saçıcıların tespiti ve mikrodalga görüntüleme potansiyelini incelemektedir. Araştırma, diyotlar, transistörler, amplifikatörler ve mikserler gibi doğrusal olmayan bileşenlerin harmonik frekans bileşenlerinin yayılım özelliklerine odaklanmaktadır. Radyo frekansı sinyalleriyle aydınlatıldığında, bu bileşenler p-n bağlantıları nedeniyle doğrusal olmayan saçılma özellikleri gösterir. Bu özellik, harmonik radar sistemlerinin doğrusal olmayan kaynaklardan gelen işaretleri doğal olarak oluşan nesnelerden gelen işaretlerden ayırt etmesini ve doğrusal parazitleri etkin bir şekilde bastırmasını sağlar. Harmonik radar sistemlerinde karşılaşılan bir diğer önemli zorluk da yüksek bir sinyal-gürültü oranı elde edebilmek için yüksek güçlü bir radyo frekansı sinyaline ve harmonik içermeyen temiz bir temel sinyal üretimine ihtiyaç duyulmasıdır. Bu nedenle verici kanalında temel frekansın harmonik bileşenlerini bastıran bir filitre gerekmektedir.

Doğrusal olmayan saçıcıların detaylı deneysel mikrodalga görüntülemesi için tek tonlu dar bantlı bir yazılım tanımlı radyo tabanlı harmonik sentetik açıklıklı radar sistemi geliştirilmiştir. Düzgün bir doğrusal dizi sentezlemek için, radar sisteminin bilgisayar kontrollü motorlu mekanik yapısı, çözünürlük, tarama hızı ve doğruluk arasında optimum bir denge elde etmek için dikkatlice optimize edilmiştir.

Bu harmonik mikrodalga görüntüleme sistemi, yakın alan bölgesinde tek boyutlu tarama sağlamanın yanı sıra, iki boyutlu haritalama sunan mikrodalga harmonik görüntülemede yenilikçi bir yaklaşımdır.

Doğrusal olmayan saçıcıları tanımlamak ve lokalize etmek için geliştirilen görüntü oluşturma tekniklerinde, gecikme ve toplama algoritması ile daha gelişmiş Capon ve Robust Capon algoritmaları kullanılmıştır. Ayrıca, bu çalışma, hüzmeleme sürecini iyileştirmek için bu algoritmaların bir Radyal Tabanlı Fonksiyon Sinir Ağı (RBFNN) yapısı ile entegrasyonunu içeren önemli bir yeniliği sunmaktadır. Üç farklı doğrusal olmayan saçıcı ve iki doğrusal Radar Kesit Alanı (RCS) hedefi kullanılarak sekiz farklı senaryo altında bir dizi deneysel çalışma yürütülmüştür. Bu kapsamlı test ve analizler, hüzmeleme sistemimizin yakın alanından toplanan verilerle doğrusal olmayan saçıcıların 2-D görüntülerinin başarıyla oluşturulmasını sağlamıştır. Görüntüler, çözünürlük, lokalizasyon, doğruluk ve gürültü bastırma yeteneği gibi temel performans parametreleri açısından analiz edilmiş ve yorumlanmıştır. Bu performans değerlendirme süreci, görüntüleme işleminin verimliliği ve doğruluğunu belirlemede hayati öneme sahiptir. Performans parametrelerine ek olarak, standart Capon ve Robust Capon algoritmaları ile eğitilen radyal tabanlı sinir ağlarının görüntü oluşum süresi açısından geleneksel hüzmeleme yöntemleriyle karşılaştırılması yapılmış ve bu karşılaştırmalardan elde edilen bulgular değerlendirilmiştir

Anahtar Kelimeler: Harmonik radar, mikrodalga görüntüleme, doğrusal olmayan saçıcılar, yakın alan mikrodalga görüntüleme, yapay sinir ağları

1
INTRODUCTION

1.1 Literature Review

Harmonic radar can detect and identify active and passive characteristics of nonlinear scatterers. It receives only harmonics of the fundamental signal. Most natural objects do not have nonlinear behavior; therefore, its strong clutter suppression allows this technique to be used in many fields, such as insect tracking by entomologists [1, 2], vital sign monitoring [3], temperature sensing at a fixed distance [4, 5], corrosion measurement [6], and search and rescue operations [7] [8]. Furthermore, harnessing the reflections of harmonic frequencies plays a vital role in applications ranging from security to diagnostics, enabling detailed mapping of hidden electronic targets [9].

The initial utilization of harmonic radar can be traced back to 1973. Klensch [10] designed and implemented an anti-collusion harmonic radar system on the vehicle. In 2013, Mazarro presented [11] nonlinear radar that transmits multiple frequencies and receives a harmonics of these frequencies, and other intermodulation frequencies close to this harmonic were presented. This radar transmits several closely spaced tones and receives harmonics and nonlinear mixture products. The experimental results show that the radar system has the ability to suppress linear clutter and distinguish nonlinear components. Furthermore, a novel closely-spaced two-tone pulsed harmonic radar system has also been developed to detect concealed electronics [12]. This work also presents a novel method to discriminate between electronic targets using at least two nonlinear mixture products received near a harmonic. A novel two-tone harmonic radar system has been experimentally validated, and the results have been used to achieve practical standoff ranges.

Later, the studies conducted at the United States Army Research Laboratory (ARL) include the results of short-range airborne harmonic radar tests and address the development of nonlinear radar [13]. This study uses the inverse Fourier transform

of the nonlinear frequency response to determine the range of nonlinear targets. Moreover, Mazarro et al. [14] proposed an ultra-wideband harmonic radar system to detect and localize nonlinear (electronic) targets in two-dimensional stationary positions. In this method, ranging is performed by scanning the transmit frequencies between 700-900 MHz up to 2W RF signal power, capturing the amplitude and phase of the harmonic return signal, and calculating the inverse Fourier transform of the broadband harmonic response of the 3 different targets.

Besides the detection and identification of nonlinear properties of the targets, harmonic radar microwave imaging and localization techniques have witnessed a notable expansion in recent years. Synthetic aperture radar systems have been used in many fields like remote sensing, orbital observation, mapping, and monitoring due to their ability to produce high-resolution images of targets. In the last decade, harmonic beamforming or synthetic aperture-based imaging has gained significant attention, but only a few systems have been proposed. Berger and Hamran [15] utilized the frequency-modulated continuous wave (FMCW) technique in harmonic radar systems. This study presented conventional SAR techniques for harmonic radar systems, but there is a noticeable lack of experimental studies. Bischeltsrieder et al. [16] introduced a 2-D imaging system employing the harmonic synthetic aperture technique in 2019. A new signal processing algorithm for harmonic radar imaging and developing a dual-mode measurement system combining conventional and harmonic radar methods is demonstrated. This research enhances the near-field array systems with a robust Capon-based imaging algorithm that extends the imaging quality beyond the capabilities of the harmonic radar system. The constructed harmonic synthetic aperture system utilizes the frequency difference between radar waves illuminating and reflected from electromagnetically nonlinear targets. In 2023, Shi et al. [17] investigated the influence of spatial variation along the range dimension on the harmonic synthetic aperture system. A novel spatial variation compensation imaging algorithm has been proposed to overcome spatial variation along the measurement range. In 2017, Gallagher et al. [18] developed a harmonic radar system to demonstrate the imaging capabilities of a moving nonlinear target and the suppression of echo signals from linear targets experimentally. This study uses a transmitter frequency of 800-1000 MHz step frequency with 40 dB RF signal power for imaging and positioning of moving nonlinear targets. The imaging and localization of the moving nonlinear scatterer were achieved by measuring the Doppler shift of the RF signal at the second harmonic fundamental frequency. In addition to the Doppler studies mentioned above, Hilton et al. [19] have studied frequency-selective RF tags for harmonic Doppler radar tracking. This study uses narrowband split ring PCB antennas and

a diode to generate a second harmonic of the incident fundamental frequency. The designed tags function as a fractional narrowband antenna. Thus, an additional circuit need has been eliminated. 2.4/4.8 GHz RF frequencies have been used to validate the effectiveness of the proposed system.

In order to identify and discriminate the nonlinear characteristics of the target, Ilbegi et al. [20] have developed a new approach for harmonic radar systems. The transmitted single-tone signal power has been swept within the determined range in order to reveal the nonlinear characteristic depending on the RF signal power,

Ragira [21] has stated that the harmonic radar should avoid interference that can saturate RF components and cause self-induced harmonics by directing RF components into nonlinear operating regions. In addition, a radar design for target detection at a given distance range with multi-tone harmonic radar is also presented. The work of Mishra et al. [22] deals with the design of a third-order harmonic radar for mm-wave frequencies. This nonlinear property produces a third-order harmonic response for clutter rejection.

In 2022, Oh et al. [23] conducted a comprehensive experimental analysis of various electronic devices' nonlinear radar cross section. These analyses involve using a nonlinear radar capable of detecting nonlinear responses (i.e., harmonics and intermodulation) scattered by electronic devices.

1.2 Objective of the Thesis

The primary objective of this thesis is to examine and enhance the capacities of the capabilities of detection and imaging of near-field nonlinear scatterers using harmonic beamforming systems (a.k.a HBF), with a particular focus on harmonic radar methodologies. This study involves the use of applying advanced beamforming techniques which are commonly employed in linear radars, like delay and sum, capon, and robust capon algorithms.

In order to improve the efficiency and reduce the need for hardware requirements of the measurement system, a narrowband single-tone continuous wave signal technique is used in this thesis. Furthermore, the thesis introduces a radial-based artificial neural network as a new beamforming approach for microwave imaging of a nonlinear target. This method simplifies the computational complexity typically associated with beamforming algorithms and enables faster adaptation to dynamic environments.

The work extends its applicability to practical scenarios, including experiments where targets are placed on styrofoam or ABS material in an aerial environment to simulate the imaging scenarios. This thesis also addresses the technical challenges of integrating advanced imaging algorithms and hardware into these contexts. It critically examines the issues arising from the combination of these sophisticated technologies.

The significant contribution of this thesis lies in the development of near-field harmonic radar imaging systems. Addressing both theoretical and practical aspects lays the groundwork for future innovations in microwave imaging.

1.3 Hypothesis

This thesis delves into both theoretical and experimental studies to achieve high-resolution and accurate 2-D imaging of nonlinear scatterers placed in the near field of an antenna array using a synthetic aperture radar (SAR) based system. The main objective is to explore whether high-resolution imaging of nonlinear scatterers is feasible and to identify the most effective techniques in this process. The study presented here shows that using the harmonic beamforming technique to obtain 2-D images of nonlinear scatterers can significantly enhance the detection capabilities of nonlinear scatterers within harmonic radar technology.

Furthermore, alternative developed systems based on harmonic radar principles offer wideband radar systems with complex and costly hardware requirements. In this context, developing a software-defined radio-based RF transceiver structure could replace the need for signal generators and oscilloscopes and pave the way for simpler hardware requirements and more cost-effective radar solutions. This would make the system more compact, efficient, and cost-effective and widen its use in field operations.

Conventional beamforming algorithms such as Delay-and-Sum, Standard Capon, and Robust Capon, frequently used in microwave imaging techniques, will be tested by integrating them into the harmonic beamformer system. It will be shown that integrating these methods can be effectively used to generate high precision, high resolution, and clutter-suppressed images of nonlinear scatterers using the principle of harmonic beamforming measurement system. This method is predicted to provide better 2D imaging of nonlinear scatterers by efficiently combining the advantages of established beamforming techniques.

Due to the inherent computational complexity, long computation and image generation time of Capon-based beamformer structures, it becomes imperative to focus on an alternative beamformer structure for real-time application needs. In recent years, neural network-based computing has emerged as a promising technique for radar image processing applications. In this work, a new beamformer structure based on the radial basis function neural network (RBFNN) technology framework is predicted to significantly reduce the 2-D image generation time of systems trained with Capon-based beamforming algorithms and to be an important step in accelerating radar imaging processes. The nonlinear microwave imaging system and beamformer structure developed in this thesis are expected to provide high resolution, accuracy, and localization. It is expected to contribute to developing faster and more effective nonlinear scatterer imaging solutions, especially in changing environments.

2
THE FUNDAMENTALS OF NONLINEAR RADARS

Harmonic radar is a specialized radar system that works by transmitting a signal and then receiving the harmonic reflections of this signal, which are usually multiples of the fundamental frequency of the transmitted signal. Nonlinear radars differ from linear radar by high clutter rejection, channel isolation, receiver sensitivity, harmonic-free fundamental signals, and required power to emit harmonics from nonlinear scatterers. In order to understand the nonlinearity, the input and output relations of the system need to be understood. A linear system can be depicted as a scaled derivative of the output data to the input data [24].

$$y_1 = L\{x_1\} \tag{2.1}$$

$$y_2 = L\{x_2\} \tag{2.2}$$

$$L\{\alpha x_1 + \beta x_2\} = \alpha y_1 + \beta y_2 \tag{2.3}$$

In this context, $L\{x_1\}$ represents the operation of a linear system on an input signal x_1 yielding an output y_1, $L\{x_2\}$ is the same linear system operating on input x_2 with the output equal to y_2, and α and β are arbitrary constants. Nonlinear systems are defined by their inability to conform to this principle of linearity.

Herein, $L\{x_1\}$ and the $L\{x_2\}$ is a linear system that operating on a signal x_1 and x_2 respectively. α and β are arbitrary constants. These linear systems output equals y_1 and y_2 respectively. Notably, nonlinear system behavior does not contain this type of linearity.

2.1 Nonlinear Behavior of System and Harmonic Generation Mechanisms

Once the behavior of a nonlinear structure needs to be examined, the current-voltage graph of the diode provides a practical way to understand the nonlinear behavior, as shown in Figure 2.1.

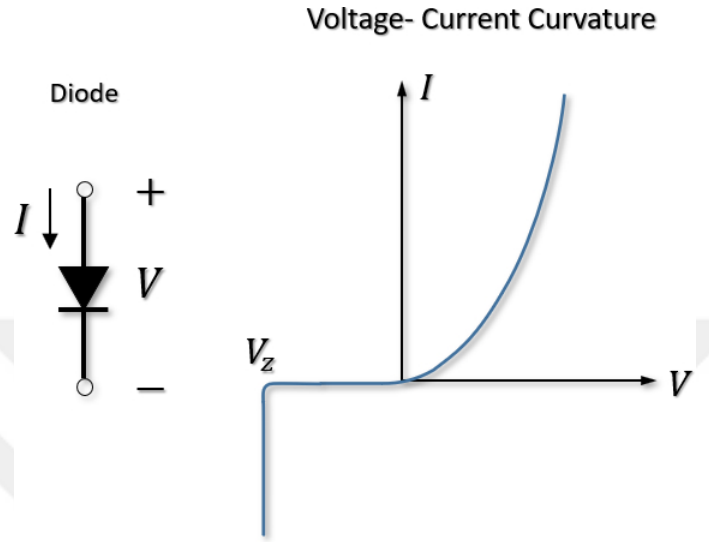


Figure 2.1 Nonlinear behavior of the diode

When the voltage V exceeds the threshold voltage V_z, the current I can be expressed as a power series. In (2.4), it summarizes that when the threshold voltage, V_z, has been exceeded, the nonlinearity increases by current.

$$I = a_1 V + a_2 V^2 + a_3 V^3 + \dots \tag{2.4}$$

The voltage difference (V) can be created by means of a remotely sensed electric field (E). d is a characteristic length between terminals

$$V = Ed \tag{2.5}$$

Current - Electric Field Relationship is given by;

$$I = b_1 E + b_2 E^2 + b_3 E^3 + \dots \tag{2.6}$$

As illustrated in Figure 2.2, the harmonic currents and electric field of the emitted electromagnetic waves must be understand to predict the reflected response of a

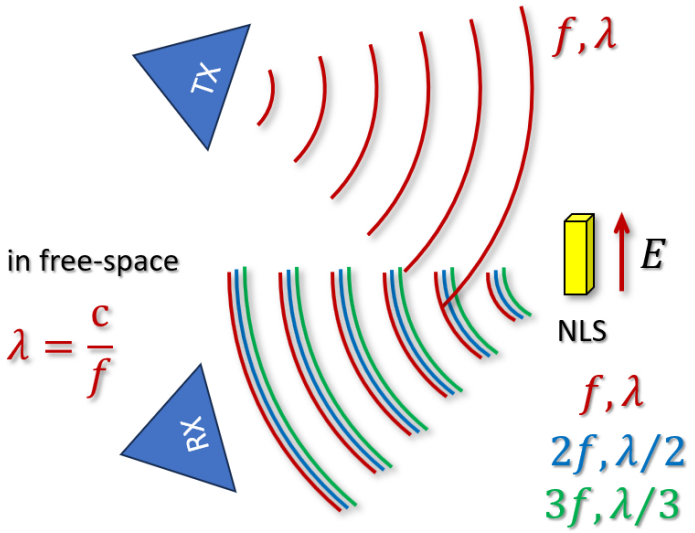


Figure 2.2 Harmonic response of a nonlinear target

nonlinear target to incident RF radiation. The harmonic expression of the current is given as;

$$I = b_1 E + b_2 E^2 + b_3 E^3 + \dots \tag{2.7}$$

$$I = b_1 E_0 \cos(2\pi f t + \theta) + b_2 E_0^2 \cos^2(2\pi f t + \theta) + b_3 E_0^3 \cos^3(2\pi f t + \theta) + \dots \tag{2.8}$$

Thus, (2.8) yields;

$$I = \beta_0 + \beta_1 \cos(2\pi f t + \theta) + \beta_2 \cos(2\pi (2f) t + 2\theta) + \beta_3 \cos(2\pi (3f) t + 3\theta) + \dots \tag{2.9}$$

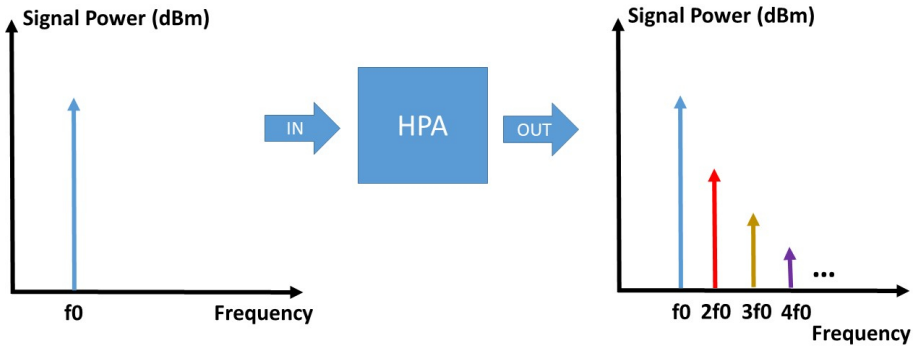


Figure 2.3 Illusration of harmonic response of a high power amplifier (HPA)

According from Figure 2.3, when single frequency RF signal applied to the input port of the HPA, the output response of the HPA consist of harmonics of the fundamental frequency f_0 like $2f_0$, $3f_0$, $4f_0$ and it continues. These harmonic products have lower amplitude than fundamental frequency. Therefore only second and the third harmonic is considerable for experimental studies.

As in illusrated in Figure 2.3, in order to examine the nonlinear behaviour of a nonlinear system, harmonic radar, one of the fundamental and robust techniques is to transmit single-tone frequency, f_0, and receive the emitted harmonics, $2f_0$ and $3f_0$, from nonlinear scatterer. When a single-tone signal is given as input to a nonlinear system, The generation of harmonic responses can be expressed as follows based on the Taylor power series expansion. Therefore, the power series of a nonlinear model can be represented by;

$$y = \sum_{n=0}^{\infty} y_n = \sum_{n=0}^{\infty} a_n x^n \tag{2.10}$$

$$x = x_0 \cos(\omega_0 t + \theta) \tag{2.11}$$

$$y = a_0 + a_1 x_0 \cos(\omega_0 t + \theta) + a_2 x_0^2 \cos^2(\omega_0 t + \theta) + a_3 x_0^3 \cos^3(\omega_0 t + \theta) \tag{2.12}$$

Therefore, the harmonic power series expressed as;

$$\begin{aligned} y =& a_0 + a_1 x_0 \cos(\omega_0 t + \theta) + a_2 x_0^2 \left(\frac{1}{2} + \frac{1}{2} \cos(2\omega_0 t + 2\theta) \right) ... \\ & ... + a_3 x_0^3 \left(\frac{3}{4} \cos(\omega_0 t + \theta) + \frac{1}{4} \cos(3\omega_0 t + 3\theta) \right) \end{aligned} \tag{2.13}$$

$$\begin{aligned} y =& a_0 + \frac{1}{2} a_2 x_0^2 + \left(a_1 x_0 + \frac{3}{4} a_3 x_0^3 \right) \cos(\omega_0 t + \theta) ... \\ & ... + \frac{1}{2} a_2 x_0^2 \cos(2\omega_0 t + 2\theta) + \frac{1}{4} a_3 x_0^3 \cos(3\omega_0 t + 3\theta) \end{aligned} \tag{2.14}$$

As depicted in (2.13) and (2.14), the power series of the second harmonic yields twice the input frequency and twice the input phase. Furthermore, for the third harmonic, the input frequency isolates three times the input frequency and the input phase.

2.2 Derivation of Nonlinear Radar Equation and Nonlinear Cross Section

The radar equation, also named the radar range equation, is a fundamental formula that describes the relation between transmitted power, reflected power, propagation loss, and received power. The radar equation, described in (2.15), calculates the received power of the radar system. It is used in the design phase of a radar system to ensure that the radar has the desired receiver sensitivity and output power.

$$P_R = \frac{\lambda^2 \sigma}{(4\pi)^3} \left(\frac{G_R}{R_R^2}\right) \left(\frac{G_T P_T}{R_T^2}\right) \tag{2.15}$$

P_T : Transmit output power (W)
P_R : Receive input power (W)
G_T : Transmit antenna gain (dBi)
G_R : Receive antenna gain (dBi)
R_T : Transmit to target distance (m)
R_R : Receive to target distance (m)
λ : wavelenght (m)
σ : radar cross-section of the target m^2

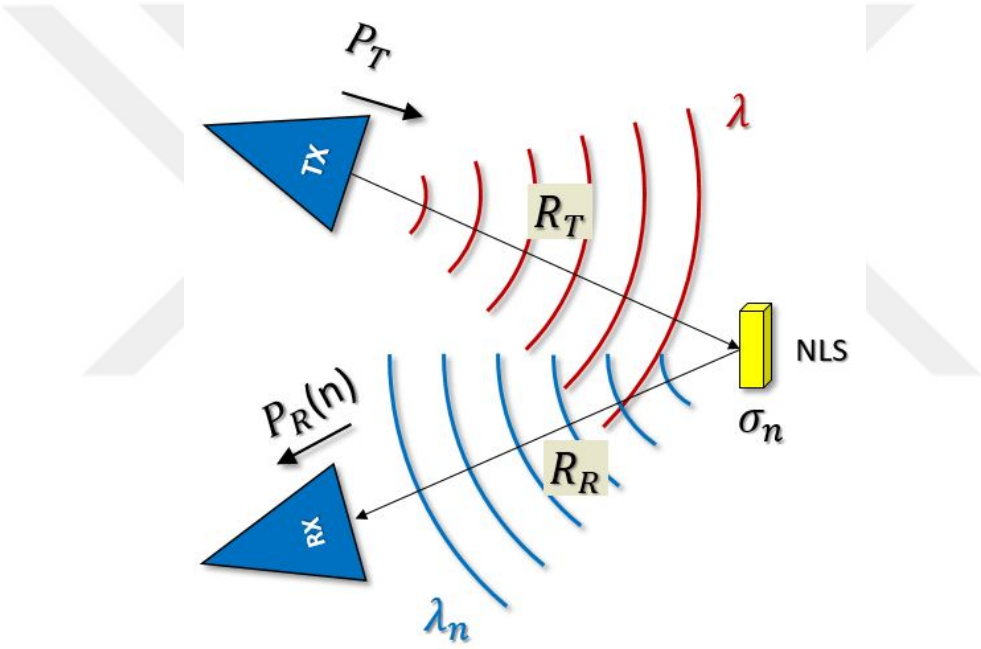


Figure 2.4 Nonlinear scatterers and harmonic radar illustration

In a nonlinear radar system, the radar equation has to be customized for this specific radar system since the harmonic multiples of the fundamental frequency are sensed. The emitted RF signal from a nonlinear target depends on the number, position, and polarisation of the p-n junctions in the target, as illustrated in Figure 2.4. A useful approach for modeling purposes is the assumption that the harmonic RF signal emitted from a nonlinear target behaves like a signal from a Hertz dipole. A Hertz dipole is a theoretical model of a radiating antenna that has a very small wavelength ($\lambda_{\text{Hertz}} \ll \lambda_{\text{Emitted}}$) compared to the wavelength of the emitted signal. This model simplifies the analysis and allows established antenna theory to predict the radiated harmonics' radiation pattern and other properties.

By making another assumption, namely that the nonlinear target has an effective field, A_{tg}, a nonlinear radar equation can be developed [23].

$$P_{in} = \frac{P_t G_t}{(4\pi)^2 R^2} \cdot A_{tg} \tag{2.16}$$

In (2.16), P_{in} Represents the incoming power density to the target, considering the effective area of the target A_{tg}.

By employing received power, P_{in}, the nonlinear interaction could be derived using the memoryless power series given in (2.16).

$$P_{\text{out}} = \sum_{n=1}^{\infty} [a_n \cdot (P_{\text{in}})^n] \tag{2.17}$$

where a_n is the scaling coefficient of the nth harmonic. The power at the nth harmonic can be derived as;

$$P_{out_n} = a_n \cdot (P_{in})^n \tag{2.18}$$

When the n^{th} harmonic frequency effective transmission gain is described as G_{tgtn}, the scattered power from the target can be derived as in (2.19).

$$P_{sc_n} = G_{tg,n} \cdot P_{out,n} \tag{2.19}$$

In (2.20), if P_{sc_n} is an RF signal that comes back to the receiver port from the distance of R, S_{r_n} could be defined as the incident power density at the receiver for a given n^{th} harmonic.

$$S_{r_n} = \frac{P_{sc_n}}{(4\pi R^2)} \tag{2.20}$$

Thus, when the terms from (2.16) to (2.20) are arranged to relate the received power density S_{r_n} with the n^{th} harmonic to the transmitted power and antenna gains, the received power density with the n^{th} harmonic could be defined as;

$$S_{r_n} = \left(P_t G_t \frac{\lambda^2}{(4\pi)^2 R^2} \right) (G_{tg,n} a_n \sigma')^n \left(\frac{(P_t G_t \lambda^2)}{(4\pi)^2 R^2} \right)^{-1} \left(\frac{1}{(4\pi)^2 R^2} \right) \tag{2.21}$$

An examination of the expression given in the second and third term of (2.21) reveals that it is directly related to the RCS, σ' and that it belongs to the nth harmonic scattered from a target which is expressed as nonlinear RCS, σ_n.

$$\sigma' = \left(\frac{(P_t G_t \lambda^2)}{(4\pi)^{1+2n-2}} \right)^{-1} \cdot \sigma_n \tag{2.22}$$

From (2.22), the nonlinear RCS of the target, σ_n, describes the measure of how the target reflects the RF signal at the n_{th} harmonic, and it could be described as in (2.23).

$$\sigma_n = a_n G_{tg,n} (A_{tg})^n \tag{2.23}$$

Although the unit of a linear RCS is m^2, the situation is different for a nonlinear radar. Here, a radar cross-section equation has to be defined, which depends on the physical properties and characteristics of the nonlinear scatterer. Therefore, the nonlinear radar cross section, σ_n, unit can be expressed as $\mathrm{m}^2/(\mathrm{W}^{n-1}/\mathrm{m}^{2n-2})$.

The total received power, $P_{r,n}$, can be expressed as a product of both the effective area of the RX antenna and S_{r_n} given in (2.24);

$$P_r = \left[\frac{P_t G_t}{4\pi R^2} \right] \cdot [\sigma'] \cdot \left[\frac{1}{4\pi R^2} \right] \cdot \left[\frac{G_r \lambda^2}{4\pi} \right] \tag{2.24}$$

Thus, P_{r_n} can be expressed by substituting (2.22) and (2.23)

$$P_{r_n} = \frac{(P_t G_t)^n G_r \lambda_n^2 \sigma_n}{(4\pi)^{n+2} R^{2n+2}}. \tag{2.25}$$

$$\sigma_2 = \frac{4\pi R^2}{P_t G_t} \cdot \sigma' \tag{2.26}$$

The equations describe how the received power P_{r_n} in a nonlinear radar system is related to various parameters like the transmitted power P_t, the gain of the transmitting $G_{tg,n}$ and receiving G_r antennas, the harmonic number n, and the nonlinear radar cross-section σ_n. They elaborate on how the power received from

a target is calculated, considering the nonlinear interaction between the transmitted signal and the target's characteristics, resulting in harmonics of the fundamental frequency. The σ' and σ_n terms represent the target's apparent and actual nonlinear RCS, respectively, contributing to the power scattered back to the radar receiver. (2.25) is referred to as the nonlinear radar equation, which is fundamental in understanding and designing nonlinear radar systems.

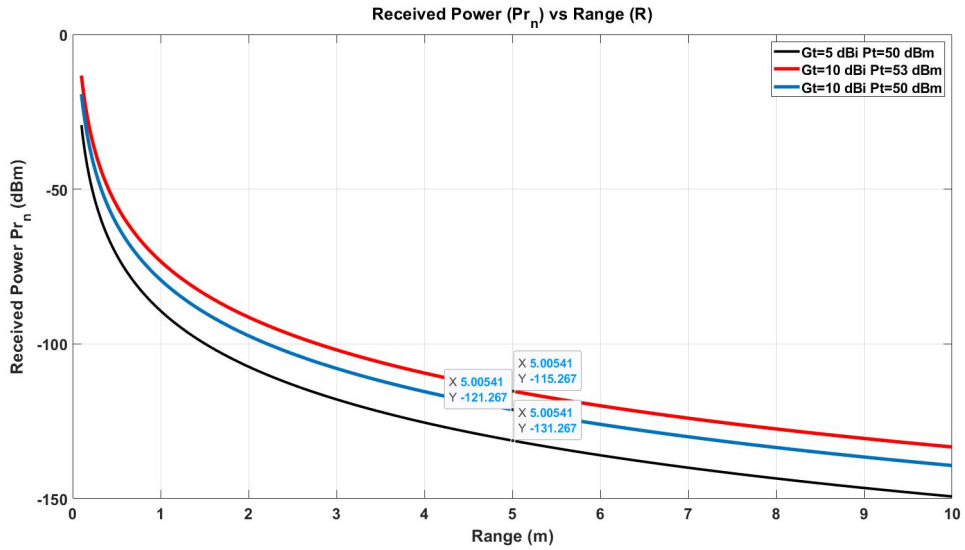


Figure 2.5 The comparison of received power P_{rn} and Range R

In order to properly understand the nonlinear radar equation given in (2.25), a theoretical plot of receive power as a function of the range is illustrated in Figure 2.5. The transmitted power increases from 50 to 53 dBm, and the analyzed harmonic order is $n = 2$. Transmitter antenna gain G_t changed from 10 to 5 dBi. The distance range, R, is determined as 0-10 meters. The scaling coefficient for the nonlinear interaction constant, a_n is 2.5, the effective area of the target at the second harmonic is $100cm^2$, and the effective transmission gain at the second harmonic, $G_{tg,n}$, is $12e^{-5}$. It is seen that the receiver power is proportional to both the transmit antenna gain and transmitted power increased/decreased by the n dB improvement/degradation in receive power [25]. Herein, when the transmitted power is increased from 50 to 53 dBm, there is a 6 dBm power improvement in received power. Furthermore, by decreasing transmitter antenna gain from 10 dBi to 5 dBi, there is a 10 dBm reduction in received power.

3
DEVELOPMENT OF HARMONIC BEAMFORMING MEASUREMENT SYSTEM

3.1 Transmitter Front-End Components and Operational Mechanism

To realize the highly sensitive harmonic radar system with a high Signal-to-Noise ratio (SNR), the transmitted fundamental signal needs to be harmonic-free and encompass exclusively the targeted fundamental frequency. First, the power amplifier and filter selection have crucial design materials for a harmonic-free system. One of the primary requirements of harmonic radars is that the signals transmitted from the transmitter are either completely devoid of or highly suppressed at the harmonic multiples of the fundamental frequency. The most fundamental way to achieve this is by selecting a power amplifier structure that generates low harmonic signal output and using a filter at the amplifier output with a high suppression ratio for signals out of the band. Another critical point to consider when choosing a filter is to minimize sensitivity increases due to nonlinear phenomena like Passive Intermodulation (PIM), which can occur due to metal-metal junctions in cavity filters. This is crucial to prevent the deterioration of the radar system's SNR and can be achieved by selecting a design with minimal contact points. Although the transmitter part of the harmonic radar system is crucial, choosing the proper receiver gain and filters are also critical initial steps in designing a harmonic radar system. Harmonic RF signals from nonlinear targets are usually relatively weak, often less than -80 dB, contingent on the target's characteristics and location, and it is essential to maximize the receiver's gain to measure these weak signals effectively. Therefore, the gain of the receiver channel should be as high as possible without RF saturation. In this study, the filter is the first component of the harmonic radar receiver channel. This filter should suppress the fundamental frequency as high as possible and pass the related harmonic frequency with minimum attenuation. Additionally, the last component of the receiver channel should be a band pass filter.

The RF harmonic signal, whose gain is increased by LNAs, must be transmitted to the next step by suppressing the harmonic components formed during the amplification process.

3.1.1 Oscilloscope Based Harmonic Radar Measurement System

In this study, two types of experimental setups have been constructed. The first HBF measurement system architecture can be seen in Figure 3.1. The first system differs from the second one, which manually adjusts the transmit and receive antennas, as well as the signal generator (Keysight N5173B) and oscilloscope (Keysight MSOV254A), as illustrated in Figure 3.2. The signal generator has been used in this setup to create a 2.4 GHz fundamental RF signal. Since the instantaneous phase of the signal generated by the PLLs is unknown, phase ambiguity will occur in the system at each cycle. Thus, major localization errors will occur in the images obtained by the microwave imaging system. To mitigate these issues and enhance the fidelity of the imaging process, a 10 dB minicircuit directional coupler has been utilized subsequent to the signal generator output port to get a reference RF signal from the signal generator. Its deployment in the measurement system is critical as it ensures consistent signal phase and amplitude sampling at the start of each measurement cycle. Thereby ensuring accurate and synchronized data acquisition is guaranteed.

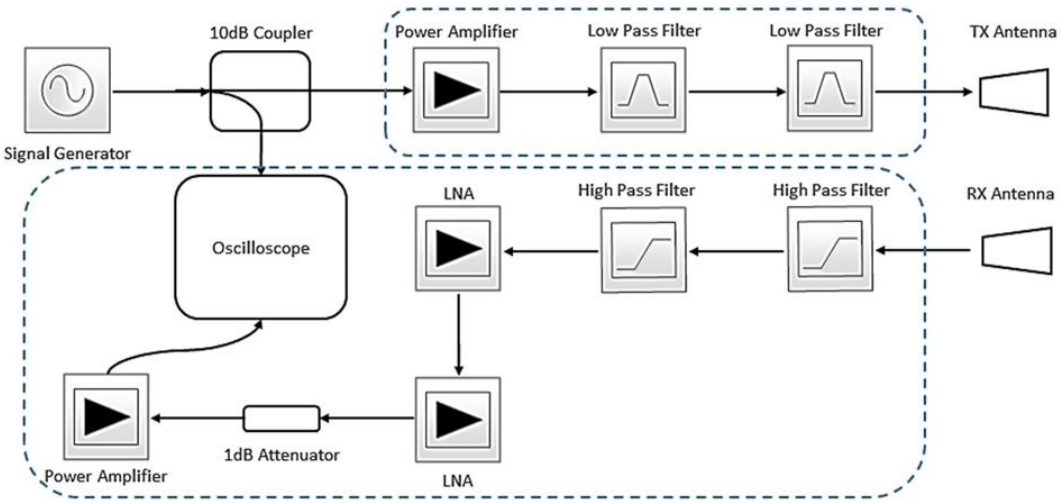


Figure 3.1 Harmonic beamforming measurement system 1 block diagram

Initiating with an input power of 15 dBm, the signal propagates through to the Mini-circuit ZHL power amplifier, which undergoes amplification by 25 dB. The total RF output signal power is measured in Figure 3.3 with a 40 dB power attenuator plugged into the input port of the spectrum analyzer.

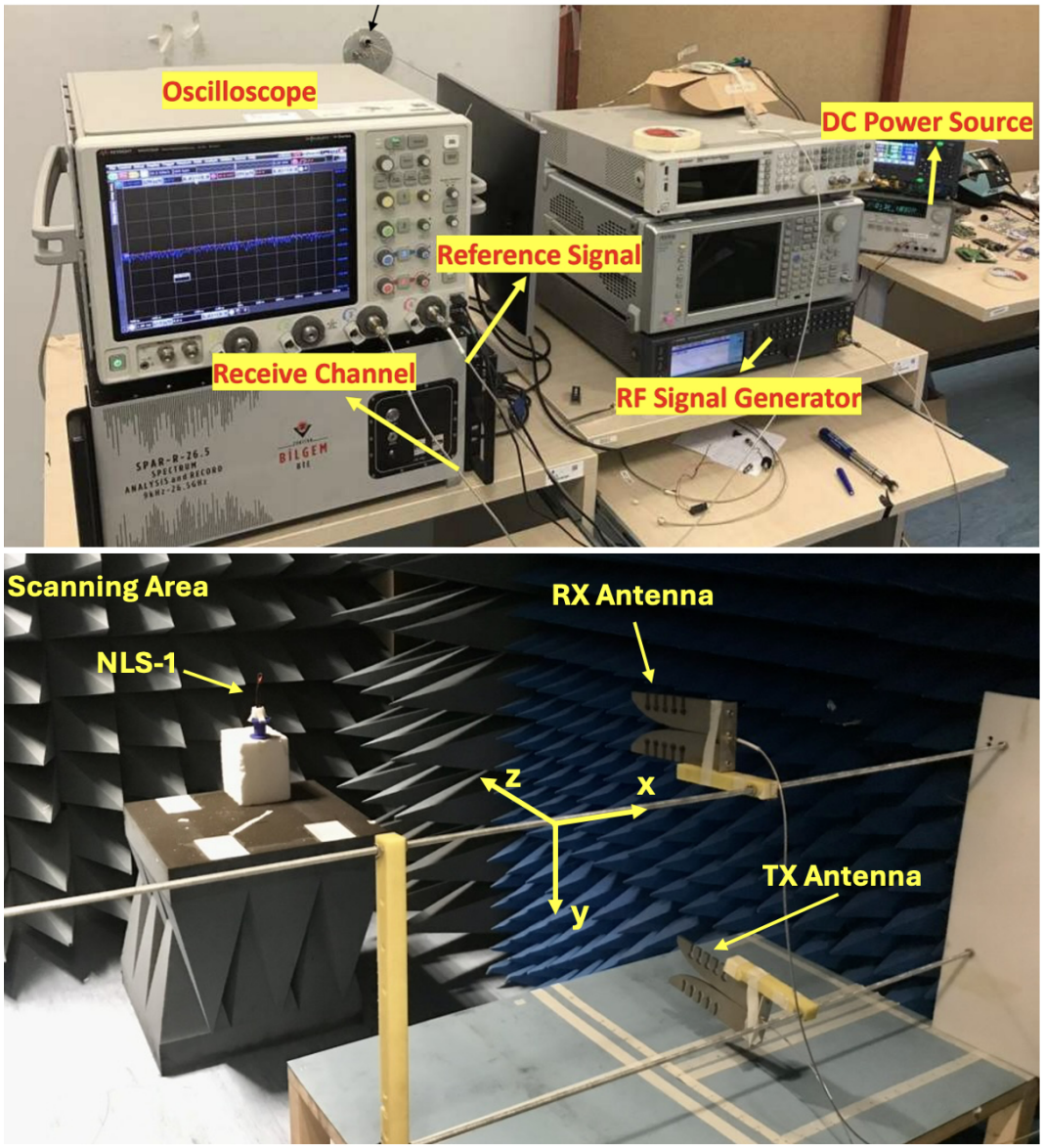


Figure 3.2 HBF measurement system 1

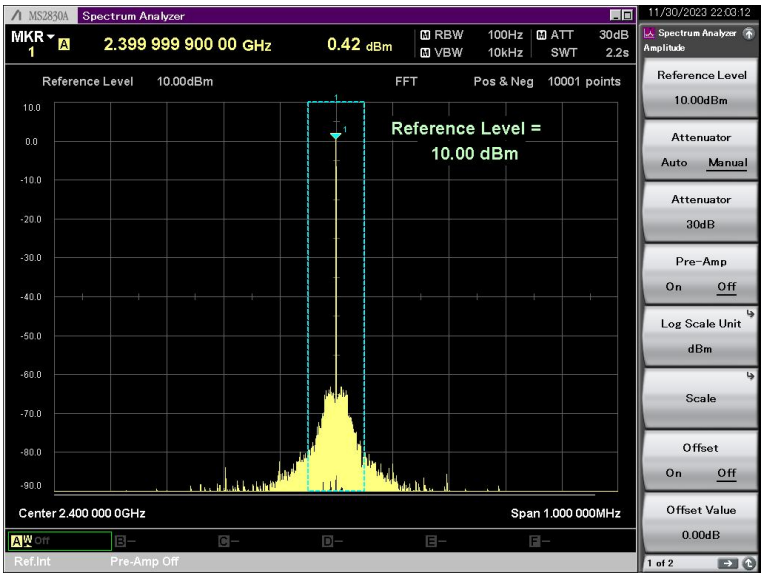


Figure 3.3 The transmitter block output power at 2.4 GHz

Once the RF signal is amplified, it goes through the two custom-designed cascaded bandpass cavity filters to suppress the generated high-amplitude harmonics that may introduce false detections and worsen the radar system sensitivity level. In this radar system, it is worth noting that the spectrum analyzer noise floor is -120 dBm. The cavity filters are a robust solution for suppressing the unwanted harmonics, as shown in Figure 3.4. The two cascaded cavity filters insertion loss at 2.4 GHz nearly 1.2 dB and have a suppression capability exceeding 120 dB for the second harmonic at 4.8 GHz.

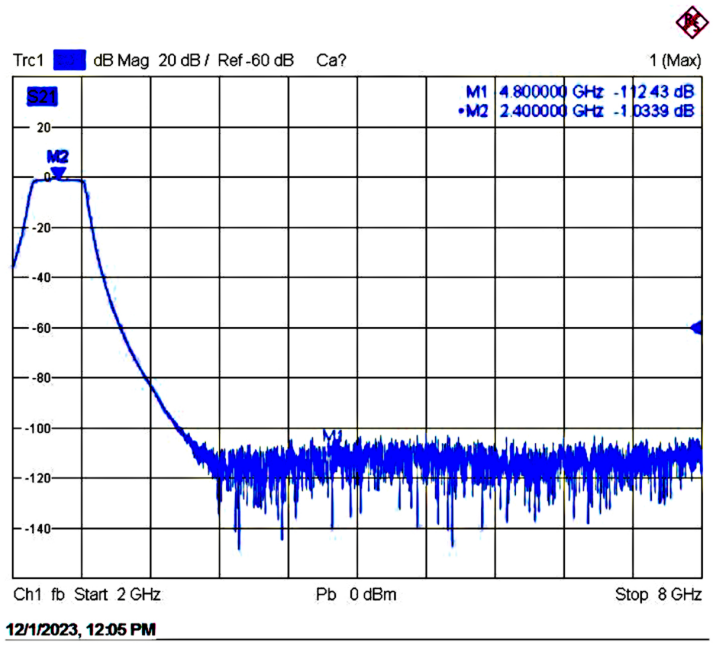


Figure 3.4 The measurement of the S21 result of cavity filter

Subsequent to the completion of the fundamental RF signal filtration phase, the fundamental signal is propagated through the transmit antenna, which has a gain of approximately 8 dBi at 2.4 GHz [26]. The transmitting and receiving antennas share an identical design architecture. The antenna structure is explained in detail in section 3.3.

3.1.2 Sofware-Defined Radio (SDR) Based Harmonic Radar Measurement System

When the secondary harmonic beamforming measurement system is examined, remarkable improvements can be seen in Figure 3.5. The transceiver and scanning antenna system have been changed compared to the first one in terms of hardware components. In this section, the transmitter, receiver, and power amplifier block have been replaced with different components and investigated here. Therefore, the mechanical hardware improvements of the scanning system are discussed in detail in section 3.5.

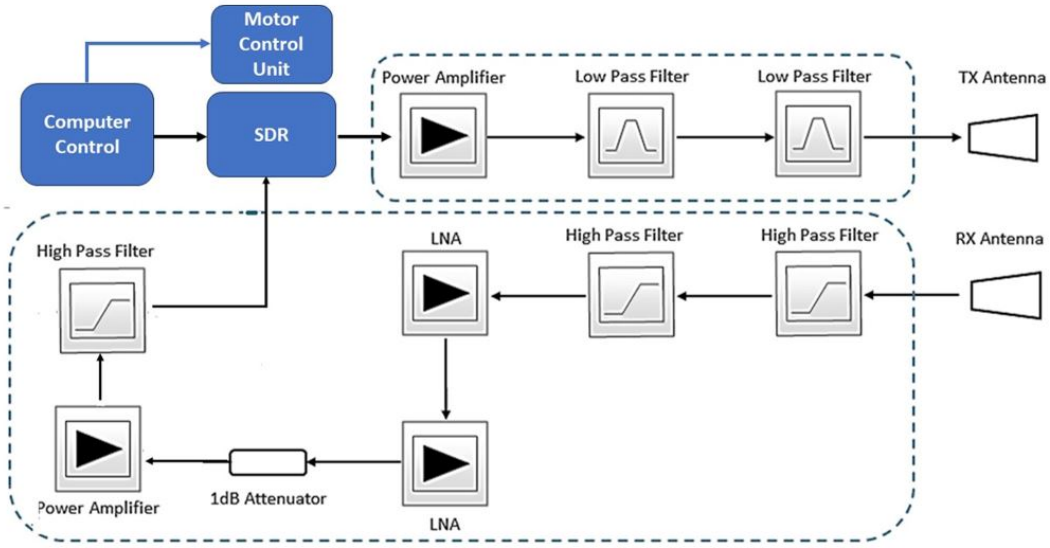


Figure 3.5 Harmonic beamforming measurement system 2 block diagram

As mentioned before, the oscilloscope used in HBF-1 in this study has a broadband structure and can simultaneously measure three different signals, f_0 f_2 and f_3. On the other hand, the non-portability and expense of the oscilloscope led the study to design a more effective system.

Upon the analysis of Figure 3.8, it is observed that the signal generator has been removed and SDR-based transceiver hardware has been utilized in order to enhance the scanning speed and portability of the HBF-1 system. This hardware upgrade significantly increased measurement speed over the previous system and eliminated

measurement errors caused by manual adjustments. Furthermore, the system's cost has been dramatically reduced by utilizing the SDR as a transceiver.

It is possible to measure different frequencies simultaneously by employing Network Analyzers. However, it needs to be an external hardware setup. Still, it remains less portable and significantly more expensive. Therefore, the SDR platform was chosen to measure a received signal simultaneously at harmonic multiples of the transmitted signal.

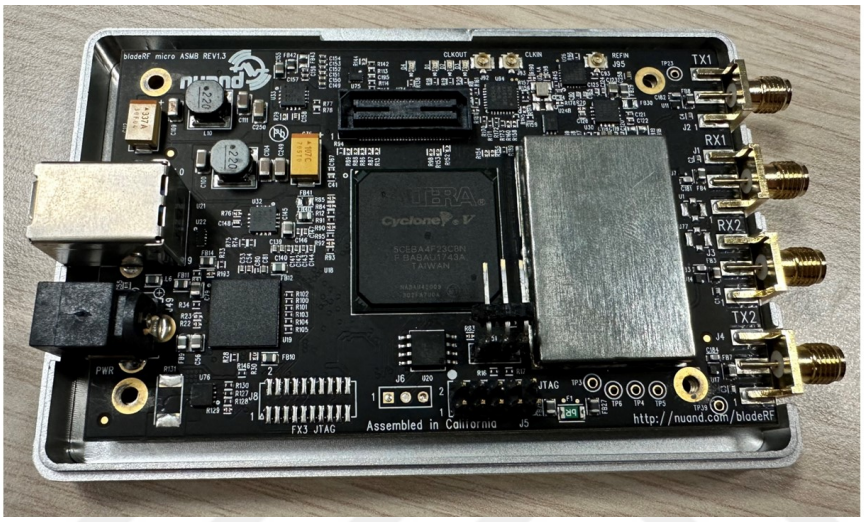


Figure 3.6 Blade RF xA4

During the experiments, the Nuand BladeRF 2.0 xA4 software-defined radio (SDR) has been utilized in order to construct a low-cost, portable, and robust solution for harmonic beamforming systems' transceiver architecture, as shown in Figure 3.6. The BladeRF 2.0 xA4 has been selected for its comparable price and is suitable for multi-functional and multi-frequency radar applications [27]. Additionally, it does not require any external power source, it operates from the USB 3.0 port of the notebook during the experimental studies.

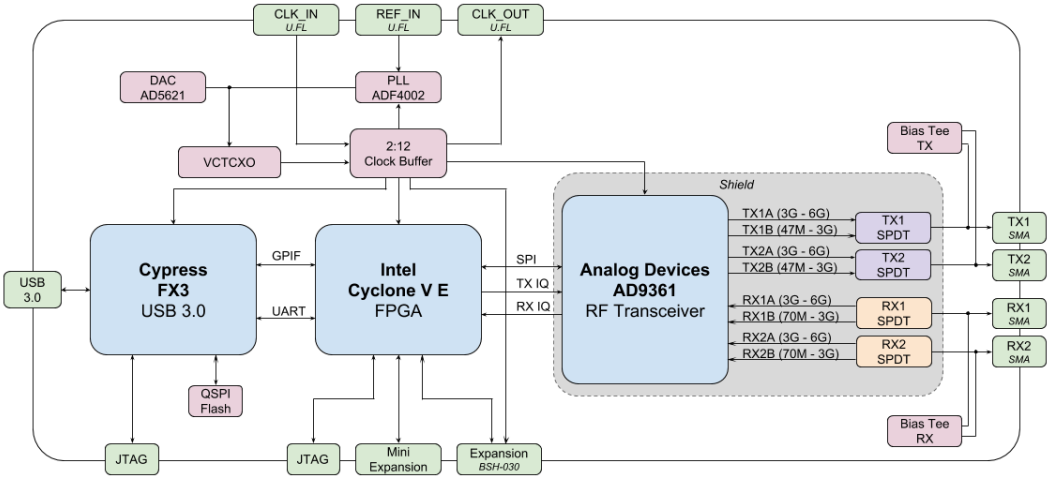


Figure 3.7 Blade RF xA4 block diagram [28]

According to Figure 3.7, the BladeRF 2.0 xA4 block diagram has defined the main components of SDR that include Intel Cyclone V E FPGA for customizable digital signal processing, Cypress FX3 USB 3.0 interface, Analog Devices AD9361 RF transceiver front-end structure which is capable of both transmit and receive a wide range of frequencies, clock generating components named DAC (AD5621) and PLL (ADF4002) and a fine-tune VCTCXO which are essential for maintaining the timing of a signal process, Data interfaces (SPI, UART, QSPI and GP/IF), and RF TX/RX channels.

In the BladeRF system, timestamping synchronizes transmit (TX) and receive (RX) operations. The counters provide timestamps, crucial for applications requiring precise timing, such as telecommunications or radar systems. The BladeRF minimizes any deviation between the TX and RX sample rate clocks. This means that the time difference between the two remains consistent. This is necessary to maintain synchronization in applications that require tightly coupled send and receive operations.

Once the RF performance of the SDR platform is examined, a driver amplifier structure needs to be integrated between the SDR and power amplifier to amplify the weak SDR's RF output signal from -20 dBm to 15 dBm. The minicircuit VLF-3000+ then filters the amplified RF signal before the input port of the power amplifier. Subsequent to the filtering process, the RF signal is amplified by the power amplifier to have a final output power of approximately 40 dBm, then passed through the cavity filter and sent to the antenna.

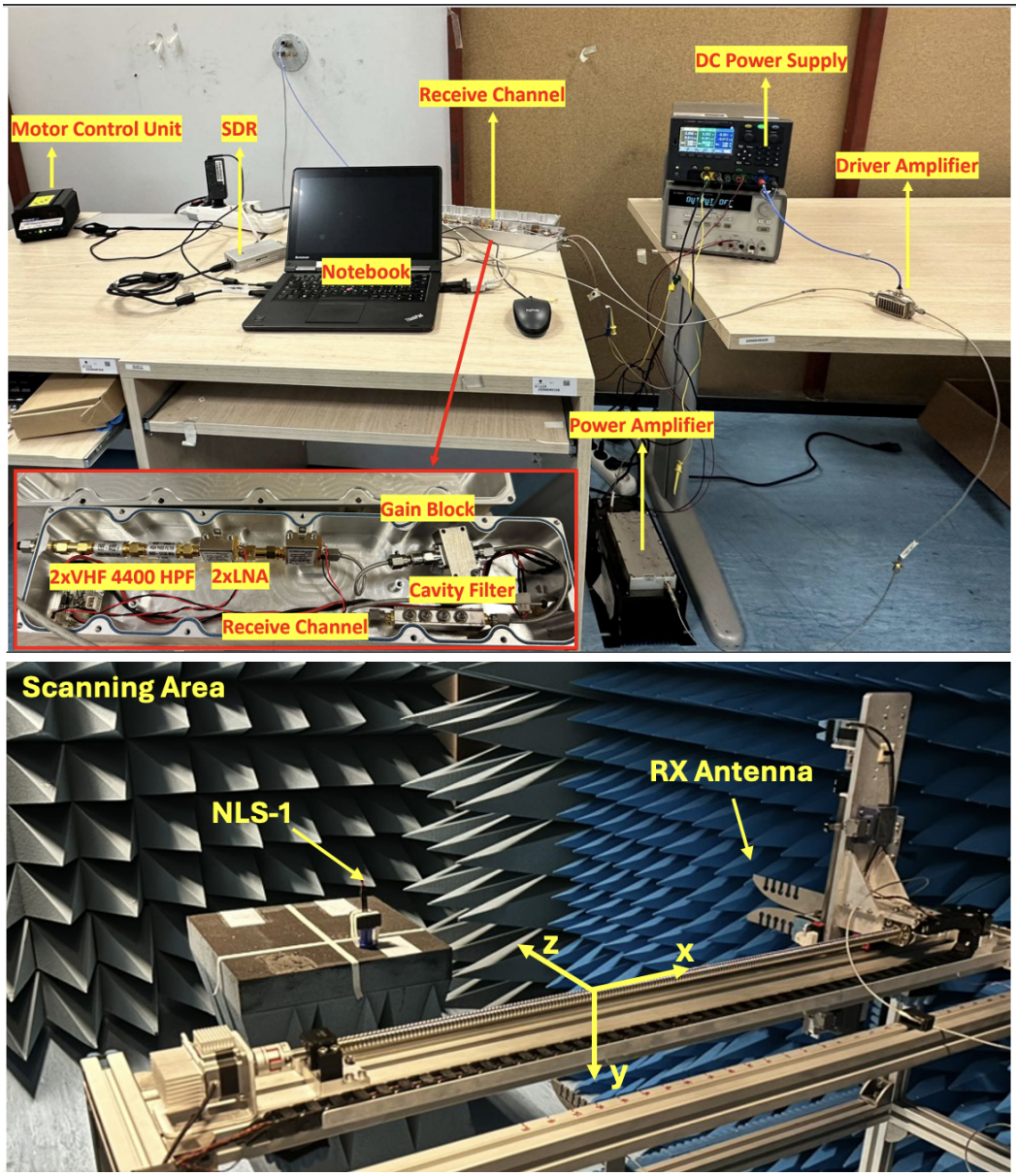


Figure 3.8 Harmonic beamforming measurement system 2 and motor-controlled scanning system

3.2 Receiver Front-End Components and Operational Mechanism

While the receiving antenna structure in the first system is manually controlled and fine-tuned, in the second system, this structure was developed to be motor-controlled. The receiving antenna is adjusted in both systems with a spacing of $\Delta_x = 3\,\text{cm}$ each. Thus, this scanning scheme results in 31 distinct antenna positions for comprehensive signal collection.

In order to suppress fundamental signals caused by reflections from clutter or

antenna coupling, two minicircuit VHF-4400+ high-pass filters have been employed in front of the LNAs. If the fundamental frequency signal arriving at the receiver channel is passed to the amplifiers without being filtered, it will be amplified here and will cause deterioration in the sensitivity level of the system. According to Figure 3.9, one VHF-4400+ filter has 60 dB fundamental frequency suppression, and insertion loss equals 1.3 dB. Furthermore, two cascaded VHF-4400+ have the ability to suppress 103 dB of fundamental frequency and 2.5dB of insertion loss.

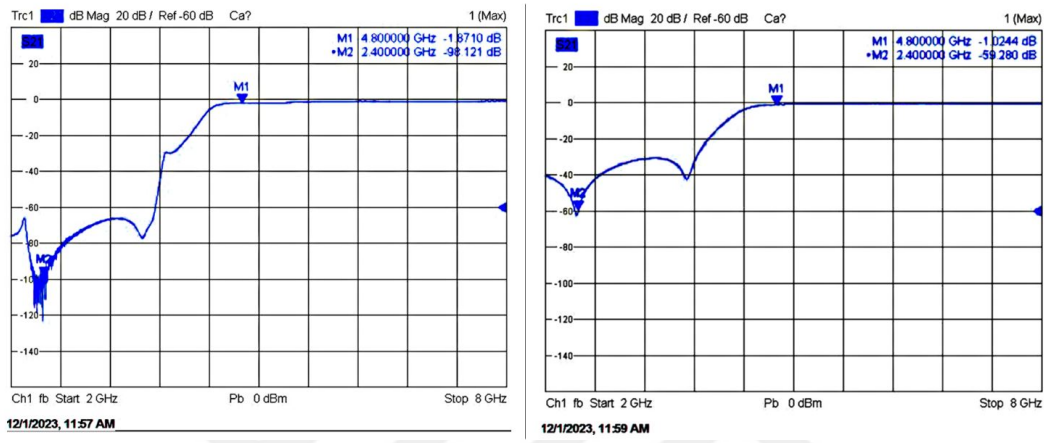


Figure 3.9 One VHF 4400 (left) and two VHF 4400 (right) S21 measurement results

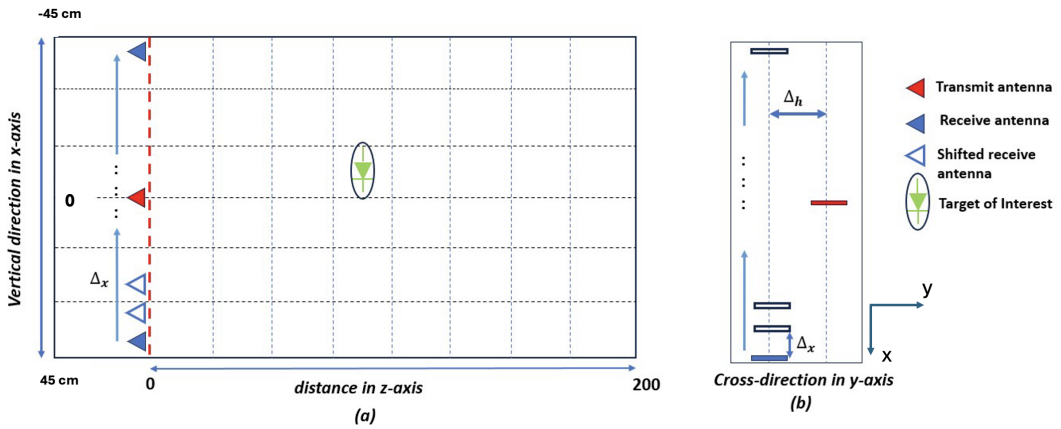


Figure 3.10 Measurement system schematic

Once the filtering process of the incoming RF signal in the receive channel is completed, two ZX60-63GLN+ minicircuits LNA take over the amplification process, which has a total gain of 50 dB. The amplified RF signal then passes through the mini-circuit gain block, which has a gain of 25 dB. To optimize the impedance matching and ensure uninterrupted signal transfer between the LNAs and the gain block, a 1 dB attenuator is placed between them. In order to evaluate the total gain of the receiver block, a -80 dBm RF signal at 4.8 GHz is connected

to the receiver's input. Then, the outcome has been monitored with a spectrum analyzer, as shown in Figure 3.11 (Top). The total gain of the receiver channel measured 75 dB (including 5 dB RF cable loss). Nonetheless, due to the presence of residual low-level amplified RF signals, these RF signal harmonics need to be filtered out prior to data acquisition. The cavity filter, BP-6000 series, has been employed for this process, providing 80 dB rejection at 2.4 GHz and 1.1dB insertion loss, as shown in Figure 3.12. Once the 0 dBm 2.4 GHz RF signal is applied to the input port of the RX channel, substantial suppression of over 100 dB has been applied to the fundamental RF signal, as shown in Figure 3.11.

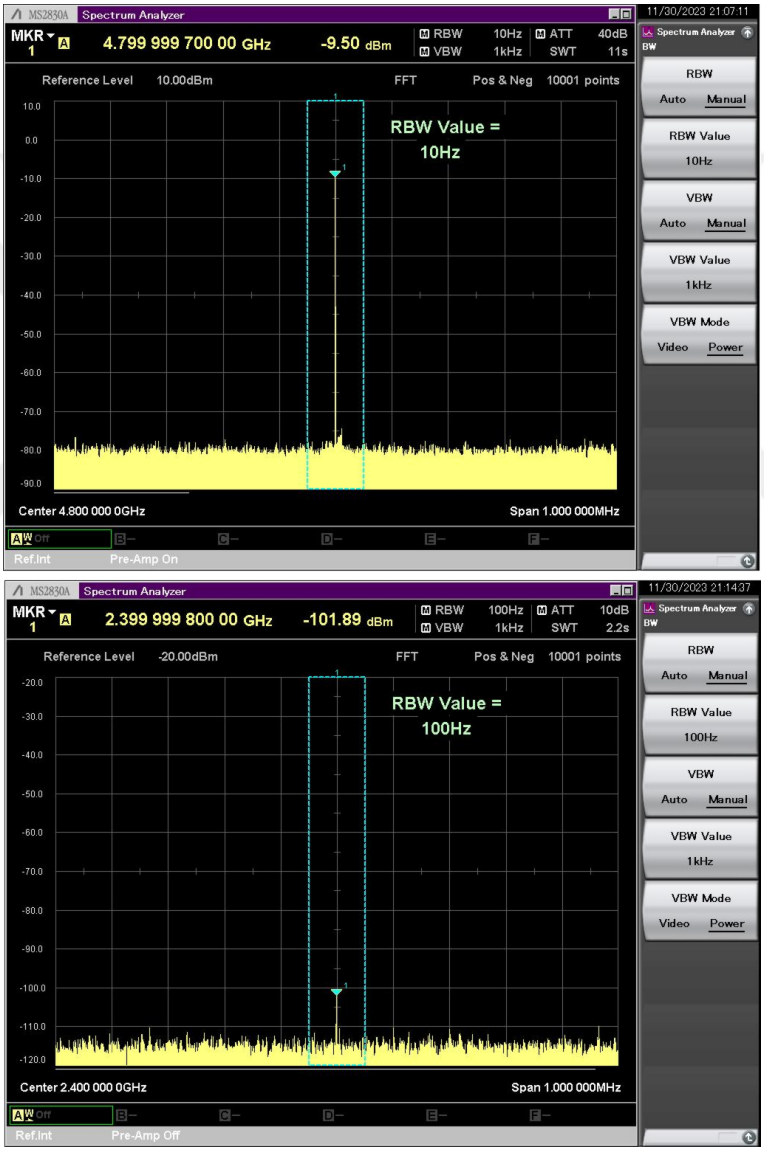


Figure 3.11 Receiver channel measured gain (top), the measured result of the 2.4 GHz at output port of the receive channel when the input power of 0 dB at 2.4 GHz (below)

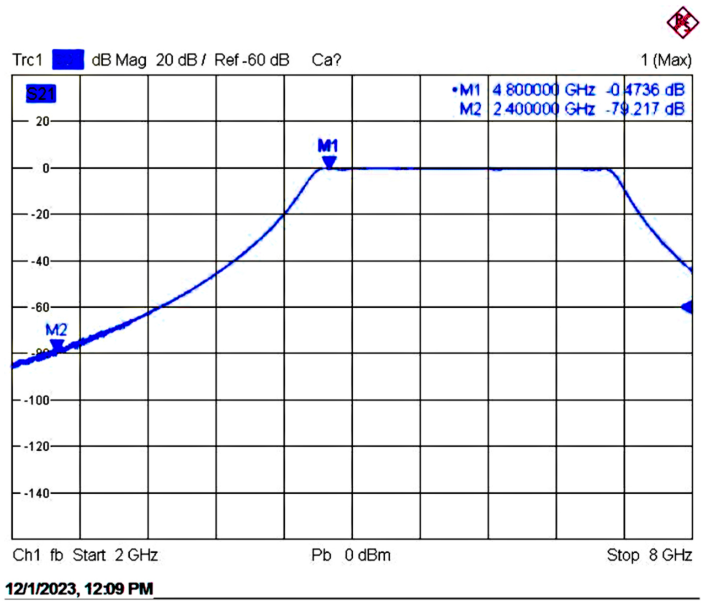


Figure 3.12 S21 measured result of the cavity filter placed on receiver block

In the data acquisition phase of the first system, the Keysight Infinium series 80 GS/s oscilloscope has been utilized. The oscilloscope measurement parameters are 200.000 data points, 40GS/s sampling rate, and 4096 averaging. Conversely, the HBF-2 system has SDR to get I/Q data from the receiver block. In HBF-1, the time data collection begins by gathering a 200,000-time series of data points for each receiver antenna position. An extensive collection, a matrix with dimensions of 31x200,000, has been obtained for each antenna position. The subsequent analytical step involves the implementation of a Fast Fourier Transform (FFT) with a size of 4096. This effective compression reduces the measurement matrix to a size of 31x48 and makes this matrix more manageable. The matrix encapsulates the amplitude and phase characteristics of the target(s). This refined measurement matrix is a fundamental data set for the advanced imaging process.

3.3 Innovative Antenna Design for Enhanced Harmonic Beamforming Performance

In this study, a broadband all-metal Vivaldi antenna has been designed and implemented on both measurement systems. Due to low metal-to-metal contact requirements, the proposed antenna structure is fabricated of solid aluminum. In Figure 3.13, all three types of the designed antenna models are illustrated. The reference antenna without a slot is designed to compare the effects of the slots on antenna performance parameters. A CST transient solver was employed to analyze the proposed antenna design. The simulations have consumed over 75 million mesh

cells. The aluminum 5083 material is chosen as the antenna's main. The reference model and the modified version of the antenna have similar dimensions, except for the slot shapes. The total weight of the proposed antenna with *Rexolite* is 250 grams, and without Rexolite, it is 230 grams.

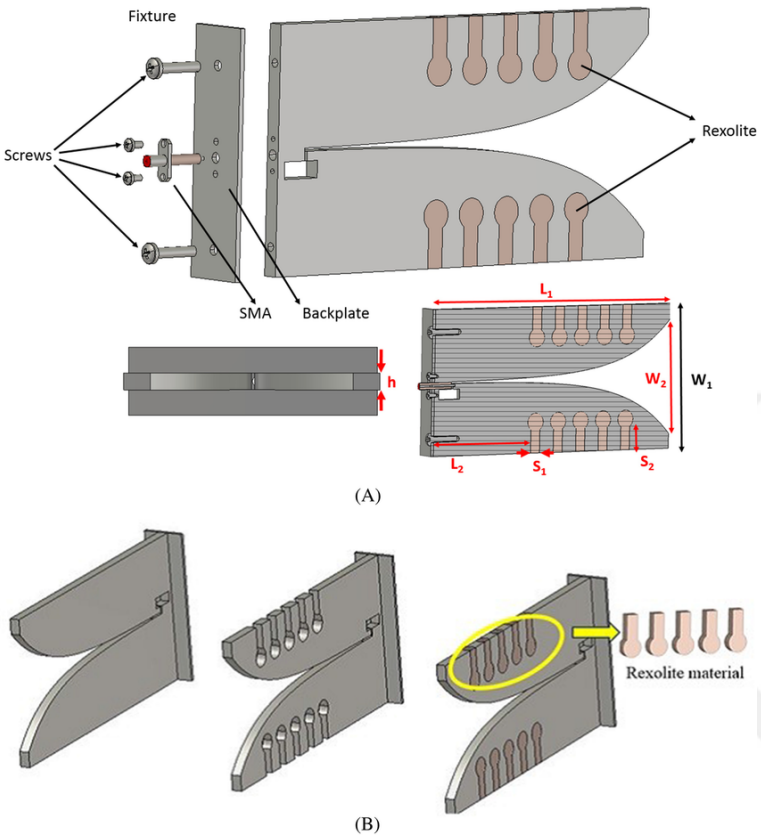


Figure 3.13 (a) Simulation model of the SEMVA (b) Evolution model of the all-metal Vivaldi antenna; reference model, slotted edge model, and *Rexolite* inserted slotted edge model, respectively.

Table 3.1 Antenna design parameters

Parameter	Dimension (mm)
L1	182
W1	96
W2	76
S1	14.56
S2	7
L2	72.6
h	6.1

The tapering slot's exponential curve determines the Vivaldi antennas' radiation characteristics and impedance bandwidth. An antenna's tapering slit facilitates

a smooth impedance change from the feed impedance to the wave impedance. Furthermore, the antenna's beamwidth, bandwidth, and impedance matching are all determined by the transition's opening rate, or R, in this case. The following equations are used to create the proposed antenna's exponential curve. The start and end positions of the exponential tapering slot are $P1(x1, y1)$ and $P2(x2, y2)$, respectively, while the tapering slot's opening rate is denoted by the coefficient R [16].

$$y = C_1 e^{R_x} + C_2 \tag{3.1}$$

$$C_1 = \frac{y_2 - y_1}{e^{R_{x2}} - e^{R_{x1}}} \tag{3.2}$$

$$C_2 = \frac{y_1 e^{R_{x2}} - y_2 e^{R_{x1}}}{e^{R_{x2}} - e^{R_{x1}}} \tag{3.3}$$

Figure 3.13b shows the modified version of the antenna. The slot shape and dimensions are optimized to achieve a broader bandwidth and the desired radiation pattern at lower operating frequency bands. Once several different shapes have been tried and implemented on a modified version of the antenna, it has been found that the best antenna performance pattern has been obtained with circularly shaped slots. According to the results, the circular slot shape with a 12 mm radius provides the best results.

The current distribution of the proposed antenna is given in Fig 3.14 in order to show how slots effect the antenna's electrical performance. As studied in [29] cutting slots at the end of the flares improves the radiation behavior and changes the current distribution of the antenna below the cut-off frequency, as expected. The antenna cut-off wavelength is calculated as follows;

$$\lambda_c = 2W_2 \tag{3.4}$$

As a result of (3.4), the aperture width W_2 of the reference all-metal Vivaldi antenna must be increased by 1.5 to achieve the lower cut-off frequency of 1.3 GHz. Thus, the electrical dimension of the proposed antenna is improved by adding slots. Comparing the current distribution of two antennas at 1.5 GHz, the surface current distribution at the tapered slots of the SEMVA is dominant along the B region.

The surface currents of the modified antenna are more concentrated at the end of the antenna taper than those without slots. As a result, the modified antenna has a higher directivity than the one without slots. However, the slotted edges do not significantly affect the current distribution of the antenna above 8 GHz and do not degrade or improve the antenna's radiation pattern.

Due to the addition of slots at the end of SEMVA, additional resonances are triggered and thus, the return loss parameter is significantly reduced at the beginning of the operational frequency band. The input impedance of the modified and reference antennas are compared in Figure 3.14 b. Below 2 GHz, the results show that the real part of the input impedance of the modified antenna is closer to 50 Ω , and the imaginary part is closer to 0 Ω compared to the antenna without slots.

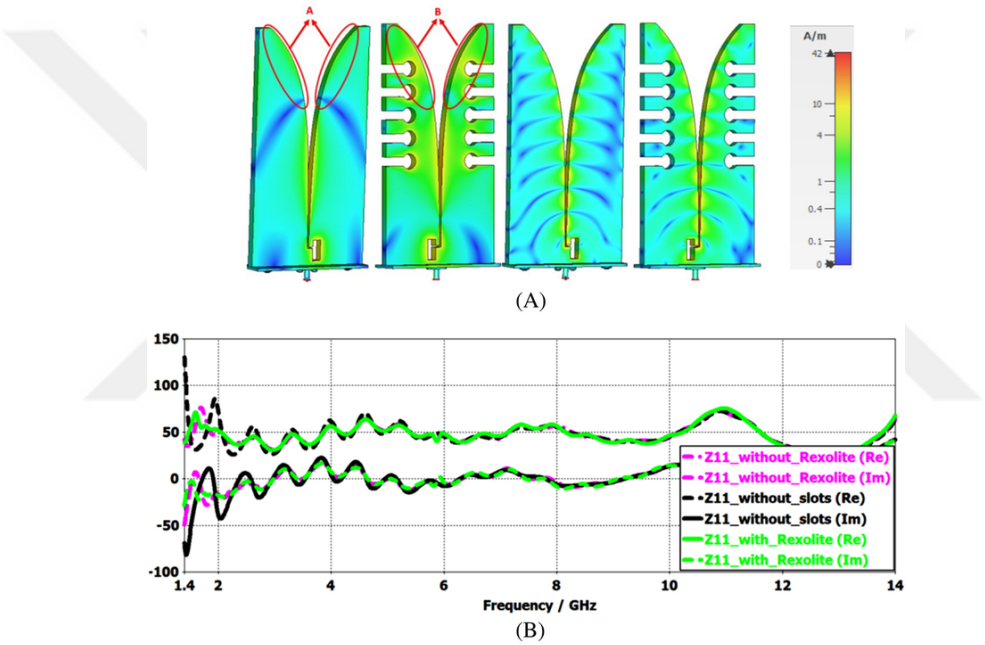


Figure 3.14 a) The current distribution of proposed antenna b) real and imaginary part of the proposed antennas

In the final design stage of the antenna, it is found that implementing a lossless and extended broadband impedance matching is not possible[34]. Therefore, almost pure resistive *Rexolite* material ($\epsilon_r = 2.53 \quad \mu_r = 0.00066@10GHz$) is inserted into the empty slots, as shown in Figure 3.13b. The *Rexolite* material is used to avoid frequency-dependent behavior since *Rexolite* has a very stable complex dielectric permittivity between 1 MHz to 500 GHz. In addition to the electrical properties of the *Rexolite*, it has a low material density (1.05g/cm^3) and very good suitability for high precision CNC machining/drilling, which allows us to create different shapes and lenses. Besides, it is easy to get high-quality surface roughness. After inserting *Rexolite* into the slot, the real and imaginary parts of the input impedance better

converge to 50 Ω and 0 Ω, respectively, at the lower end of the operating band, as shown in Figure 3.14b. Therefore, the optimum impedance matching for the whole band while preserving a smooth radiation pattern is achieved by manipulating the slots using dielectric loadings at the cost of a lossy matching network and slightly reduced total gain.

The feeding mechanism of the SEMVA is based on the Kindt Vivaldi antenna array structure [30]. Printed circuit technology (PCB)-based Vivaldi antenna designs typically have a feed design based on a microstrip-to-slot-line transition using quarter-wave stubs, which requires two-step transitions from coax to microstrip to radiating slot or balun structures. These feeding structures mentioned above cause frequency dependency, lower power capability, physical damage, and increased complexity and size [31]. The proposed antenna does not require an additional internal or external matching circuit and transfers energy directly to the radiator. The impedance matching is achieved directly in the aperture. The antenna's cavity dimensions and feed pin position are obtained after comprehensive studies with CST .

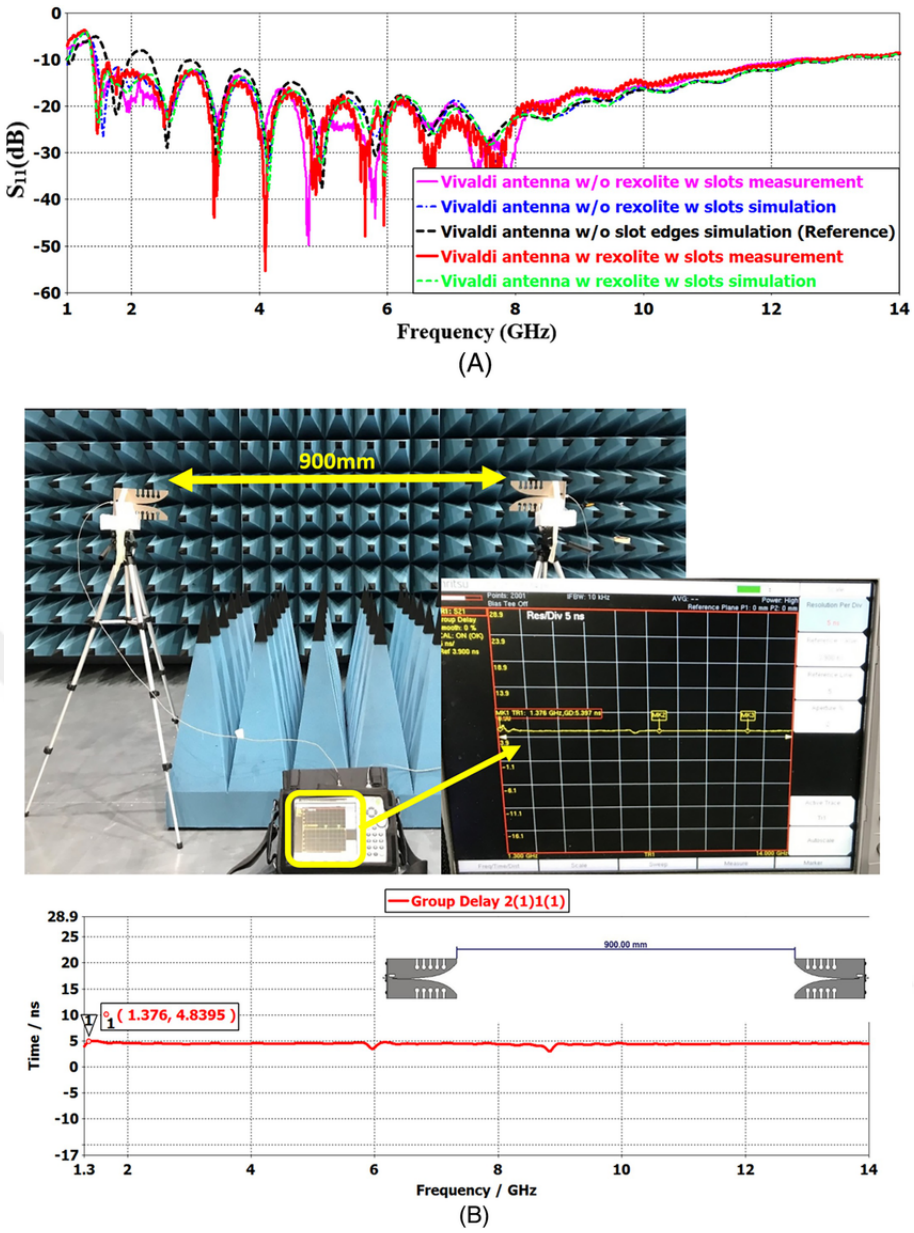


Figure 3.15 Measured and simulated reflection coefficient results (b) Group delay measurement setup and results of the proposed antenna

The Vivaldi antennas' simulated and measured scattering parameters are compared, as shown in Figure 3.15a. To obtain precise results from the simulation, the mesh settings of the CST are well-adjusted near the antenna geometry. From Figure 3.15, it is observed that the lower operating frequency of the reference antenna is 2.3 GHz. When circularly shaped slots are cut and Rexolite is inserted, a new lower resonance frequency appears, and the lowest operating frequency becomes 1.3GHz. As a result, the antenna impedance bandwidth increases. A prototype is fabricated to validate the proposed design, and the image of the proposed antenna is shown in Figure 3.15b. The scattering parameters of the fabricated antennas are obtained using a Rohde-Schwarz ZVA40 network analyzer. The experimental measurements

are in very good agreement with the simulations. Time-domain characterization is an important parameter for broadband antennas. The group delay describes the distortion level of the pulse shape from one antenna to another antenna. In this study, two SEMVA's are set face to face and separated 900 mm from each other, as illustrated in Figure 3.15b. The proposed antenna group delay is measured at approximately 4.5 ns, and the maximum variation is less than +/-1 ns for the whole operating bandwidth. According to the simulation, the proposed antenna has a very stable group delay of approximately 4.5 ns, and the maximum variation is less than +/-1 ns throughout the operation. The results show that the measured group delay is in very good agreement with the simulated group delay. A relatively flat group delay response and good time-domain characteristics are achieved.

Additionally, the power handling capacity of the metal Vivaldi antenna has been calculated for the first time in literature. Vivaldi antenna designs and productions are generally based on PCB, a simple and cost-effective procedure. However, when exposed to impact, the dielectric substrates are damaged easily because of their lower physical strength. Furthermore, the thermal capability of the dielectric material used in a substrate and adhesive material to bond the copper surface to the dielectric substrate is unsuitable for high-power applications. The 4350B substrate is investigated in this study to understand the thermal breakdown of PCB antennas better. The Rogers Corp. MWI-2019 tool [32] calculates the substrate's power-handling capacity and thermal analysis, as shown in Figure 3.16a. According to the manufacturer's datasheet, the glass transition temperature (Tg) of the 4350B substrate at the beginning of the substrate's softened state is 280 °C. In addition, the decomposition temperature (Td) at the beginning of the substrate's irreversible damage state is 390 °C. According to the MWI tool, the Tg of a 50 Ω microstrip line is 369 W and 514 W for Td. In addition, the thermal expansion coefficient (CTE, ppm) is another important thermal characteristic of substrates. Due to the different thermal expansion coefficients of adhesive, dielectric, and copper, the mechanical delamination state and interconnection issues arise at the beginning of Tg.

To compare the power-handling capacity of PCB and the metal antenna structure, the proposed antenna power-handling capacity is calculated in this study. Because of the SMA connector's low power-handling capacity, it must be replaced with a coaxial waveguide. The coaxial waveguide power-handling capacity can be obtained by [33];

$$P = \frac{1}{120}\alpha^2 E_a^2 \ln\frac{b}{a} \tag{3.5}$$

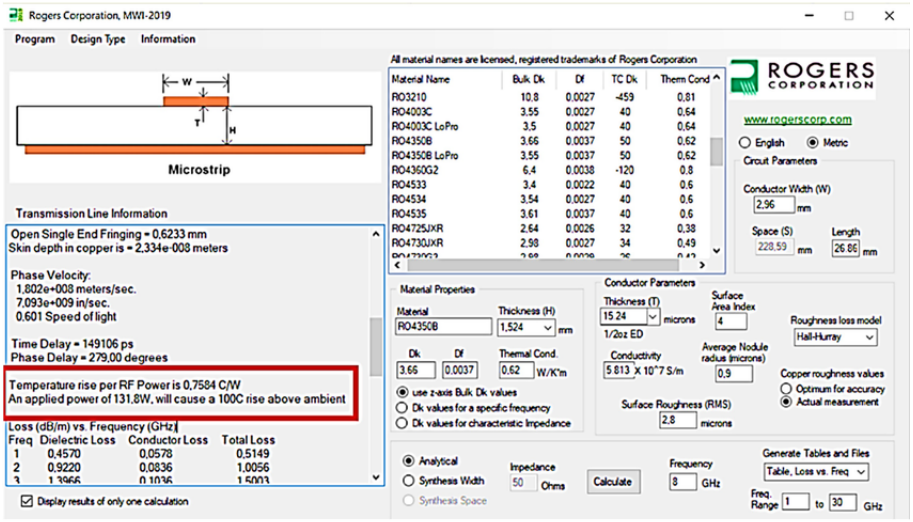


Figure 3.16 (a) Rogers MWI-2019 calculation parameters (b) E-field distribution of the proposed antenna at 8GHz

The coaxial waveguide is designed to match the proposed antenna of 50 Ω , with an inner radius (a) of 1.77 mm and outer radius (b) of 4.1 mm without any dielectric material. Taking the breakdown voltage (Ea) of 3 MV/m for the air, the waveguide power-handling capacity is calculated as 173 kW.

According to Paschen law, if the breakdown voltage level needs to be increased, the antenna could be placed inside the radome with a high-pressurized gas environment [34]. This study considers air and vacuum conditions for calculating the proposed antenna's breakdown voltage.

According to the simulation results in Figure 3.16b, the maximum electric field is approximately 10673 V/m at 8 GHz. As expected, the maximum E-field distribution occurs at the beginning of the tapered slots. To calculate the maximum breakdown voltage of the SEMVA in air, 3 MV/m, must be considered.

Therefore, the power-handling capacity of SEMVA is calculated by the following calculations;

$$(3 \times 10^6/10673)^2 = 79kW$$

Taking the breakdown voltage of the vacuum condition, 50 MV/m, the power-handling capacity of the SEMVA is calculated by:

$$(50 \times 10^6/10673)^2 = 22MW$$

According to the calculations, the PCB Vivaldi antenna's microstrip feed line can only handle up to 514 W without any irreversible damage, whereas SEMVA with a coaxial waveguide can handle up to 79 kW without any breakdown voltage. As a result, printed Vivaldi antennas have a much lower power-handling capacity than metal Vivaldi antennas.

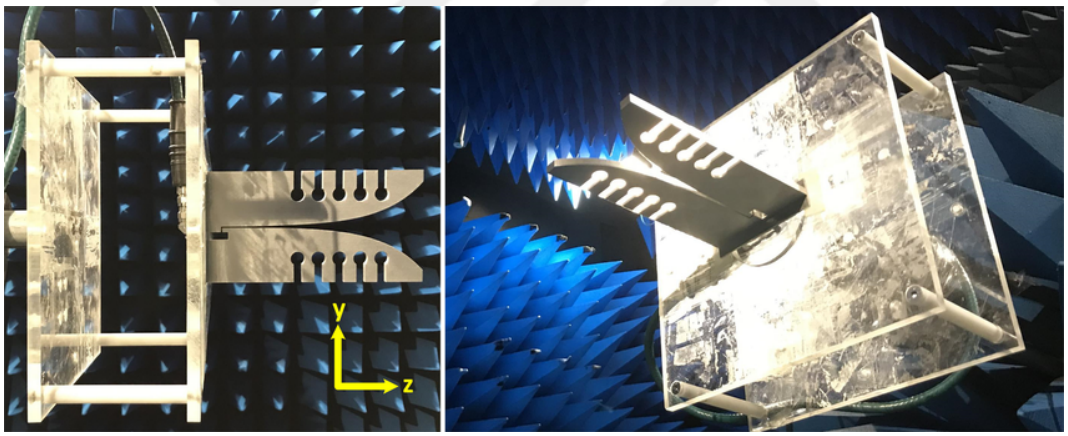


Figure 3.17 Radiation pattern measurement setup of the SEMVA inside the spherical near field chamber.

The SEMVA fabrication and assembly processes are also investigated in this section. The proposed antenna structure is constructed entirely of Aluminum 5083 material to meet the weight, power, and conductivity requirements. One of the advantages of the metal Vivaldi antenna is its suitability for high-power applications. The proposed antenna parts were fabricated using a three-axis cut from a block of aluminum, wire cutting, and high-precision drill equipment. As shown in Figure 3.13, the SMA connector passes directly through the backplate and is placed near the antenna impedance transformer cavity. To obtain the best SMA feed pin contact and electrical performance, a 1.5 mm deep and 1.3 mm

diameter hole is drilled on the opposite side of the antenna feed gap, significantly increasing the antenna feed structure robustness. This solution overcomes using the fuzz-button [35] and the soldering process used in Tianang's study [36]. The final assembly process of the proposed antenna combines the backplate, radiator, and SMA connector. These parts are screwed together with M4x20 and M2.5x6 screws, as shown in Figure 3.13a. To measure the assembled antenna pattern in a spherical near-field chamber (SNF), a fiberglass antenna holder is fabricated and placed on the rotary, as shown in Figure 3.17.

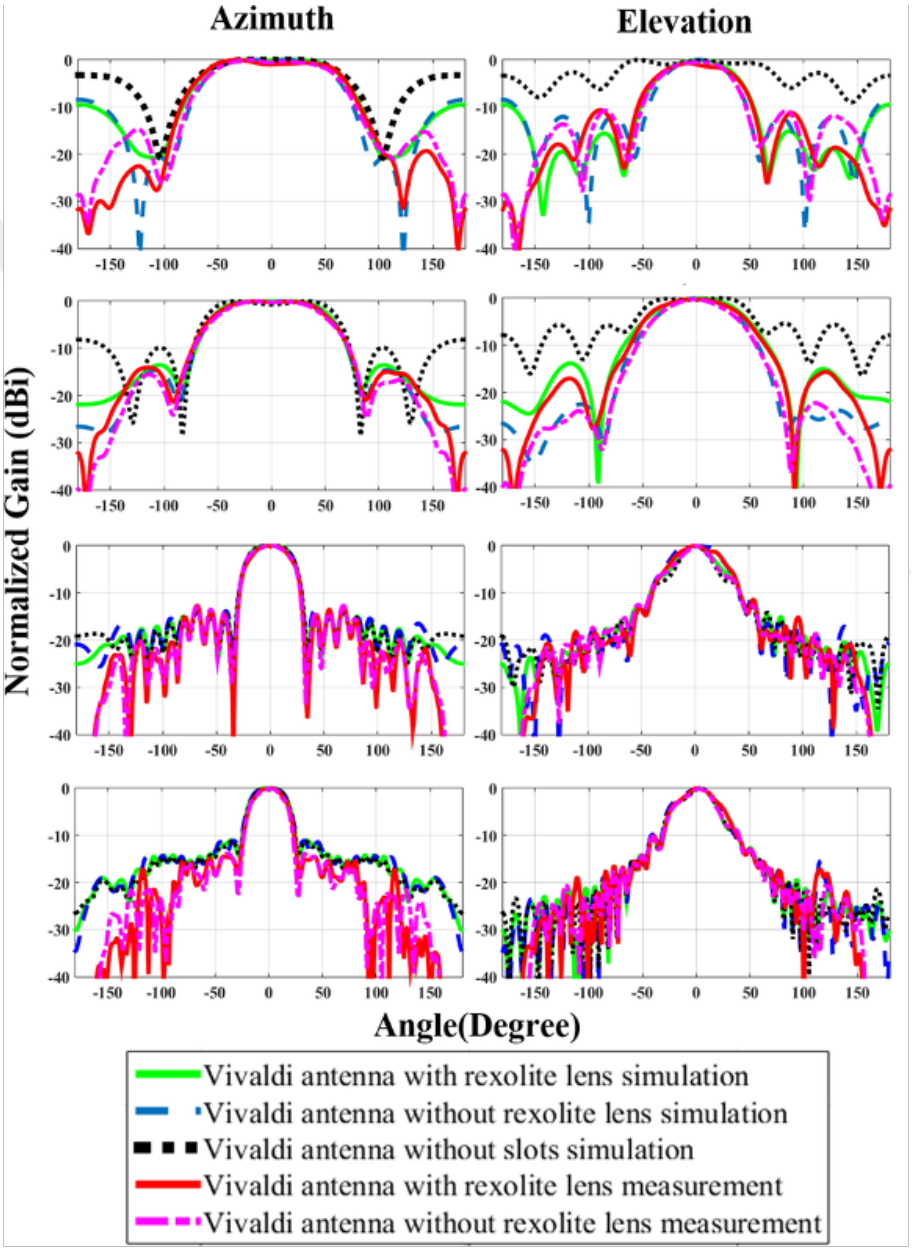


Figure 3.18 Comparison of Simulated and Measured Antenna Radiation Patterns at 1.5 GHz, 2 GHz, 8 GHz, and 12 GHz

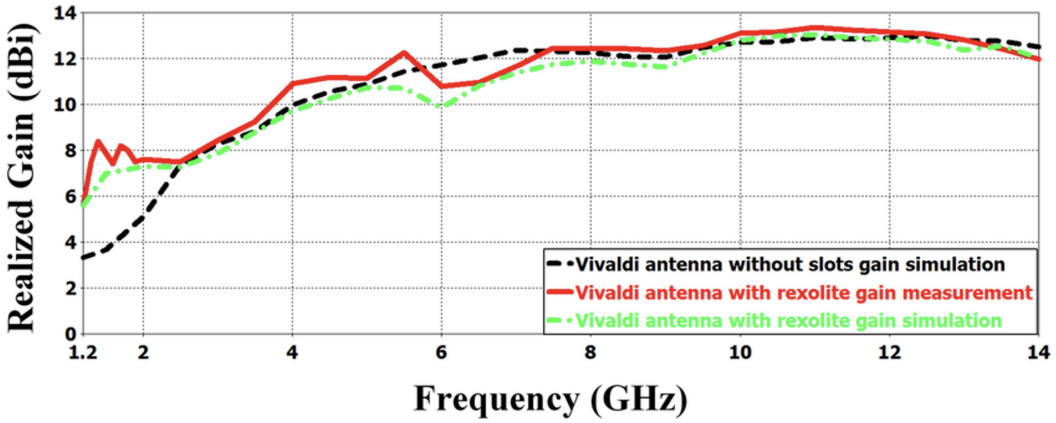


Figure 3.19 The proposed antenna gain comparison

In Figure 3.18, the simulation and measurement results of the radiation pattern of the proposed antenna can be seen. The designed antenna without slots provides a directional pattern above 2GHz. On the other hand, SEMVA provides directional radiation patterns characteristic of both E- and H-planes below 2 GHz. Also, by inserting *Rexolite* into the slots, the proposed antenna's elevation half-power beamwidth increased from 58.2 degrees to 67.9 degrees at 1.5 GHz and 65.5 degrees to 79.5 degrees at 2 GHz, respectively. Additionally, it can be concluded that all types of designed antennas have very close radiation pattern characteristics above 2GHz. Figure 3.19 presents the simulated and measured antenna gains. The realized gain of the proposed antenna is at least 3 dBi higher than the reference model below 2 GHz. The proposed antenna gain is between 8 dBi and 13 dBi, reaching its maximum value of 13 dBi at 11 GHz.

Additionally, the SEMVA has a very stable group delay, as in Figure 3.15b. Only +/-1 ns is observed. Thus, it can be concluded that the proposed antenna, which has very stable flatness and low group delay, is suitable for ultra-wideband applications like ground penetrating radar.

Table 3.2 Performance comparison of the Vivaldi antennas

Ref. no.	Dimensions ($\lambda_1 \times \lambda_2 \times \lambda_3$)	Dimensions (mm)	BW (GHz)	Gain (dBi)	Material	Permittivity	Group delay
[37]	$1.4 \times 0.24 \times N.M.$[a]	$140 \times 24 \times N.M.$[a]	3–18	3.4–8.7	All-Metal	N.A.[b]	N.M.[a]
[38]	$1.11 \times 0.67 \times 0.002$	$202 \times 120 \times 0.508$	1.65–18	6.7–14.9	Rogers 4003C	3.38	N.M.[a]
[39]	$1.27 \times 0.28 \times 0.002$	$190 \times 42 \times 0.28$	2–18	0.93–15.5	PCB (N. M.[a])	N.A.[b]	N.M.[a]
[40]	$1.62 \times 0.93 \times 0.008$	$72 \times 41 \times 0.381$	5.4–18	9–13	Rogers 5880	2.2	N.M.[a]
[41]	$0.96 \times 0.5 \times 0.003$	$96 \times 50 \times 3.15$	3–18	5–14.7	Arlon AD255	2.55	± 0.5 ns
[40]	$1.69 \times 0.2 \times 0.03$	$258.4 \times 29.7 \times 4.6$	2–6	-2.5 to -2.2	All-Metal	N.A.[b]	N.M.[a]
[42]	$0.32 \times 0.32 \times 0.006$	$40 \times 45 \times 0.8$	2.45–15.2	4.6–9.3	FR4	4.4	± 0.5 ns (over 1.5 ns peak around 2.5 GHz)
[43]	$0.51 \times 0.44 \times 0.019$	$42 \times 36 \times 1.6$	3.7 to > 18	1.8–6.9	FR4	N. M.[a]	Nearly flat (narrow band discontinuities occurred up to 5 ns)
[44]	$0.7 \times 0.35 \times 0.015$	$140 \times 70 \times 3$	1.5–15	4.5–12.6	Arlon Dilacl880	2.2	± 0.25 ns (narrow band discontinuity occurred up to 0.5 ns)
This work	$\mathbf{0.83 \times 0.44 \times 0.02}$	$\mathbf{182 \times 96 \times 6.1}$	**1.38–13.8**	**8–13**	**All-Metal**	**N.A.**[b]	± 1 **ns**

[a]Not mentioned.
[b]Not available.

The proposed antenna is compared with the other Vivaldi antennas in the literature regarding dimension, substrate material, bandwidth, and group delay results, as shown in Table 3.2. The proposed antenna performs superior to the all-metal Vivaldi antenna in References [37, 45] regarding the minimum and maximum gains, operating bandwidth, and dimension by length. Moreover, compared with the referenced Vivaldi antennas in references [38, 39, 41, 43, 44], the proposed Vivaldi antenna has the highest gain at the lower operating frequency and minimum gain deviation according to the bandwidth. Although in reference [40], the proposed antennas have similar gains, SEMVA has smaller dimensions regarding the wavelength and wider operating bandwidth. The proposed antenna has a nearly flat group delay response, as shown in Figure 3.15. According to Table 3.2, compared with the referenced Vivaldi antennas in references [41, 42, 44], the proposed antenna has a similar group delay response. Hence, in the study of reference [43], the group delay response of the Vivaldi antenna has a flat response with narrowband discontinuities up to 5 ns.

3.4 Mechanical Design Considerations for Harmonic Beamforming Systems

One of the most critical parameters in the beamforming measurement system is resolution, which directly impacts the image of the target. According to the experimental results, if the distance between the antennas is too close, the scanning system will take too long to complete a scan. On the other hand, the resolution is lost if the distance between the antennas is too wide. Placing the receiving antennas 3 cm apart with a scanning distance of 90 cm provides optimum resolution.

The scanning system is constructed with a sigma profile for robustness and mobility. The precise movement of the receive antenna is achieved by the dc step motor and ball screw, as seen in Figure 3.22.

The measurement system is designed via *Solidworks* 3D mechanical design tool, as seen in Figure 3.20. The transmit antenna and receive antenna are located 76.5 cm and 114.5 cm above the ground floor, respectively. The receiving antenna is automated to slide at 3 cm intervals at a distance of 90 cm from the measurement line. The system collects data from 31 points in one scan, which takes approximately 3 minutes. This time provides a significant advantage compared to the manual adjustment system where the first measurements were made. A measurement performed with the manual adjustment system takes approximately 3 hours.

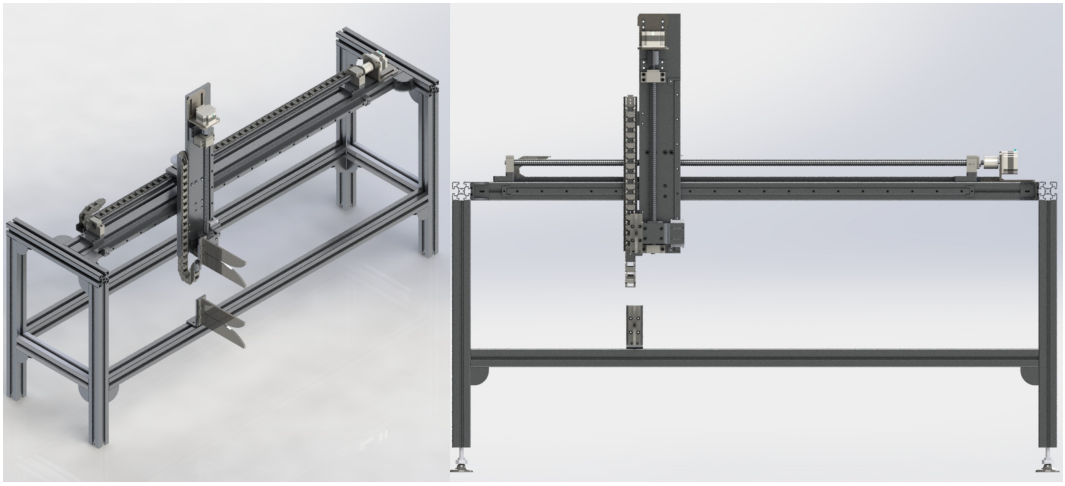


Figure 3.20 Perspective view of the mechanical design model of the HBF scanning system

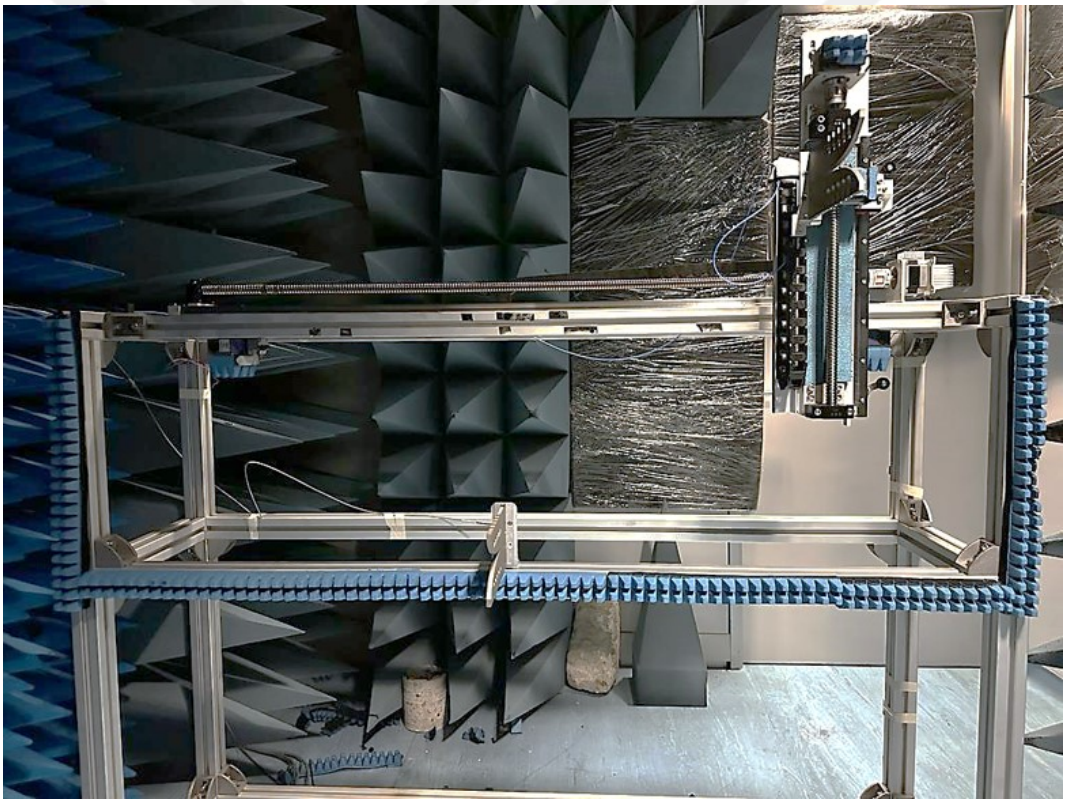


Figure 3.21 Constructed HBF scanning system

Step motors have been utilized in the scanning system. Parameters such as motor rotation number, torque, and antenna position information are transferred to the *Welmex* motor control unit via *Matlab* software in a computer environment.

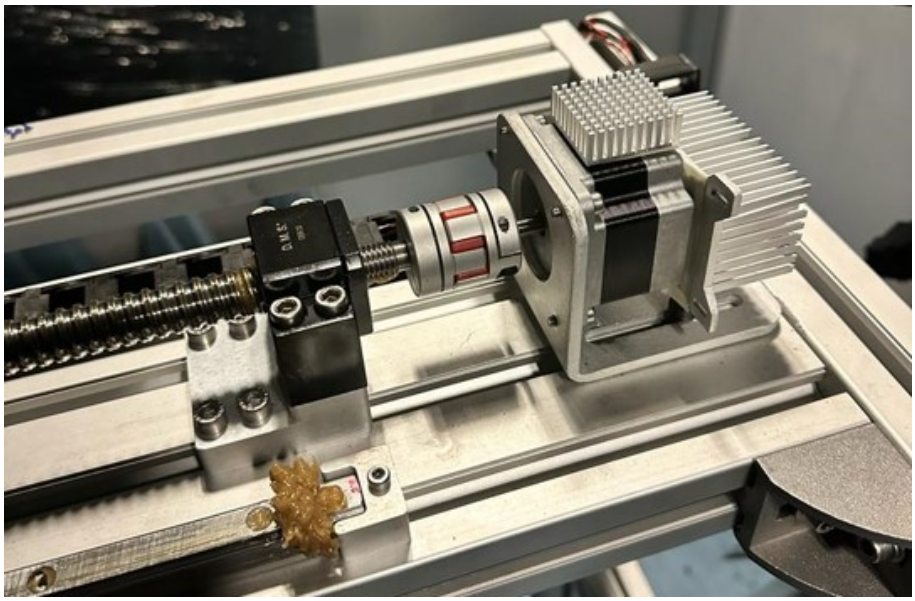


Figure 3.22 Step motor integration

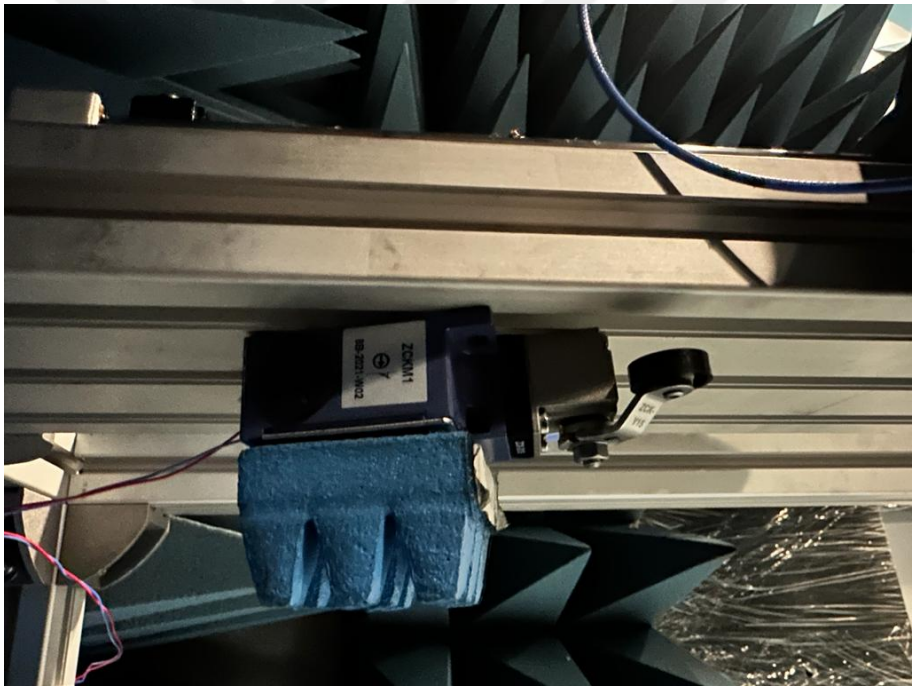


Figure 3.23 HBF-2 system mechanical switch

The calibration process is carried out just before the system starts collecting data. Mechanical switches have been established on both sides to verify the receiving antenna location and prevent system malfunction during the calibration and data acquisition process, as seen in Figure 3.23. Thus, as a result of the calibration process, the accuracy of each measurement is guaranteed.

4
MICROWAVE IMAGING AND ADAPTIVE BEAMFORMING TECHNIQUES

Beamforming is a method used in arrayed sensors for directional signal transmission or reception [46]. Additionally, this is a common and still promising technique in array signal processing to suppress unwanted signals and clutter from the environment. By utilizing the beamforming technique in an array, the SNR of the system is significantly improved. The beamforming technique collects the signal envelope in the array as a vector. The desired signal from a specific direction is included in the final output upon applying a weight vector to the incoming array signals, as illustrated in Figure 4.1. In addition, background noise and interference with various directions are effectively suppressed [47]. Consequently, the beamformers' key concepts include array geometry, phase and amplitude weighting, and signal directionality (steering and nulling).

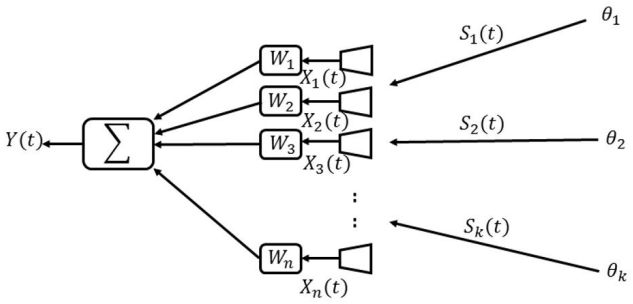


Figure 4.1 N-th element array arriving signals

Consider a ULA with N equally spaced antenna elements. The spacing between array elements is d, typically half the wavelength $\lambda/2$ of the incoming signal for spatial sampling without aliasing.

1. **Steering Vector**: The steering vector $\mathbf{a}(\theta)$ represents the phase differences of an incoming signal at each array (a.k.a antenna) element due to the geometry

of the array and the angle of arrival θ of the signal. For a given ULA, the steering vector can be expressed as:

$$\mathbf{a}(\theta) = \begin{bmatrix} 1 \\ e^{-j2\pi \frac{d}{\lambda} \sin(\theta)} \\ e^{-j2\pi \frac{2d}{\lambda} \sin(\theta)} \\ \vdots \\ e^{-j2\pi \frac{(N-1)d}{\lambda} \sin(\theta)} \end{bmatrix}$$

2. **Received Signal Model**: The signal received by the array, $\mathbf{x}(t)$, is a combination of the signal of interest, noise, and possible interference. It can be modeled as:

$$\mathbf{x}(t) = s(t)\mathbf{a}(\theta) + \mathbf{n}(t) \tag{4.1}$$

where $s(t)$ is the signal of interest and $\mathbf{n}(t)$ represents noise and interference.

Adaptive beamforming dynamically adjust the weights of the each antenna element. This tunining enhances thereception of the signal from the desired direction while minimizing interference and noise from other directions.

1. **Weight Vector**: A weight vector $\mathbf{w}$ is applied to the received signal. This vector is adaptive and calculated to control the beam pattern of the array. The weighted output of the array is given by:

$$y(t) = \mathbf{w}^H \mathbf{x}(t) \tag{4.2}$$

where $\mathbf{w}^H$ is the Hermitian transpose (conjugate transpose) of the weight vector.

2. **Optimization**: The weight vector $\mathbf{w}$ is often chosen in order to maximize the Signal-to-Interference-plus-Noise Ratio (SINR). In the simplest case (without considering specific algorithms like SCB or LCMV), this can be a simple phase alignment based on the steering vector. Still, more sophisticated approaches involve solving optimization problems that consider the signal and interference statistics.

This section formally describes the image formation algorithms used in this study. The delay and sum algorithm, capon algorithm, robust capon algorithm and

beamforming algorithm based on radial basis function (RBF) neural network is investigated and compared for image formation. Experimental studies are carried out in a free space medium for both linear and nonlinear scatterers, and the results are given in Section 5.

4.1 Delay and Sum Algorithm (DSB)

The Delay-and-Sum algorithm is the most fundamental beamforming technique in array signal processing. It is valued for its simplicity and direct approach to align signals from a particular direction. The main idea behind DSB is to time-align signals received at each antenna element so that signals from a target direction are constructively superimposed [48].

The essence of DSB in ULAs lies in manipulating the directionality of the antenna array's beam. In a ULA, N antennas are linearly arranged at equidistant intervals, d. $s(t) = A(t) \cdot e^{j(2\pi ft+\phi)}$ represents the signal at each antenna, with $A(t)$, f, and ϕ denoting the amplitude, frequency, and phase, respectively.

The DSB process in a ULA involves applying specific time delays to the signals received by each antenna. These delays align the signals from the target direction in phase at the array's output, enhancing signal clarity and strength. The time delay τ for the n-th element is given by $\tau_n = \frac{n \cdot d \cdot \sin(\theta)}{c}$, with θ as the steering angle and c as the speed of light.

The resultant output signal of the ULA is thus:

$$S_{\text{out}}(t) = \sum_{n=1}^{N} s_n(t - \tau_n) \tag{4.3}$$

This equation emphasizes the summation of the time-adjusted signals from each antenna, focusing the beam in the desired direction.

In practice, the delay for each antenna element is applied after digitizing the received signals. The time delays correspond to phase shifts in the frequency domain, implemented using digital signal processing techniques like the Fast Fourier Transform (FFT).

While the Delay-and-Sum method is advantageous for its simplicity and effectiveness, it does not discriminate between desired signals and noise or interference. DSB's higher side lobe level and lower resolution make it impractical

in highly cluttered scenarios. This makes it most suitable for scenarios with either low interference or when used with additional signal processing methods.

The Delay-and-Sum beamformer is extensively employed in the area of sonar [49], radar [50], and medical ultrasound imaging [51, 52]. Its ability to reinforce the signal from a known direction is crucial in many practical applications. Here, the beampatterns generated by the DSB algorithm for a single source signal and uncorrelated signals from three different directions are analyzed below as shown in Figure 4.2. The single source signal impinging from a $30°$ angle, while the uncorrelated 3 signals come from $-50°$, $0°$, and $30°$, respectively.

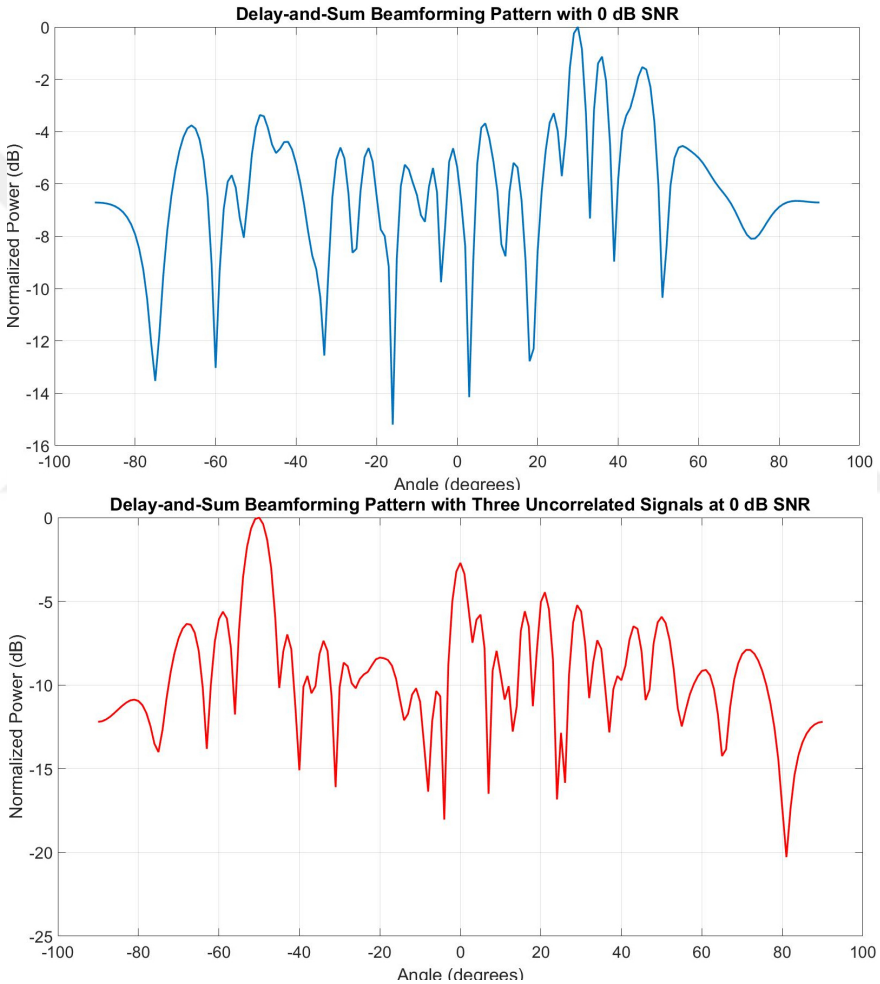


Figure 4.2 DSB beam pattern for a single source signal at $30°$ with SNR level of 0 dB (top), DSB beam patterns for three uncorrelated signals for $-50°$, $0°$, and $30°$ degree at SNR level of 0 dB, respectively (bottom)

In Figure 4.3, the analysis below focuses on the beam patterns produced by the DSB algorithm in response to uncorrelated signals originating from three distinct directions from the angles of $-10°$-$0°$-$10°$. The amplitudes of 1, 2, and 1 are examined under conditions where the SNR is maintained at 0 dB.

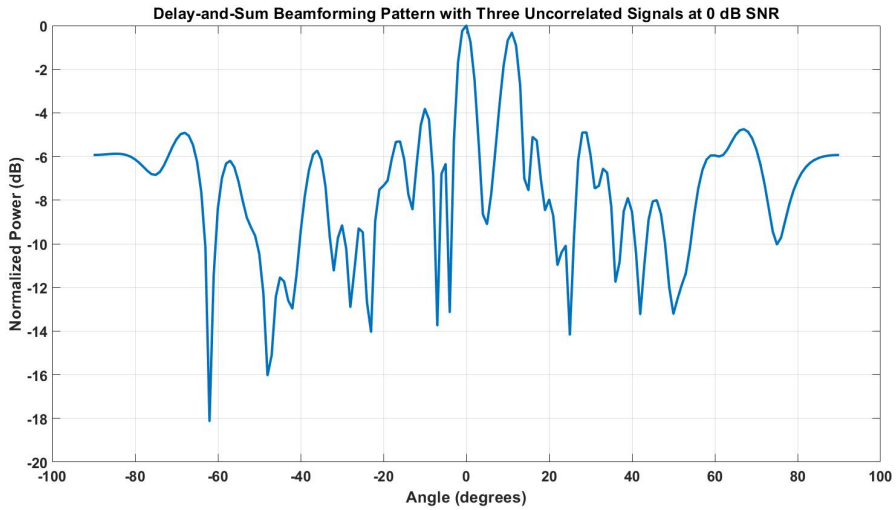


Figure 4.3 Beamforming result with 0 dB SNR from $-10°$-$0°$-$10°$ angles

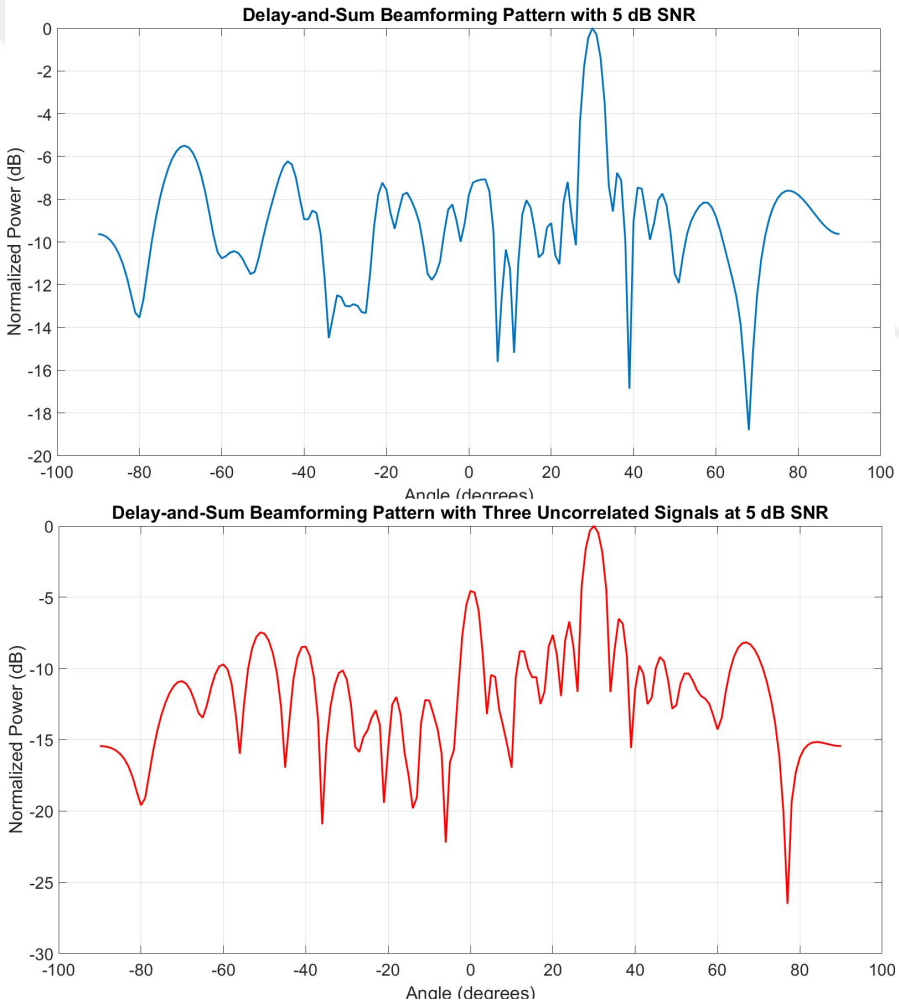


Figure 4.4 DSB beam pattern for a single source signal at $30°$ with SNR level of 5 dB (top), DSB beam patterns for three uncorrelated signals for $-50°$, $0°$, and $30°$ degree at SNR level of 5 dB, respectively (bottom)

In Figure 4.4 represents the beampatterns generated by the DSB algorithm for a single directional signal and uncorrelated signals from 3 different directions. The signal impinging from a 30° angle, while the uncorrelated 3 signals impinging from -50°, 0°, and 30°, respectively.

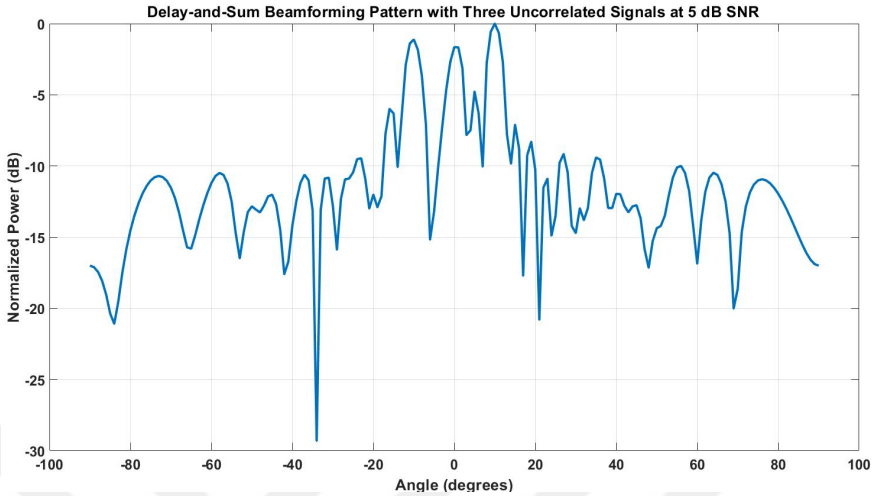


Figure 4.5 Beamforming result with 5 dB SNR from -10°-0°-10° angles

In Figure 4.5, the analysis focuses on the beam patterns produced by the DSB algorithm in response to uncorrelated signals originating from three distinct directions, specifically at angles of -10°-0°-10°. These signals, with amplitudes of1, 2, and 1 respectively, are examined at SNR level of 5 dB.

Here, the beampatterns generated by the DSB algorithm for a single directional signal and uncorrelated signals from 3 different directions are analyzed below as shown in Figure 4.6. The signal impinging from a 30° angle, while the uncorrelated 3 signals come from -50°, 0°, and 30°, respectively.

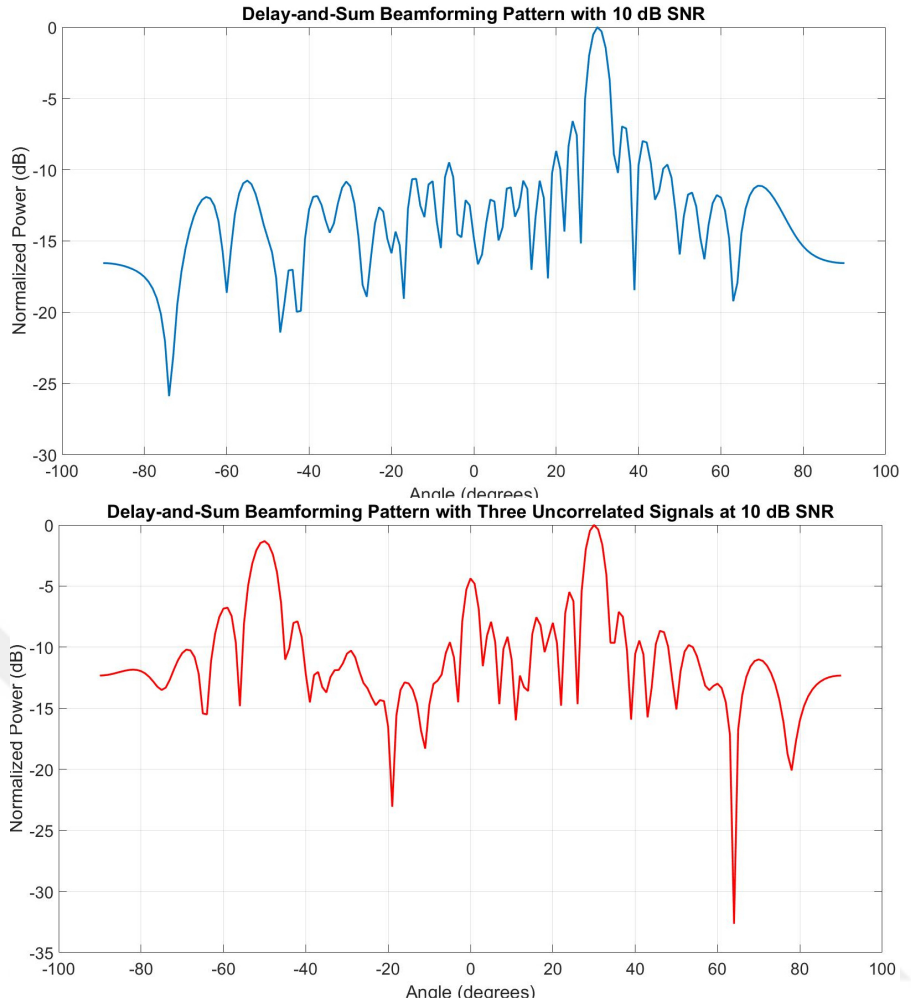


Figure 4.6 DSB beam pattern for a single source signal at $30°$ with SNR level of 10 dB (top), DSB beam patterns for three uncorrelated signals for $-50°$, $0°$, and $30°$ degree at SNR level of 10 dB, respectively (bottom)

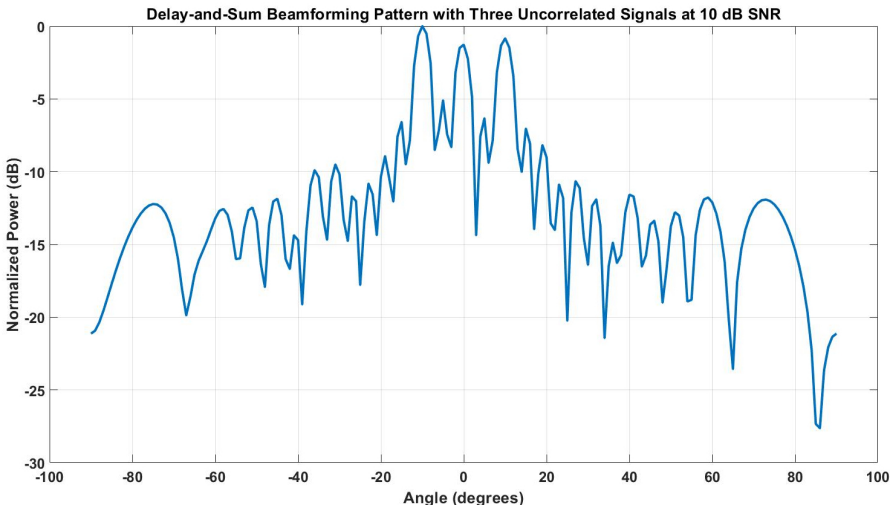


Figure 4.7 Beamforming result with 10 dB SNR from $-10°$-$0°$-$10°$ angles

In Figure 4.7, the analysis focuses on the beam patterns produced by the DSB algorithm in response to uncorrelated signals originating from three distinct directions, specifically at angles of $-10°$-$0°$-$10°$. These signals, with amplitudes of 1, 2, and 1 respectively, are examined at SNR level of 10 dB.

Below in Figure 4.8 the signal is impinging from a $30°$ angle, while the uncorrelated 3 signals are impinging from $-50°$, $0°$, and $30°$, respectively.

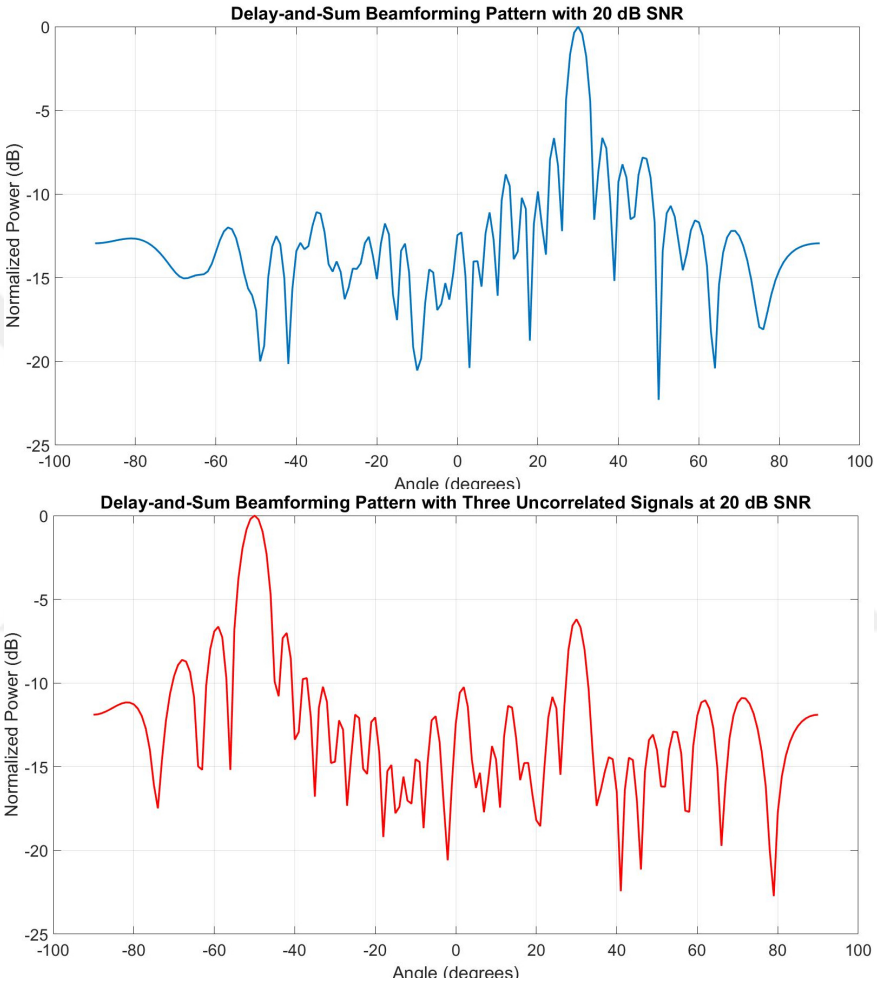


Figure 4.8 DSB beam pattern for a single source signal at $30°$ with SNR level of 20 dB (top), DSB beam patterns for three uncorrelated signals for $-50°$, $0°$, and $30°$ degree at SNR Level of 20 dB, respectively (bottom)

In Figure 4.9, the analysis below focuses on the beam patterns produced by the DSB algorithm in response to uncorrelated signals originating from three distinct directions, specifically at angles of $-10°$-$0°$-$10°$. These signals, with amplitudes of 1, 2, and 1 respectively, are examined at SNR level of 20 dB.

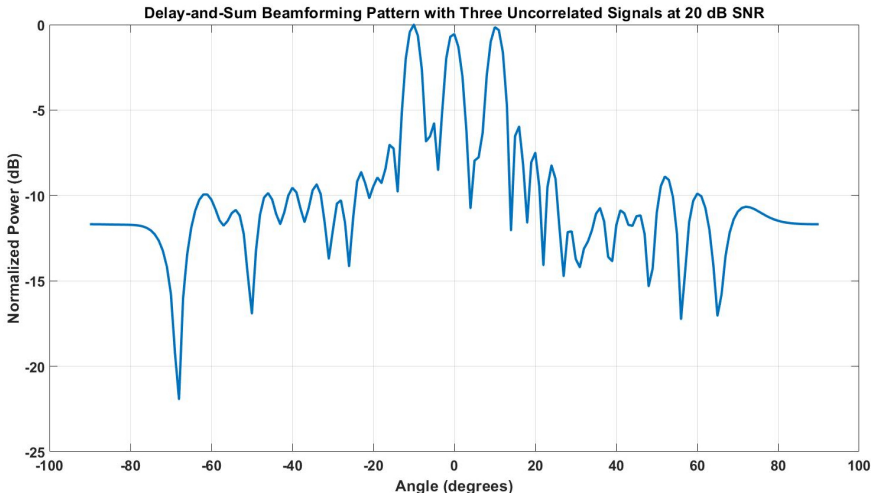


Figure 4.9 Beamforming result with 20 dB SNR from $-10°$-$0°$-$10°$ angles

According to the results, the DSB algorithm can detect single and multiple uncorrelated signals. The ability to detect multiple uncorrelated signals depends on the array design, signal-to-noise ratio (SNR), and the spatial separation of the signals (i.e., how far apart they are in angle).

The DSB algorithm works by time-aligning signals from a specific direction and summing them together. For uncorrelated signals, which have no correlation, the DSB could work but with limitations like SNR, array structure, and signal conditions.

The Delay-and-Sum algorithm is a stepping stone to more sophisticated adaptive beamforming techniques. It provides a baseline understanding necessary for exploring advanced algorithms such as Capon (SCB) and Robust Capon, which are adapted to the signal environment to improve performance. It will be discussed in subsequent sections.

4.2 Capon Algorithm (SCB)

Conventional beamformers, such as Delay and Sum beamformers, apply uniform weighting to the signals for each array element and primarily use phase shifting for beam steering. Nevertheless, such beamformers have limited ability to suppress interference and noise, especially in complex clutter environments. This limitation has led to adaptive beamforming techniques, among which the Capon or SCB beamformer stands out.

The theoretical background of the SCB beamformer depends on minimizing the output power of the beamformer while ensuring a distortionless response in the

desired signal's direction [53]. The objective of the Capon beamforming algorithm is to minimize P_{i+n} while maintaining a distortionless response in the direction of the desired signal, typically constrained as $\mathbf{w}^H\mathbf{a}_0 = 1$ where $\mathbf{a}_0$ is the steering vector towards the desired signal. The aim of the SCB could be expressed as the power of interferences and noise at the output is given by:

$$P_{i+n} = \mathbf{w}^H\mathbf{R}_{i+n}\mathbf{w} \tag{4.4}$$

where:

- P_{i+n} is the power of interferences and noise.
- $\mathbf{w}$ is the complex weight vector applied by the beamformer to the array input.
- $\mathbf{R}_{i+n}$ is the covariance matrix of interferences and noise, encapsulating the combined second-order statistics of the interference and noise across the array elements.

The covariance matrix $\mathbf{R}_{i+n}$ is defined as:

$$\mathbf{R}_{i+n} = \sum_{i=2}^{M} \mathbf{a}_i \mathbb{E}[s_i s_i^H]\mathbf{a}_i^H + \sigma_n^2\mathbf{I} \tag{4.5}$$

where:

- $\mathbf{a}_i$ are the steering vectors for the interferences.
- s_i are the interference signals.
- σ_n^2 is the noise power.
- $\mathbf{I}$ is the identity matrix.
- $\mathbb{E}[\cdot]$ represents the expectation operator.

Minimizing the output power of interference and noise improves the Signal-to-Interference-plus-Noise Ratio (SINR) of the signal received by the array, which is necessary to improve the quality and intelligibility of the desired signal in the presence of noise and interference.

In practical application, the noise correlation matrix and interference are not available. Thus, the whole array covariance matrix is used to determine weights.

$$\min_{\mathbf{w}} \mathbf{w}^H \mathbf{R} \mathbf{w} \tag{4.6}$$

$$\text{Subject to:} \quad \mathbf{w}^H \mathbf{a}(\theta_0) = 1 \tag{4.7}$$

where;

- $\mathbf{w}$ is the weight vector applied to the array elements.
- $\mathbf{R}$ is the covariance matrix of the received signal.
- $\mathbf{a}(\theta_0)$ represents the array steering vector in the direction of the desired signal θ_0.
- The superscript H denotes the Hermitian transpose (conjugate transpose).

The covariance matrix $\mathbf{R}$ in the context of the Capon beamformer represents the auto-correlation matrix of the received signals across the array elements. Mathematically, it is defined as:

$$\mathbf{R} = \mathbb{E}\left[\mathbf{x}(t)\mathbf{x}^H(t)\right] \tag{4.8}$$

Where:

- $\mathbf{x}(t)$ is the received signal vector at the array as a function of time t.
- $\mathbb{E}[\cdot]$ denotes the expectation operator.
- The superscript H represents the Hermitian transpose.

The constraint $\mathbf{w}^H \mathbf{a}(\theta_0) = 1$ ensures a distortionless response in the direction of the desired signal, meaning the beamformer does not alter the signal's phase or amplitude in this direction.

To solve this constrained optimization problem, we apply the method of Lagrange multipliers. The Lagrangian is given by;

$$\mathcal{L}(\mathbf{w}, \lambda) = \mathbf{w}^H \mathbf{R} \mathbf{w} - \lambda(\mathbf{w}^H \mathbf{a}(\theta_0) - 1) \tag{4.9}$$

Where λ is the Lagrange multiplier. Differentiating $\mathcal{L}$ with respect to $\mathbf{w}^*$ and equating to zero, we get;

$$2\mathbf{R}\mathbf{w} - \lambda\mathbf{a}(\theta_0) = 0 \tag{4.10}$$

We seek to solve for the weight vector $\mathbf{w}$. The gradient of the Lagrangian $\mathcal{L}$ with respect to the weight vector $\mathbf{w}$ is given by:

$$\nabla_{\mathbf{w}}\mathcal{L} = 2\mathbf{R}\mathbf{w} - \lambda\mathbf{a}(\theta_0) \tag{4.11}$$

Setting the gradient to zero for optimally, we have:

$$2\mathbf{R}\mathbf{w} - \lambda\mathbf{a}(\theta_0) = 0 \tag{4.12}$$

Rearranging the terms, we obtain:

$$2\mathbf{R}\mathbf{w} = \lambda\mathbf{a}(\theta_0) \tag{4.13}$$

Multiplying both sides by the inverse of $2\mathbf{R}$, assuming $\mathbf{R}$ is non-singular and hence invertible, we get:

$$\mathbf{w} = \frac{\lambda}{2}\mathbf{R}^{-1}\mathbf{a}(\theta_0) \tag{4.14}$$

The value of λ can be determined by applying the constraint that the response of the beamformer in the direction of the desired signal is distortionless:

$$\mathbf{w}^H\mathbf{a}(\theta_0) = 1 \tag{4.15}$$

Substituting the expression for $\mathbf{w}$ into the constraint gives us:

$$\left(\frac{\lambda}{2}\mathbf{R}^{-1}\mathbf{a}(\theta_0)\right)^H \mathbf{a}(\theta_0) = 1 \tag{4.16}$$

Solving for λ yields:

$$\lambda = 2\frac{1}{\mathbf{a}^H(\theta_0)\mathbf{R}^{-1}\mathbf{a}(\theta_0)} \tag{4.17}$$

Finally, substituting back for λ in the expression for $\mathbf{w}$, we get the optimal weight vector:

$$\mathbf{w}_{\text{opt}} = \frac{\mathbf{R}^{-1}\mathbf{a}(\theta_0)}{\mathbf{a}^H(\theta_0)\mathbf{R}^{-1}\mathbf{a}(\theta_0)} \tag{4.18}$$

This is the optimal weight vector for the Capon beamformer that minimizes the output power of interferences and noise while maintaining a distortionless response in the direction of the desired signal.

The SCB adaptive beamformer technique is seen as a significant breakthrough over conventional techniques like DSB, as it can adaptively calculate and adjust the array weights, effectively suppress ambient noise, and significantly improve the signal-to-noise ratio in complex and dynamic signal environments. On the other hand, it has some limitations due to the necessity of continuous calculation of the covariance matrix, the dependence on the number of array elements, and the insufficient detection between correlated targets. The computational complexity of systems with large antenna array structures makes it impossible to use in real-time applications.

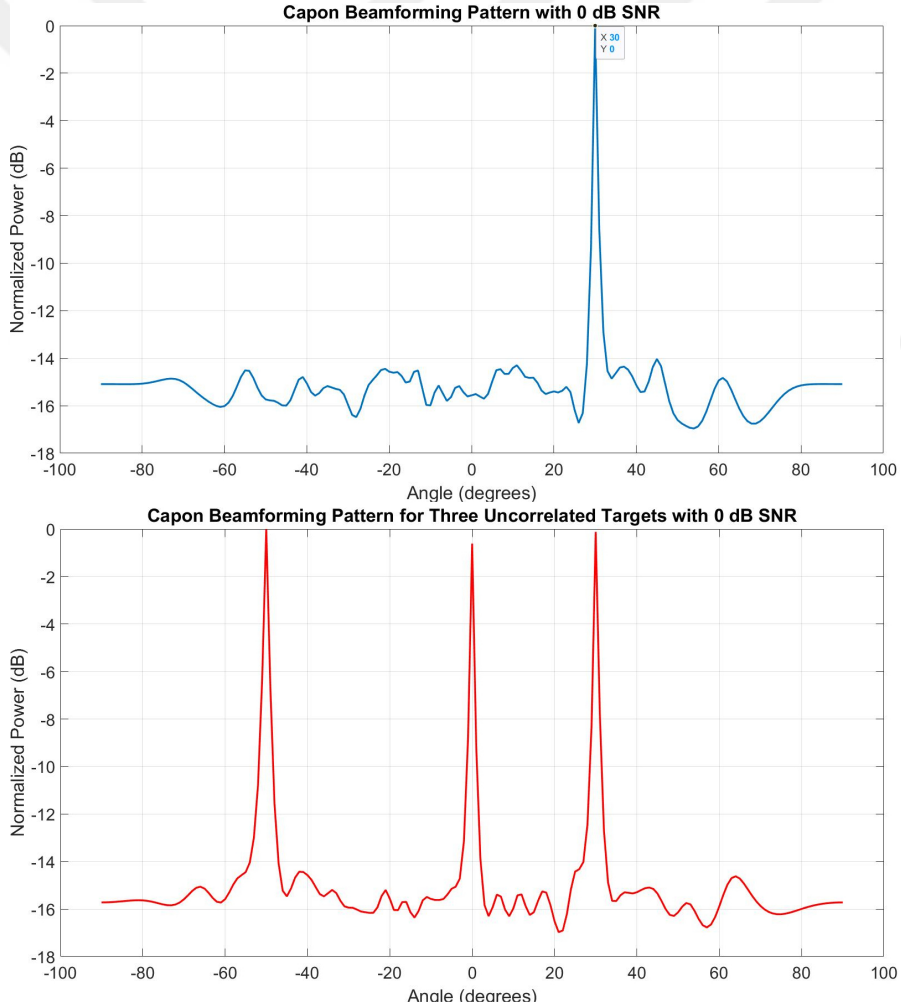


Figure 4.10 SCB beam pattern for a single source signal at $30°$ with SNR level of 0 dB (top), SCB beam patterns for three uncorrelated signals for $-50°$, $0°$, and $30°$ degree at SNR level of 0 dB, respectively (bottom)

Here in Figure 4.10, the beampatterns generated by the Capon (SCB) beamformer pattern have been examined for single source signal and uncorrelated signals from three different directions are analyzed below. The signal source signal is imping from a $30°$ angle, while the uncorrelated signals come from $-50°$, $0°$, and $30°$, respectively. The array sensor number is 31. The SNR is set to 0-5-10-20 dB respectively. The distance between the adjacent sensor elements equals half the wavelength of the narrowband signal.

In Figure 4.11, the analysis below focuses on the beam patterns produced by the SCB algorithm in response to uncorrelated signals originating from three distinct directions, specifically at angles of $-10°$-$0°$-$10°$. These signals, with amplitudes of 1, 2, and 1 respectively, are examined at SNR level of 0 dB.

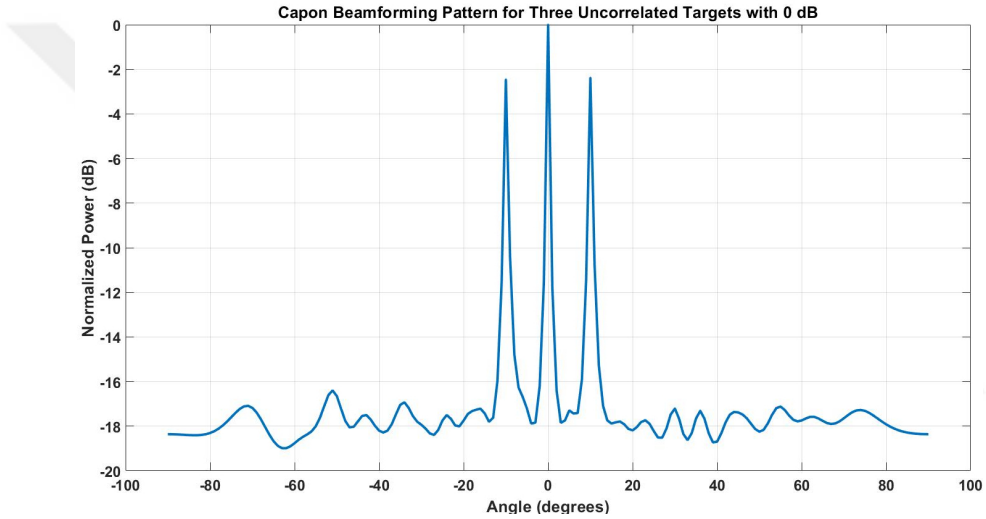


Figure 4.11 Beamforming result with 0 dB SNR from $-10°$-$0°$-$10°$ angles

As can be seen in Figure 4.12 the signal impinges from a $30°$ angle, while the uncorrelated 3 signals impinge from $-50°$, $0°$, and $30°$, respectively.

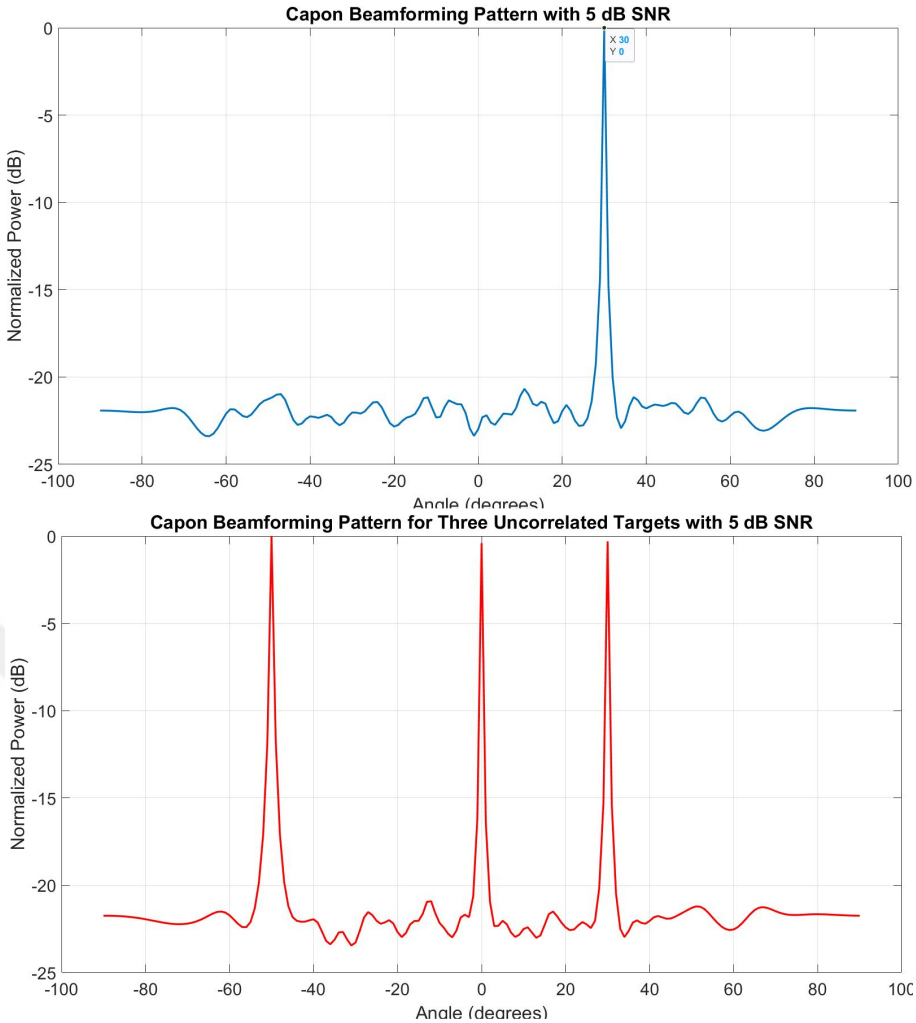


Figure 4.12 SCB beam pattern for a single source signal at $30°$ with SNR level of 5 dB (top), SCB beam patterns for three uncorrelated signals for $-50°$, $0°$, and $30°$ degree at SNR level of 5 dB, respectively (bottom)

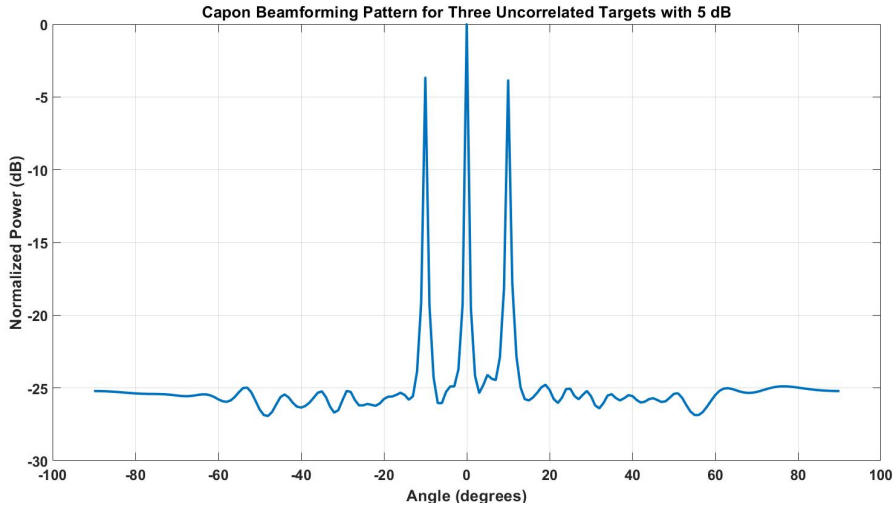


Figure 4.13 Beamforming result with 5 dB SNR from $-10°$-$0°$-$10°$ angles

In Figure 4.13, the analysis focuses on the beam patterns produced by the SCB algorithm in response to uncorrelated signals originating from three distinct directions, specifically at angles of $-10°$-$0°$-$10°$. These signals, with amplitudes of 1, 2, and 1 respectively, are examined at SNR level of 5 dB.

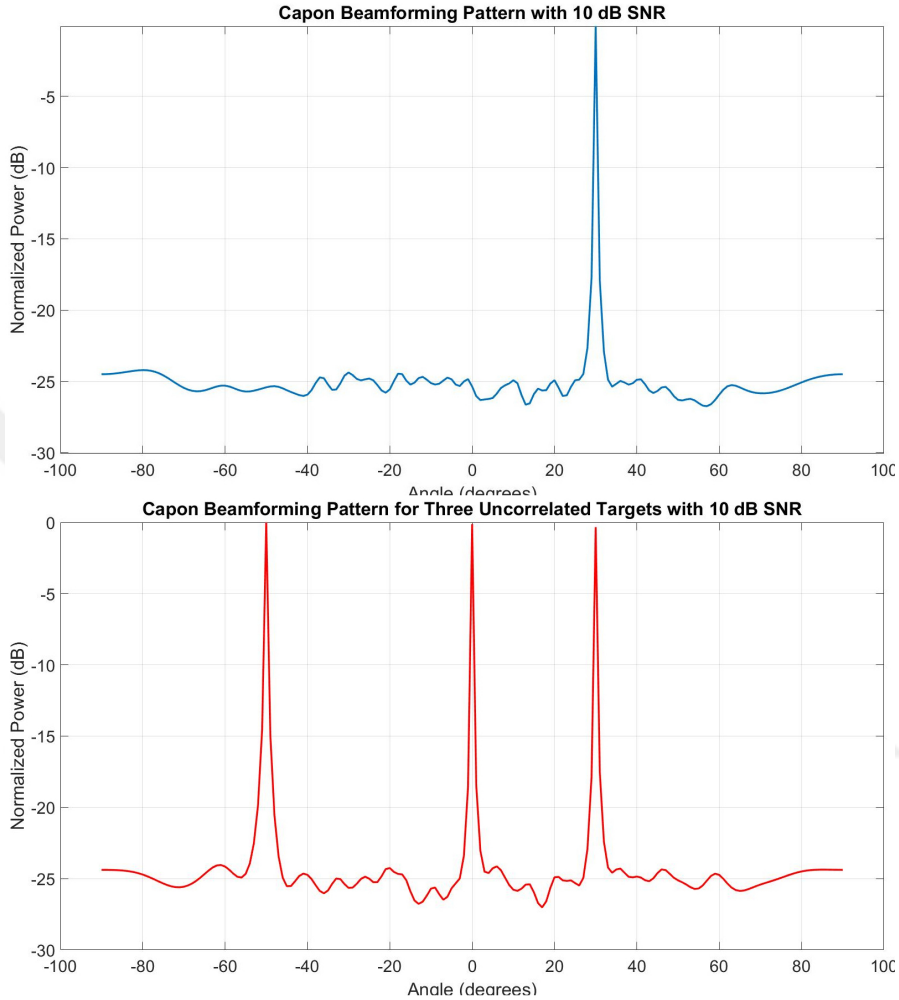


Figure 4.14 SCB beam pattern for a single source signal at $30°$ with SNR level of 10 dB (top), SCB beam patterns for three uncorrelated signals for $-50°$, $0°$, and $30°$ degree at SNR level of 10 dB, respectively (bottom)

In Figure 4.14, the SNR level of 10 dB examined. The signal impinges from $30°$ angle, while the uncorrelated 3 signals impinge from $-50°$, $0°$, and $30°$, respectively.

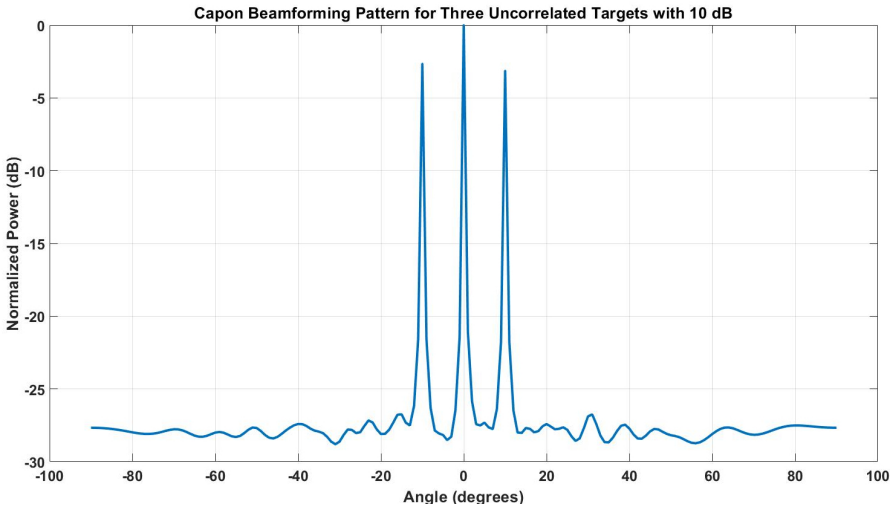


Figure 4.15 Beamforming result with 10 dB SNR from $-10°$-$0°$-$10°$ angles

In Figure 4.15, the analysis focuses on the beam patterns produced by the SCB algorithm in response to uncorrelated signals originating from three distinct directions, specifically at angles of $-10°$-$0°$-$10°$. These signals, with amplitudes of 1, 2, and 1 respectively, are examined at SNR level of 10 dB.

Below in Figure 4.16, the SNR level of 20 dB examined. The signal is impinging from a $30°$ angle, while the uncorrelated 3 signals are impinging from $-50°$, $0°$, and $30°$, respectively.

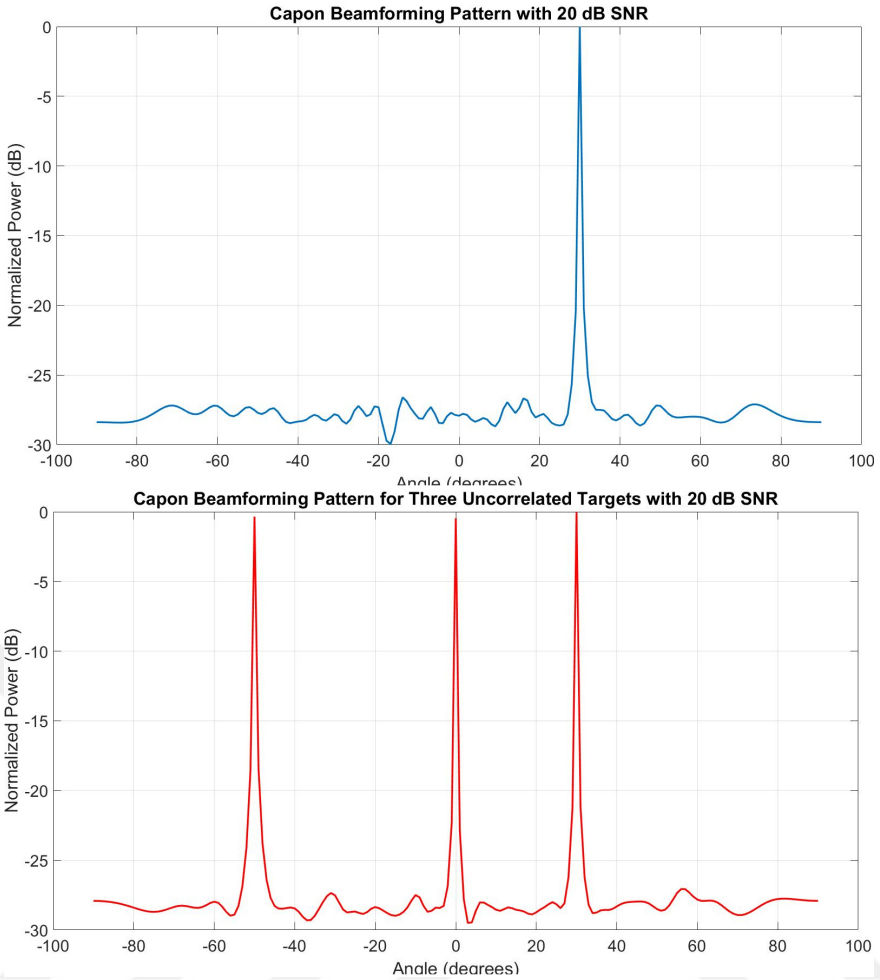


Figure 4.16 SCB beam pattern for a single source signal at $30°$ with SNR level of 20 dB (top), SCB beam patterns for three uncorrelated signals for $-50°$, $0°$, and $30°$ degree at SNR level of 20 dB, respectively (bottom)

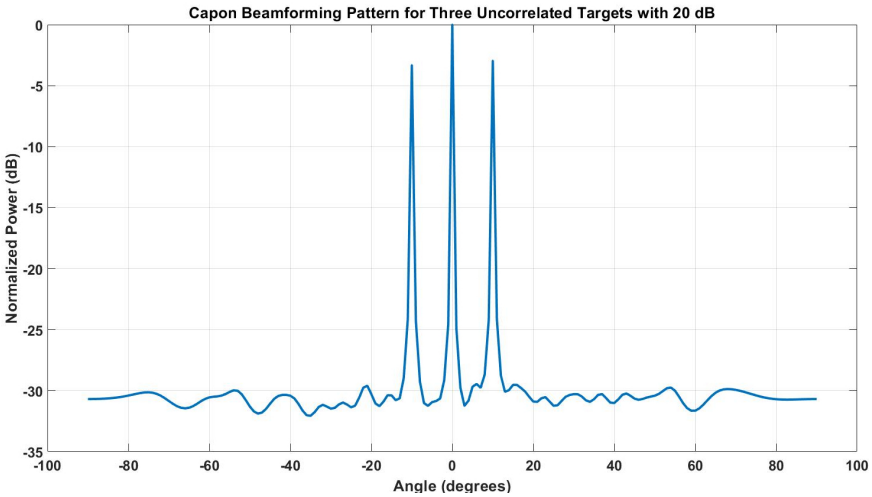


Figure 4.17 Beamforming result with 20 dB SNR from $-10°$-$0°$-$10°$ angles

In Figure 4.17, the analysis focuses on the beam patterns produced by the SCB algorithm in response to uncorrelated signals originating from three distinct directions, specifically at angles of $-10°$-$0°$-$10°$. These signals, with amplitudes of 1, 2, and 1 respectively, are examined at SNR level of 20 dB.

4.3 The Robust Capon Algorithm (RCB)

The robust capon algorithm is an extension and enhanced version of the classical SCB algorithm [54, 55]. The RCB is designed to maintain the optimum performance in cases where the array steering vector is unknown, array imperfections, environmental changes, and model inaccuracies. The RCB weights are found using the approach described in [54].

While the array pattern is as close as possible to the desired one, the power output is minimized by suppressing undesired environmental effects. The optimization problem for RCB can be expressed as follows;

$$\min_{\mathbf{w}} \mathbf{w}^H \mathbf{R} \mathbf{w} \tag{4.19}$$

Subject to;

$$\left| \mathbf{w}^H \mathbf{a}(\theta_0) - 1 \right| \leq \mathbf{e} \tag{4.20}$$

Here, e represents the bound on the array's uncertainty level, allowing some deviation from the distortionless response constraint.

Various methods have been established to improve the Capon beamformer robustness, such as diagonal loading matrix addition, where a scalar is added to the diagonal of the covariance matrix, or by formulating a worst-case performance optimization problem. One common approach is to add a small value to the diagonal elements of the covariance matrix $\mathbf{R}$, effectively increasing the noise estimate. This can be mathematically expressed as:

$$\mathbf{R}_{\text{robust}} = \mathbf{R} + \delta \mathbf{I} \tag{4.21}$$

where δ is a positive scalar and $\mathbf{I}$ is the identity matrix.

The identity matrix $\mathbf{I}$ is defined as a square matrix with ones on the main diagonal and zeros elsewhere. Using $\mathbf{I}$ does not alter the off-diagonal elements of the covariance matrix, $\mathbf{R}$. Thus, the main structure of the matrix does not changed, and also its diagonal elements are enhanced. Furthermore, adding

the regularization term ϵ in (4.22) prevents division by zero and stabilizes the beamformer's performance in mismatches and steering vector errors.

$$I_N = \begin{bmatrix} 1 & 0 & \cdots & 0 \\ 0 & 1 & \cdots & 0 \\ \vdots & \vdots & \ddots & \vdots \\ 0 & 0 & \cdots & 1 \end{bmatrix}_{N \times N}$$

where I_N is an $N \times N$ identity matrix, and the subscript $N \times N$ denotes the size of the matrix. The RCB uses a modified version of the Capon beamformer's solution. The weight vector is given by:

$$\mathbf{w}_{\text{opt, robust}} = \frac{\mathbf{R}_{\text{robust}}^{-1}\mathbf{a}(\theta_0)}{\mathbf{a}^H(\theta_0)\mathbf{R}_{\text{robust}}^{-1}\mathbf{a}(\theta_0) + \epsilon} \tag{4.22}$$

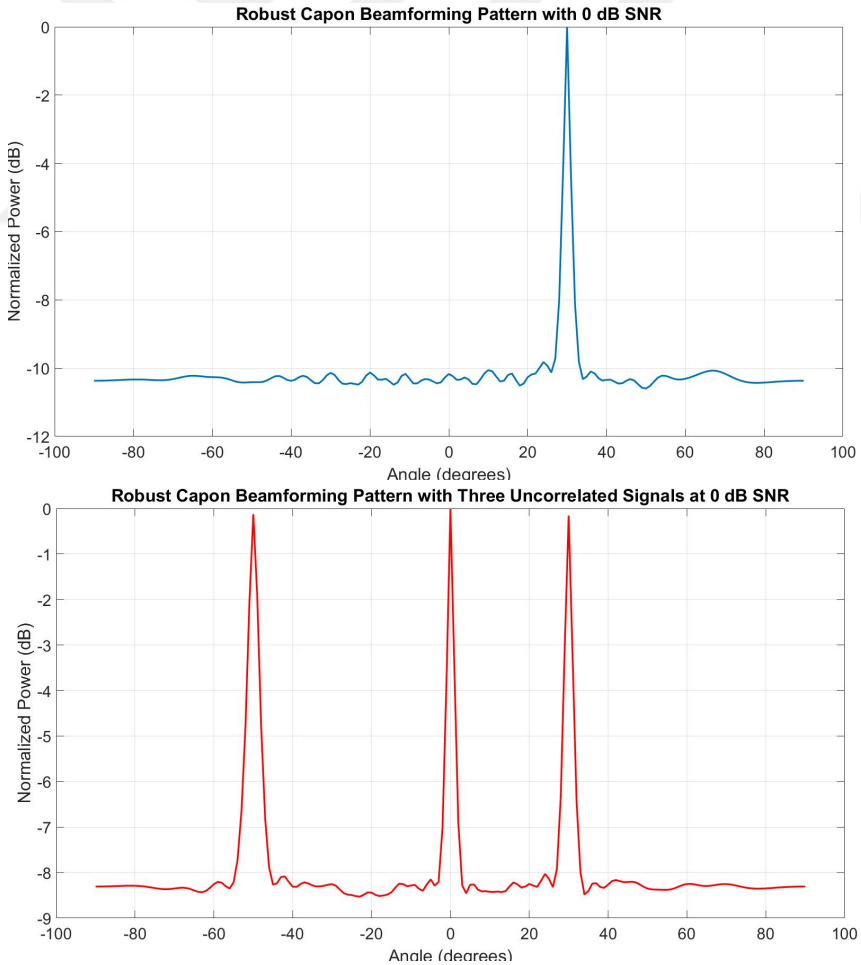


Figure 4.18 RCB beam pattern for a single source signal at $30°$ with SNR level of 0 dB (top), RCB beam patterns for three uncorrelated signals for $-50°$, $0°$, and $30°$ degree at SNR level of 0 dB, respectively (bottom)

The RCB beamformer 1-D patterns are generated and analyzed for unidirectional and uncorrelated signals from 3 different directions as shown in Figure 4.18. The AOA of a single source signal is $30°$, while the uncorrelated 3 signals arrive from $-50°$, $0°$, and $30°$, respectively. The array sensor number is 31. The SNR value is set to 0-5-10-20 dB respectively. The distance between the adjacent sensor elements equals half the wavelength of the narrow-band signal.

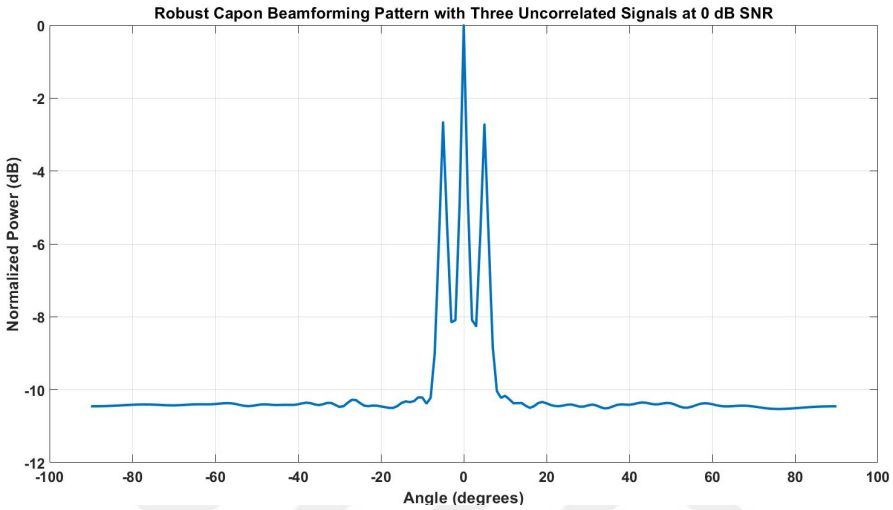


Figure 4.19 RCB Beamforming result with 0 dB SNR from $-10°$-$0°$-$10°$ angles

In Figure 4.19, the analysis focuses on the beam patterns produced by the RCB algorithm in response to uncorrelated signals originating from three distinct directions, specifically at angles of $-10°$-$0°$-$10°$. These signals, with amplitudes of 1, 2, and 1 respectively, are examined at SNR level of 0 dB.

According to the Figure 4.20, both single and uncorrelated signals can be seen. The first beam pattern represents the $30°$ signal, and the second graph illustrates the signals are impinging from the direction of $-50°$, $0°$, and $30°$ degree at SNR Level of 5 dB, respectively.

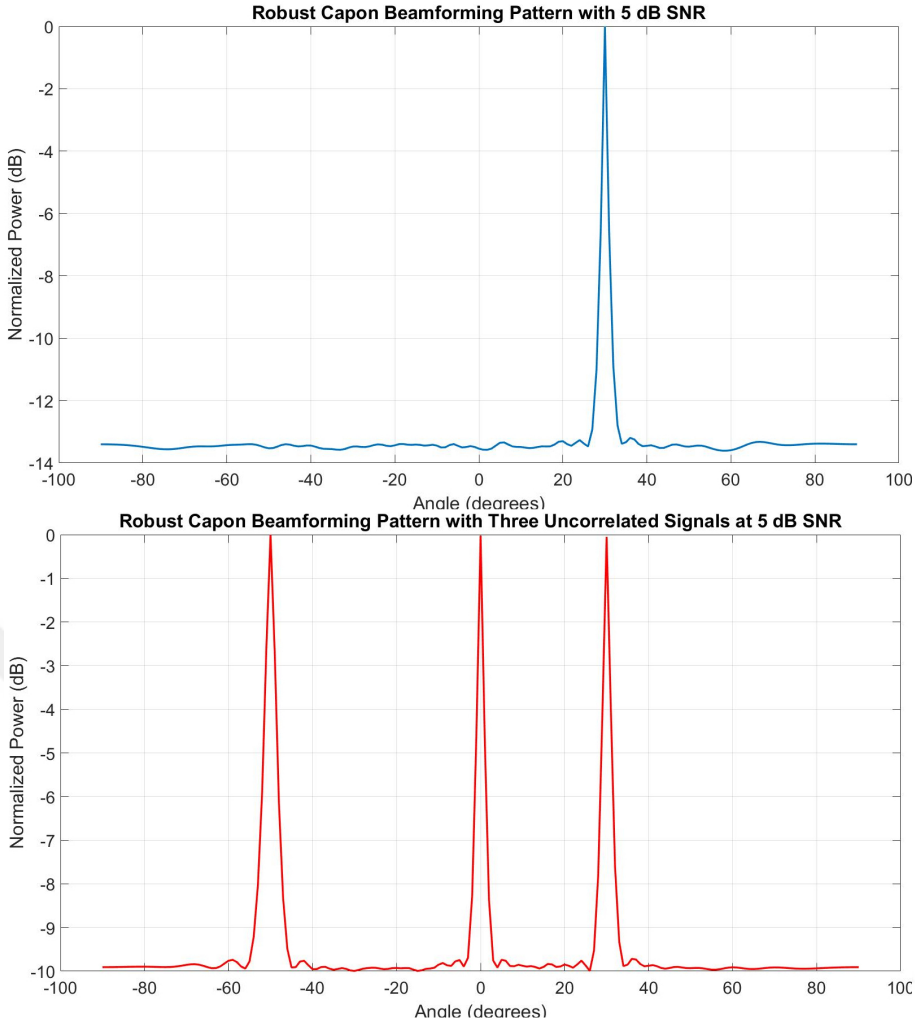


Figure 4.20 RCB beam pattern for a single source signal at $30°$ with SNR level of 5 dB (top), RCB beam patterns for three uncorrelated signals for $-50°$, $0°$, and $30°$ degree at SNR level of 5 dB, respectively (bottom)

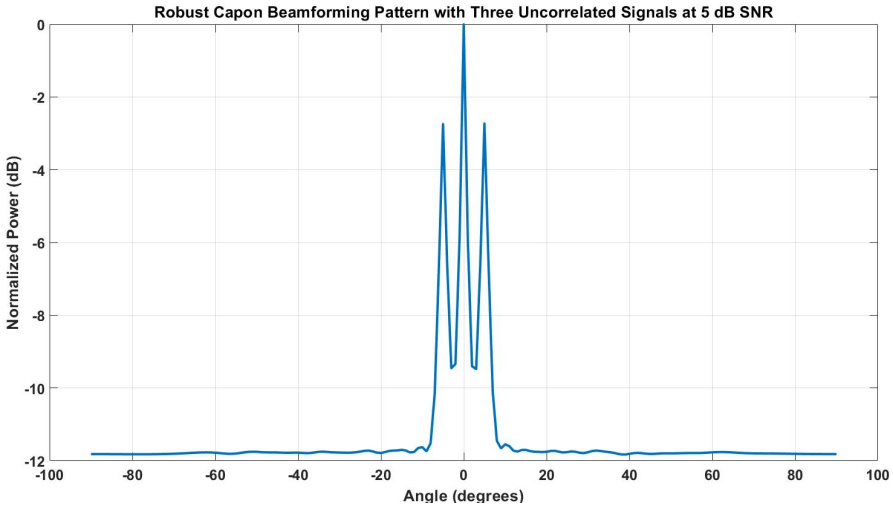


Figure 4.21 RCB Beamforming result with 5 dB SNR from $-10°$-$0°$-$10°$ angles

In Figure 4.21, the analysis below focuses on the beam patterns produced by the RCB algorithm in response to uncorrelated signals originating from three distinct directions, specifically at angles of $-10°$-$0°$-$10°$. These signals, with amplitudes of 1, 2, and 1 respectively, are examined at SNR level of 5 dB.

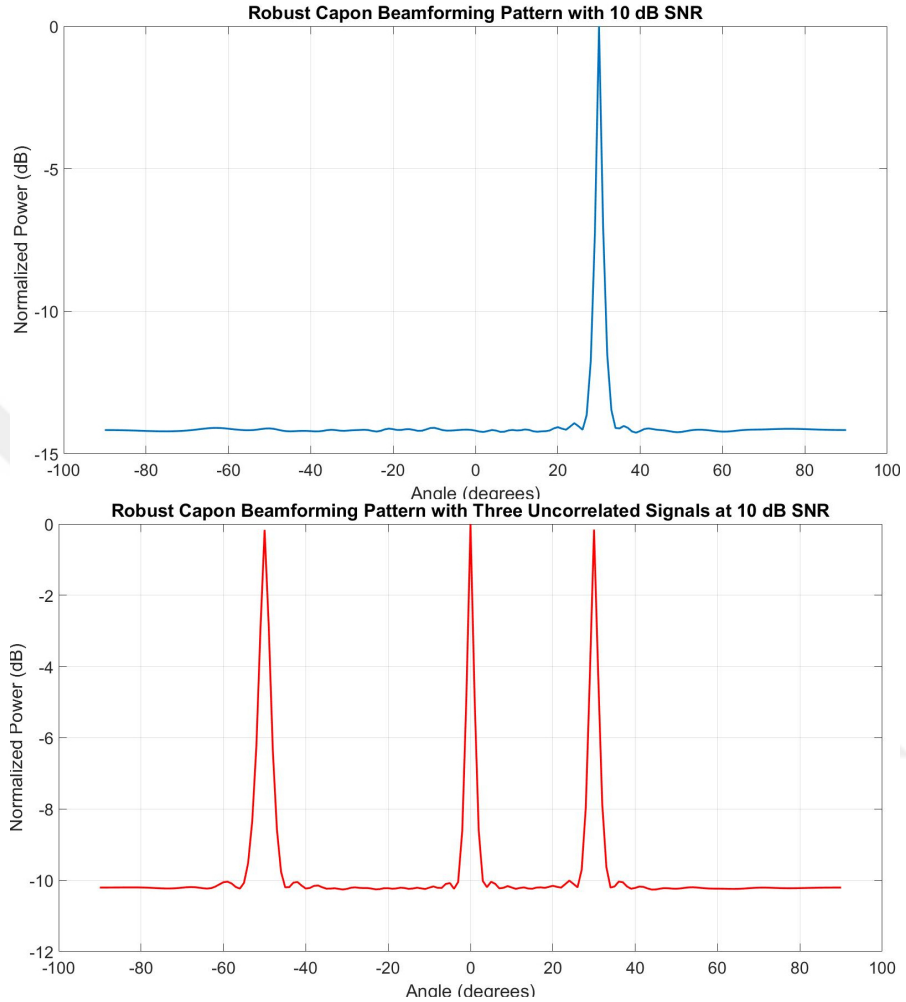


Figure 4.22 RCB beam pattern for a single source signal at $30°$ with SNR level of 10 dB (top), RCB beam patterns for three uncorrelated signals for $-50°$, $0°$, and $30°$ degree at SNR level of 10 dB, respectively (bottom)

As illustrated in Figure 4.22, both single and three uncorrelated signals have been employed to show RCB result in given SNR level, 10 dB.

The analysis shown in Figure 4.23 shows that the beam patterns produced by the RCB algorithm in response to the uncorrelated signals originating from three distinct directions, specifically from angles of $-10°$, $0°$, and $10°$. These signals with amplitudes of 1, 2 and 1 dB are analysed at SNR of 10 dB.

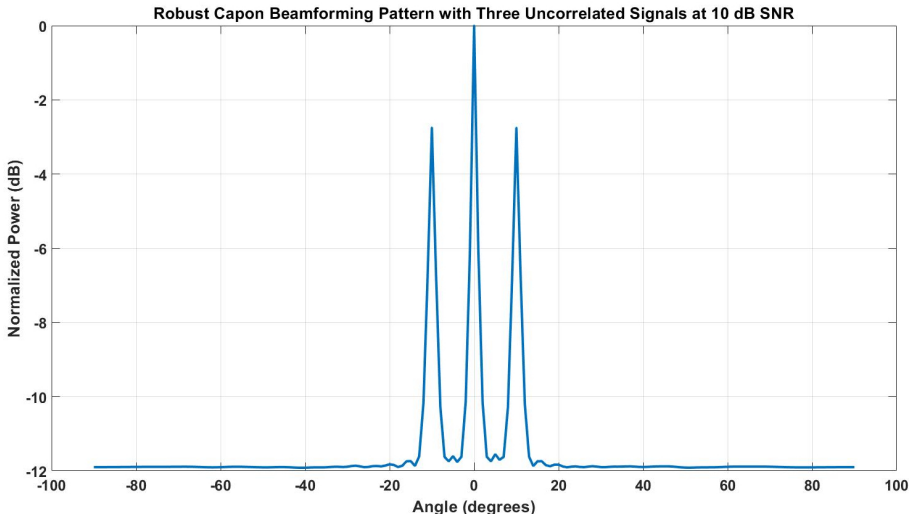


Figure 4.23 RCB Beamforming result with 10 dB SNR from $-10°$-$0°$-$10°$ angles

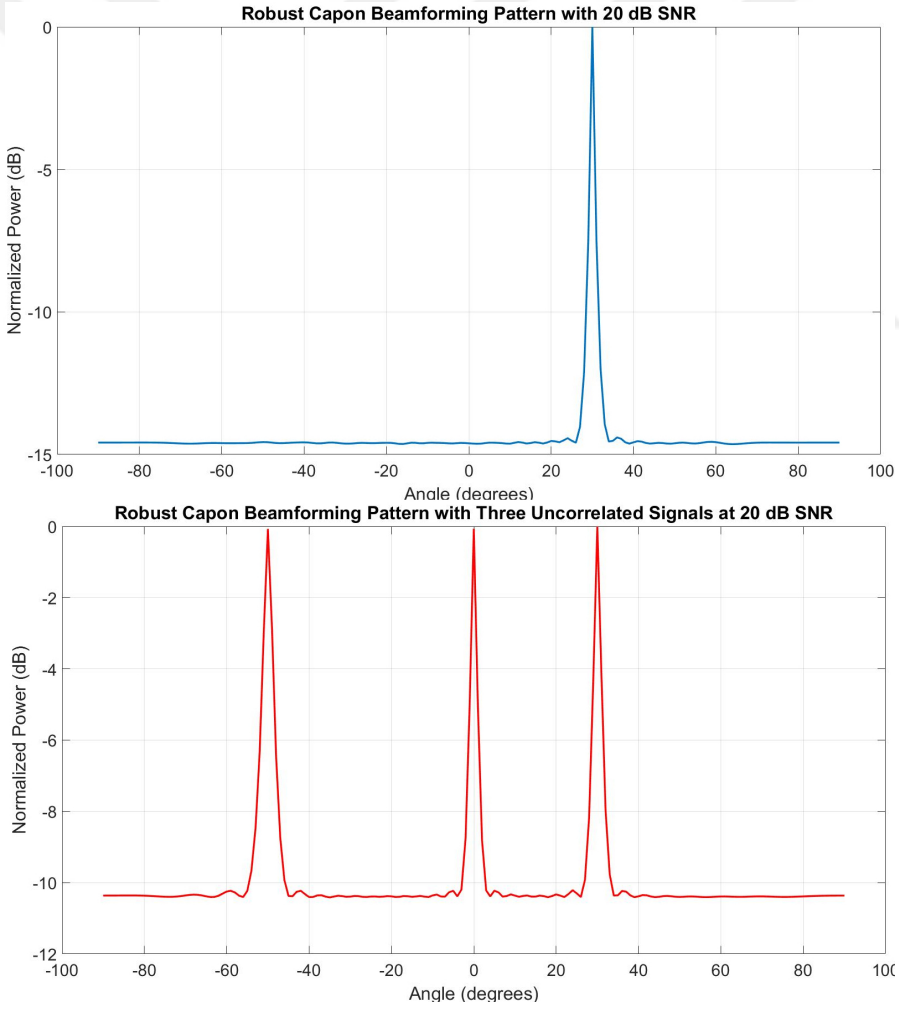


Figure 4.24 RCB beam pattern for a single source signal at $30°$ with SNR level of 20 dB (top), RCB beam patterns for three uncorrelated signals for $-50°$, $0°$, and $30°$ degree at SNR level of 20 dB, respectively (bottom)

According to the Figure 4.24, both single and uncorrelated signals can be seen in given graphs. The first beam pattern represents the $30°$ signal, and the second graph illustrates the signals coming from the direction of $-50°$, $0°$, and $30°$ degree at SNR level of 5 dB, respectively.

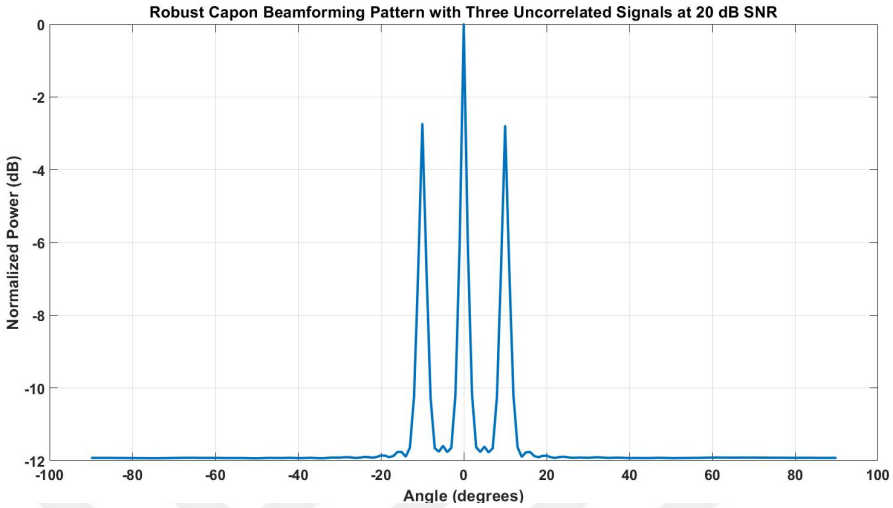


Figure 4.25 RCB Beamforming result with 20 dB SNR from $-10°$-$0°$-$10°$ angles

In Figure 4.25, the analysis focuses on the beam patterns produced by the RCB algorithm in response to uncorrelated signals originating from three distinct directions, specifically at angles of $-10°$-$0°$-$10°$. These signals, with amplitudes of 1, 2, and 1 respectively, are examined at SNR level of 20 dB.

Due to diagonal loading, regularization parameters, tolerance to steering vector errors, and interference suppression, RCB performs better compared to the SCB algorithm.

4.4 Radial Basis Function Neural Network (RBFNN)

The radial basis function network (RBFN) is a specialized type of three-layered feed-forward network architecture. This network has robustness for universal approximation and regularization capabilities. The RBFN excels in its ability to theoretically approximate any continuous function, supported by extensive research and empirical evidence.

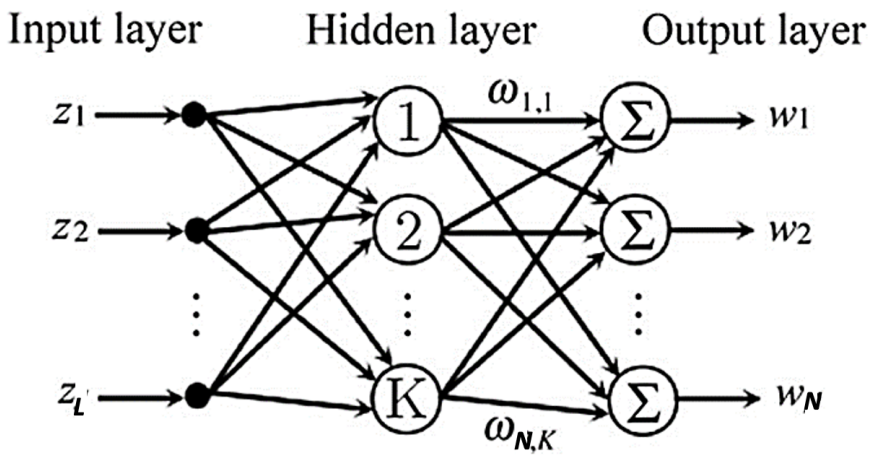


Figure 4.26 The architecture of RBFNN [56]

When the RBFNN structure has been analyzed, a three-layered architecture appears as shown in Figure 4.26. The first layer is the input layer, and the second is the hidden layer, with RBFs as neurons. Each neuron in this layer is associated with a "center" and a "spread," it typically uses a Gaussian function as an activation function. The last layer of the architecture is the output, which consists of the computed weight sum of these RBFs.

Approximation capability is an important advantage for radial basis neural networks. Hence, the network generates a strong response when the input is close to the center of the RBF in the input domain. This feature makes RBFNs suitable for localized data pattern tasks.

Due to the localized nature of RBFNs, which reduces the dimensionality of the optimization problem during the training process, RBFNs can achieve a smaller number of iterations compared with approximation methods like Multilayer Perceptions (MLPs) with backpropagation learning rules (BP). Additionally, due to the efficiency in complex pattern recognition tasks and fast training capability, implementing RBFN to Direction-of-Arrival applications like weather radar estimation problems has gained significant importance. In literature, RBFNN based on the direction of arrival applications have been investigated extensively [56–58].

In this thesis, the methodology of RBFN's is applied to the harmonic synthetic aperture radar imaging problem. The RBFN network is used for beamforming weight calculation for near-field measurement studies. Due to the network's fast adaptation to changing input patterns, the network can dynamically adjust beamforming weights, enabling a more precise and efficient imaging process.

4.4.1 RBFNN Based 1-D Beamforming Pattern Simulations and Results

In the following simulations, 1-D beampatterns generated by the RBFNN have been simulated for single-directional and uncorrelated signals from 3 different directions. In this section, only 1-D beamformer results have been presented. The RBFNN of 1-D beamformer trained with far-field signals arriving at the ULA. The RBFNN structure is trained for the ULA system covering a 180-degree angle of view, with the presence of a signal from a total of 181 far-field angles in steps of 1^0 degree each from -90^0 to 90^0. Each training sample is constructed considering a single angle of arrival to ensure the RBFNN learns to determine the direction of incoming signals accurately. Herein, the calculations are similar with [59].

The problem can be formulated as follows: first, the M antenna has been placed along the x-axis and separated by half wavelength, d, as shown in Figure 4.27. The number of arriving signals is equal to K, and the antennas are assumed to be omnidirectional. The angle of arrival is represented by θ. The AOA signals are assumed to be in the far-field region. Thus, the AOA signals are assumed to be plane waves.

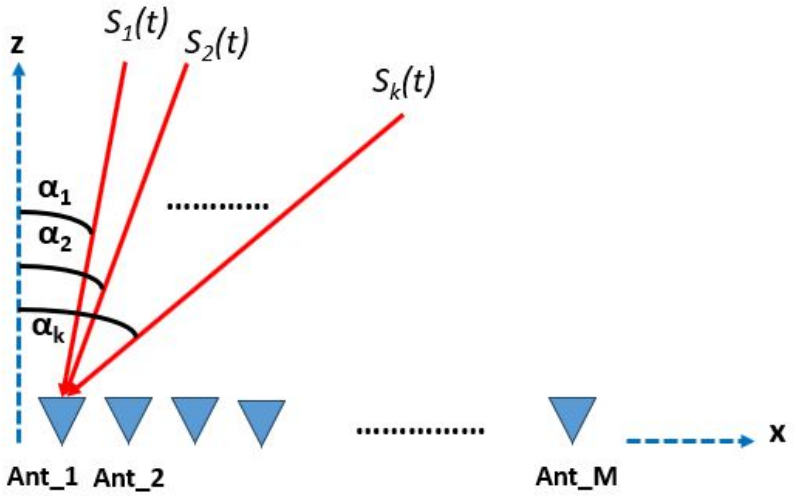


Figure 4.27 The one-dimensional uniform linear array structure

Here, this equation represents the received signal $X_i(t)$ at the $i-th$ sensor, which is composed of a summation of K signals $S_m(t)$, each with a phase shift due to the path difference d_{ik}, and an additive noise term $n_i(t)$. The signal received on each antenna element can be written as ;

$$X_i(t) = \sum_{k=1}^{K} S_m(t) e^{-j(i-1)k_m} + n_i(t) \quad i = 1, 2, \ldots, M \tag{4.23}$$

where $n_i(t)$ is the noise signal. $k_m = \frac{\omega_0 d}{c}\sin(\theta_m)$ where, d is the spacing between the antenna element, c is the speed of light in free-space, and ω_0 is the angular center frequency of the signal.

Given in matrix form,

$$X(t) = AS(t) + N(t) \tag{4.24}$$

where

$$X(t) = [X_1(t), X_2(t), \ldots, X_M(t)]^T, \tag{4.25}$$

$$N(t) = [n_1(t), n_2(t), \ldots, n_M(t)]^T, \tag{4.26}$$

$$S(t) = [S_1(t), S_2(t), \ldots, S_K(t)]^T, \tag{4.27}$$

and each entry of A can be defined as;

$$A_{im} = e^{-j(2\pi/\lambda)d_{ikm}}, \tag{4.28}$$

The spatial correlation matrix R of the received signal is given by

$$R = E\{X(t)X(t)^H\} = AE\{S(t)S(t)^H\}A^H + E\{N(t)N(t)^H\} \tag{4.29}$$

here "H" denotes the conjugate transpose.

It is depicted in (5.15), only the upper or lower triangular side of the correlation matrix is enough for the calculation. As given in (5.17), the input matrix for the RBFNN structure is formed by calculating the vector $\hat{\boldsymbol{\kappa}}$.

In DOA simulations as shown in Figure 4.28, the single source signal impinging from a 30° angle, while the uncorrelated 3 signals come from -50°, 0°, and 30°, respectively. The array sensor number is 31. The SNR is set to 0-5-10-20 dB respectively. The distance between the adjacent sensor elements equals half the wavelength of the narrowband signal.

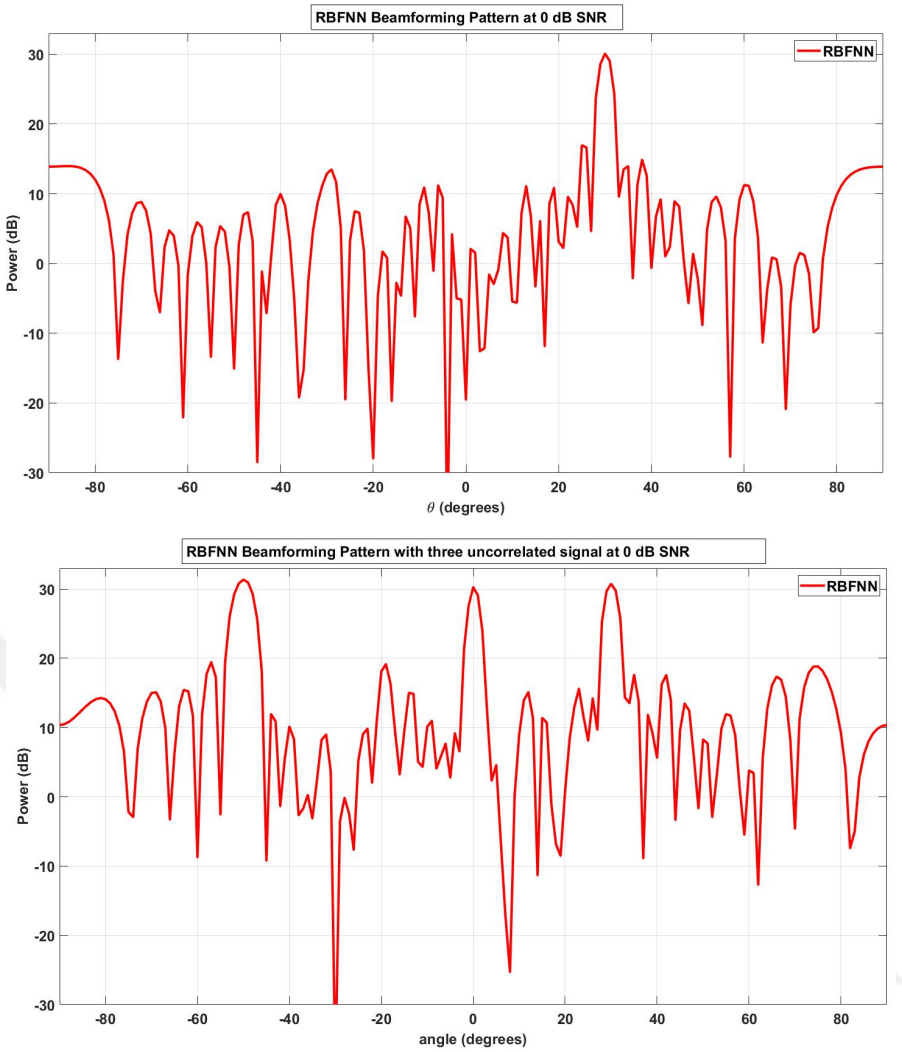


Figure 4.28 RBFNN beam pattern for a single source signal at 30° with SNR level of 0 dB (top), RBFNN beam patterns for three uncorrelated signals for -50°, 0°, and 30° degree at SNR level of 0 dB, respectively (bottom)

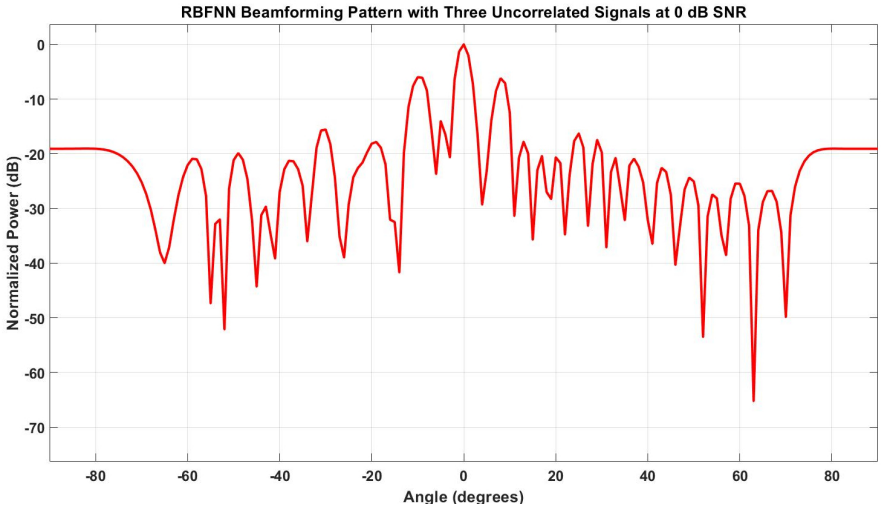


Figure 4.29 RBFNN Beamforming result with 0 dB SNR from -10°-0°-10° angles

In Figure 4.29, the analysis focuses on the beam patterns produced by the RBFNN algorithm in response to uncorrelated signals originating from three distinct directions, specifically at angles of $-10°$-$0°$-$10°$. These signals, with amplitudes of1, 2, and 1 respectively, are examined at SNR level of 0 dB.

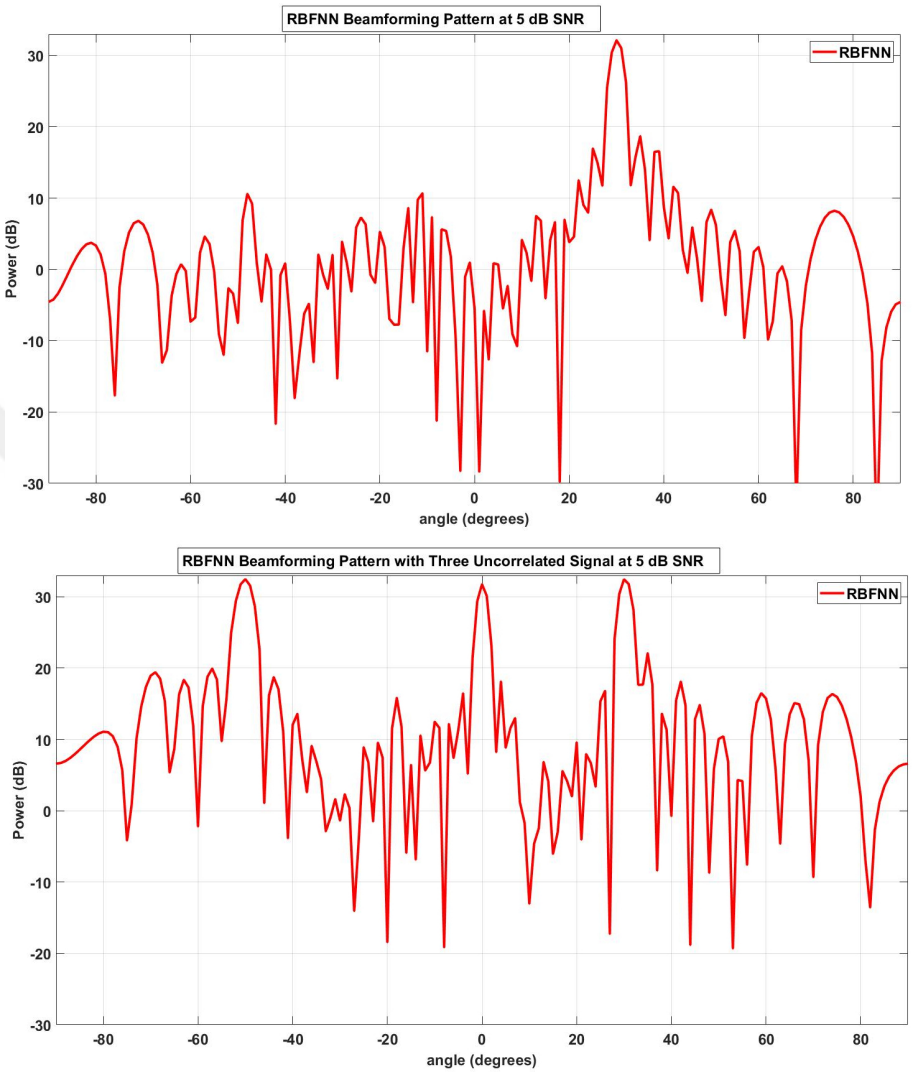


Figure 4.30 RBFNN beam pattern for a single source signal at $30°$ with SNR level of 5 dB (top), RBFNN beam patterns for three uncorrelated signals for $-50°$, $0°$, and $30°$ degree at SNR level of 5 dB, respectively (bottom)

As depicted in Figure 4.30, a singular signal approaches from $30°$ degree, while three distinct uncorrelated signals are detected coming from angles $-50°$, $0°$, and $30°$ degrees.

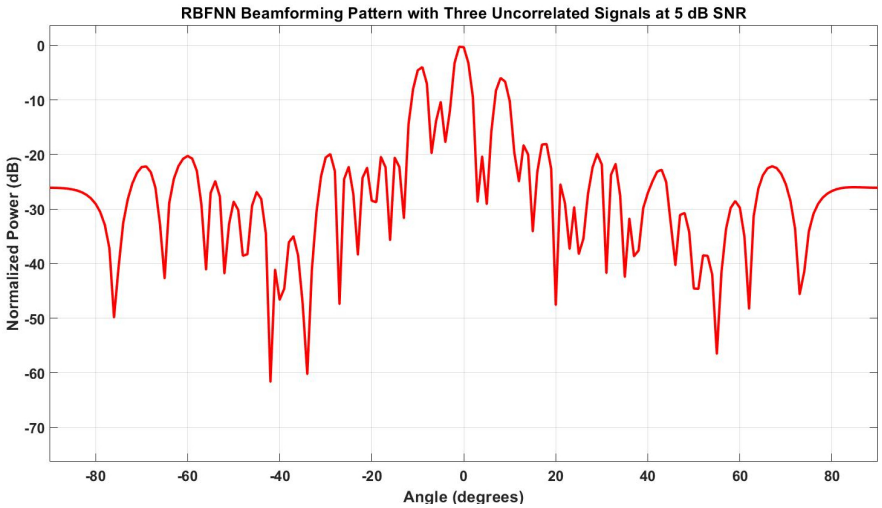


Figure 4.31 RBFNN Beamforming result with 5 dB SNR from $-10°$-$0°$-$10°$ angles

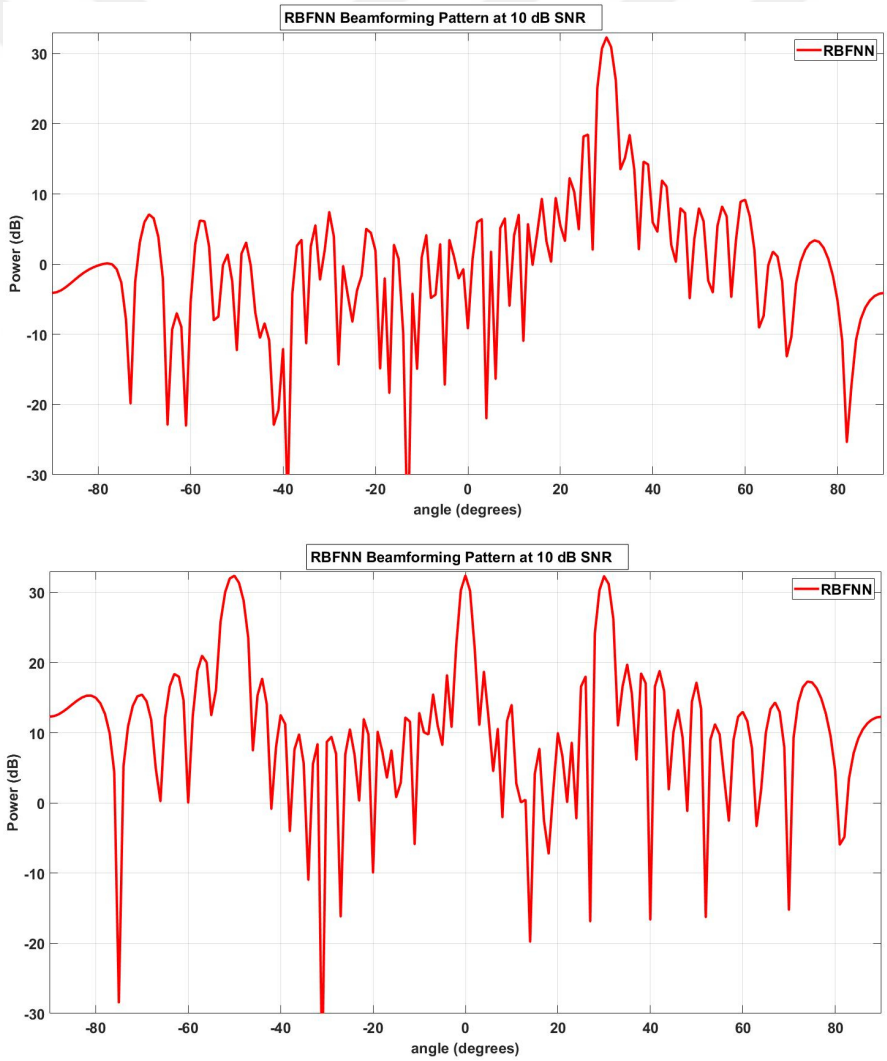


Figure 4.32 RBFNN beam pattern for a single source signal at $30°$ with SNR level of 10 dB (top), RBFNN beam patterns for three uncorrelated signals for $-50°$, $0°$, and $30°$ degree at SNR level of 10 dB, respectively (bottom)

In Figure 4.31, the analysis focuses on the beam patterns produced by the RBFNN algorithm in response to uncorrelated signals originating from three distinct directions, specifically at angles of $-10°$-$0°$-$10°$. These signals, with amplitudes of1, 2, and 1 respectively, are examined at SNR level of 5 dB.

In the DOA simulations shown in Figure 4.32, one signal is detected impinging at a $30°$ degree contrasted by three uncorrelated signals originating from $-50°$, $0°$, and $30°$ degrees.

In Figure 4.33, the analysis below focuses on the beam patterns produced by the RBFNN algorithm in response to uncorrelated signals originating from three distinct directions, specifically at angles of $-10°$-$0°$-$10°$. These signals, with amplitudes of1, 2, and 1 respectively, are examined at SNR level of 10 dB.

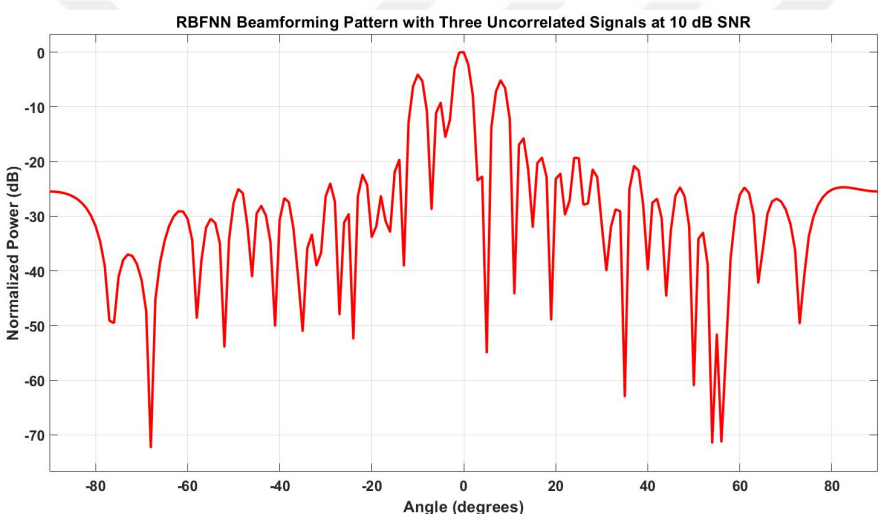


Figure 4.33 RBFNN Beamforming result with 10 dB SNR from $-10°$-$0°$-$10°$ angles

Figure 4.34 displays DOA simulations where a single source signal arrives from a $30°$ degree, while three separate signals are received from angles of $-50°$, $0°$, and $30°$ degrees.

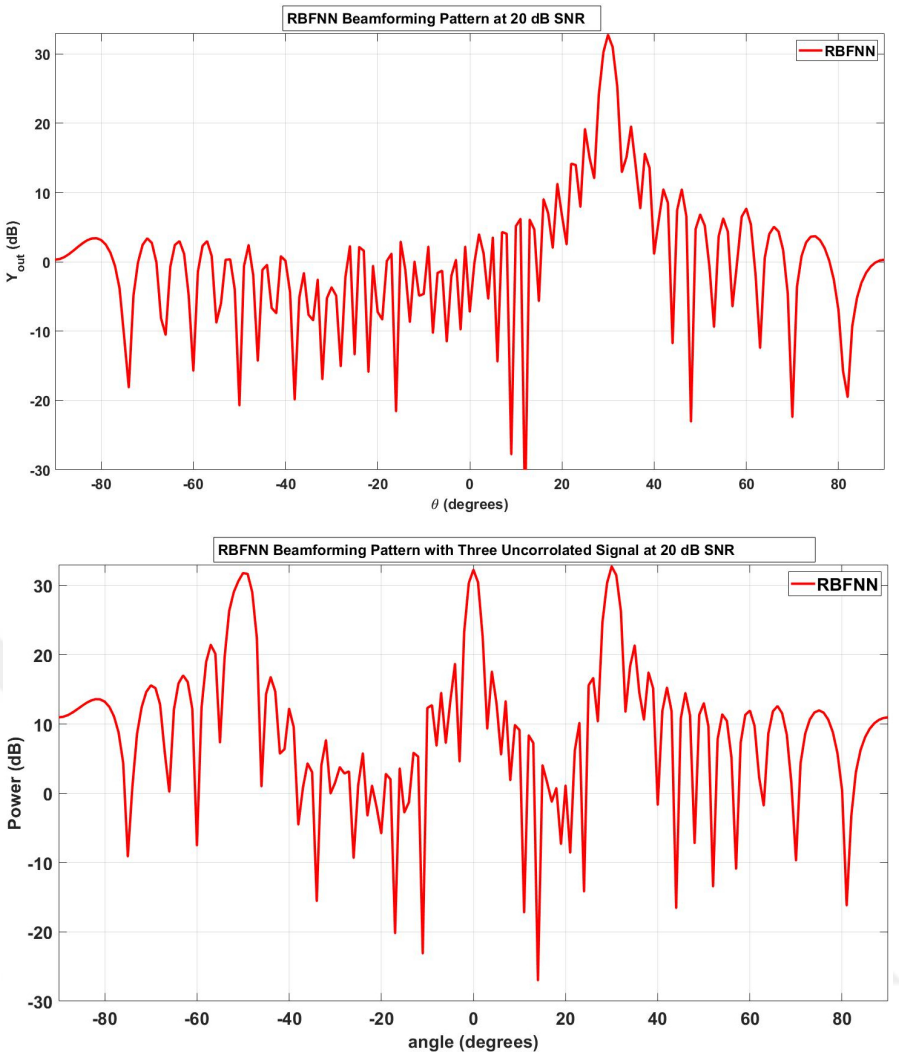


Figure 4.34 RBFNN beam pattern for a single source signal at $30°$ with SNR Level of 10 dB (top), RBFNN beam patterns for three uncorrelated signals for$-50°$, $0°$, and $30°$ degree at SNR level of 20 dB, respectively (bottom)

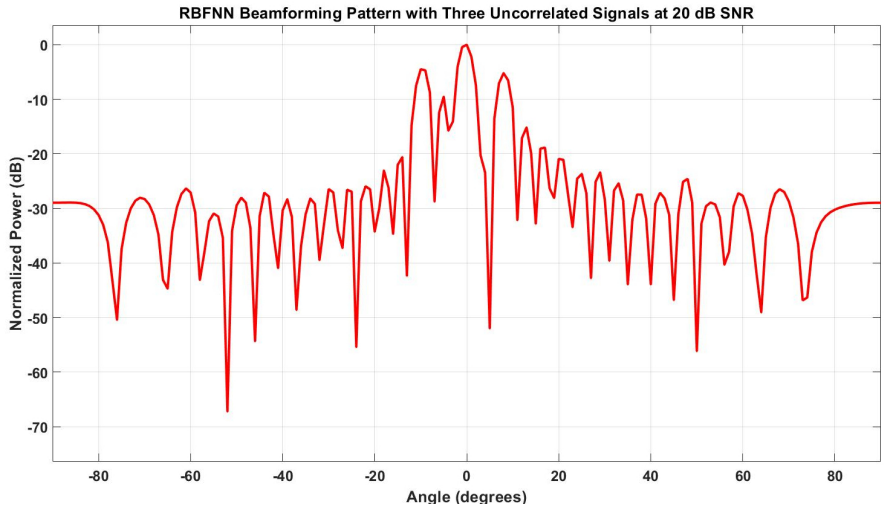


Figure 4.35 RBFNN Beamforming result with 20 dB SNR from $-10°$-$0°$-$10°$ angles

In Figure 4.35, the analysis below focuses on the beam patterns produced by the RBFNN algorithm in response to uncorrelated signals originating from three distinct directions, specifically at angles of $-10°$-$0°$-$10°$. These signals, with amplitudes of1, 2, and 1 respectively, are examined at SNR level of 20 dB.

According to the 1-D beamforming results using the RBFNN beamformer, even if the SNR level is as low as 0 dB, the RBFNN beamformer can calculate the weights of the ULA for a given signal direction.

4.5 Discussion

The findings reveal that the DSB beamformer structure successfully detects and orients to unidirectional signals and signals that are close to each other, while it shows lower performance for signals coming from wider angles. Additionally, it lags in accurately detecting signal amplitudes, especially when compared to alternative beamforming approaches. Conversely, upon examining the Standard Capon Beamformer (SCB) and Robust Covariance Beamformer (RCB) algorithms, it can be concluded that both beamformer structures outperform the DSB across various simulation conditions. These algorithms demonstrated greater accuracy and consistency, adeptly handling signals that have been closely spaced and differing amplitudes. Additionally, the RCB-based beamformer has outperformed SCB due to its sidelobe suppression ability. In addition, a radial neural network-based 1-D beamformer has been developed and compared with its conventional counterparts under the exact scenarios. The simulation results show that it has demonstrated its robust ability to accurately discriminate the direction of incoming signals under all tested scenarios while maintaining high performance for signals of proximity and varying amplitude. When the RBFNN-based beamformer structure is examined, it is seen that it is able to successfully separate signals from both single and three different directions at all SNR levels and form beampatterns. Furthermore, when the beampattern results with three different signals of different amplitudes and closer angles are analyzed, it is seen that the amplitude and angular accuracy are maintained at all SNR levels.

5
EXPERIMENTAL RESULTS AND DISCUSSION

This section comprehensively investigates the harmonic radar systems' experimental results of the image formation algorithms. The measurement setup has been constructed in the TÜBİTAK BİLGEM Antenna Technologies and Measurement System (ATAM) laboratory to carry out experimental studies and demonstrate the effectiveness of the prototype of the HBF system. The usable scanning area equals 1.5x2x2 meters. Here, the measurement scene contains a passive Recco RF tag (NLS-1), a bow-tie antenna containing a Schottky diode (NLS-2), a Macom SFD26 connectorized doubler (NLS-3), a 2-meter-long 6 cm radius aluminum pipe (RCS-1), and an aluminum pyramidal structure (RCS-2). The fundamental frequency employed in these experimental studies is $f_0 = 2.4$ GHz, and only the second harmonic of the fundamental frequency, namely $2f_0 = 4.8$ GHz, has been considered in all measurement scenarios. The targets have been placed on styrofoam and ABS material. The Delay and Sum (DSB), Capon (SCB), Robust Capon (RCB), and RBFNN neural network-based beamformer methods have been employed to create a 2-D image of NLS in measurement scenarios. Eight different measurement scenarios have been completed here, and the results are discussed in section 5.2. Additionally, the computer hardware used during the 2-D image acquisition studies carried out in this thesis can be summarised as follows: Intel Xeon CPU E5-2680 2.8GHz CPU, 512 GB DDR4 RAM, NVIDIA Tesla K80 GPU. All image formation and data processing studies have been obtained using *Matlab* environment.

5.1 HBF Image Construction

The HBF images can be formed in many different ways. Herein, a sliding computer-controlled motorized system has been employed. The receive antenna collects 31 data from distinct positions. First, in order to perform image formation algorithms, the scanning area, coordinate system, and antenna positions must be defined. The 2-D images' mathematical calculations are established, and these

calculations parallel the study of [16]. The scanning area consists of P pixels with coordinates $(x_p(i), y_p(i), z_p(i))$ and amplitude $P(i)$, where $1 \leq i \leq P$. Data is collected over an aperture consisting of M positions, which is 31 positions in these experiments. In this thesis, the TX antenna position is static. Thus, the coordinate of the transmit antenna is known, and receive antennas need to be known at each of the M positions on the x-axis. The location of the receive antenna at each aperture position is defined to be $(x_R(m), y_R(m), z_R(m))$ where $1 \leq m \leq M$.

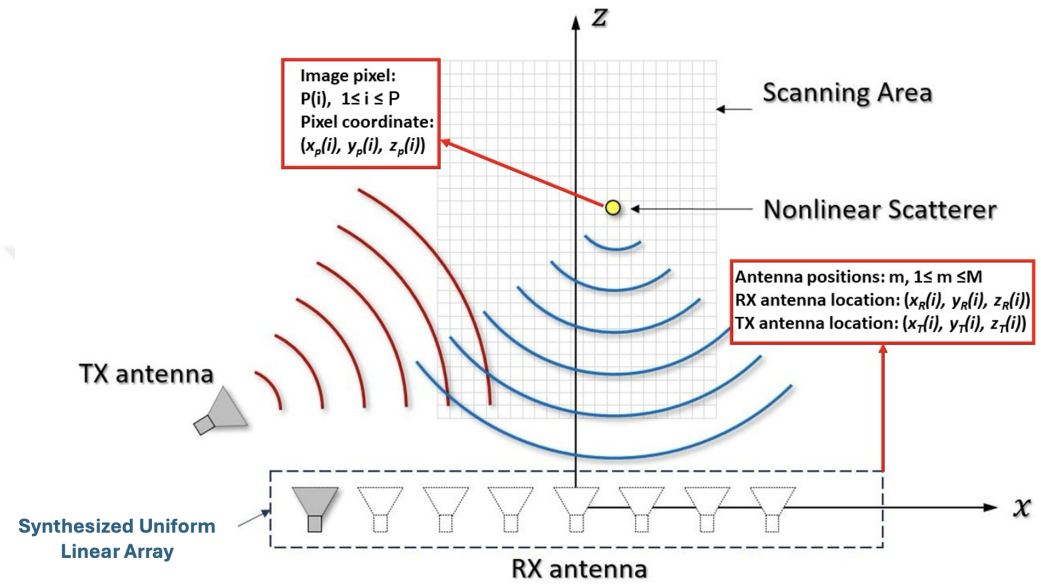


Figure 5.1 Imaging of nonlinear scatterer with synthesized uniform linear array

The harmonic generating target is exited by a single transmitter operating at frequency ω. The exiting fields impress the current densities $\boldsymbol{j}_{\omega}$,$\boldsymbol{j}_{2\omega}$,$\boldsymbol{j}_{3\omega}$, where the subscript $n\omega$, $n \in \mathbb{Z}$, denotes the n'th harmonic. Because of the use of a single transmitter, the actual relation between the impressed current densities and the exiting field is not relevant to our task of imaging. Secondary fields named here as *scattered harmonics,* $\boldsymbol{E}_{n\omega}$, are exited by the current densities $\boldsymbol{j}_{n\omega}$. These scattered harmonics are observed by a Uniform Linear Array (ULA) to form construct an image of the current distribution in a region of space. In theory, an image can be constructed for each $\boldsymbol{j}_{n\omega}$by observing the corresponding scattered harmonic $\boldsymbol{E}_{n\omega}$. In practice, however, harmonics for $n > 2$ are too weak to allow imaging unless imaging is done in the close vicinity of the target. In Figure 5.1, the imaging geometry is depicted. The ULA, having M identical antenna elements, is aligned with the $x-$axis with the antenna boresights pointing in the $z-$direction. The spacing between the antenna elements of the ULA is $d = \lambda/2n$, where $\lambda = 2\pi c/\omega$ (c: speed of light in vacuum) is the wavelength corresponding to the *fundamental harmonic* ω. By reciprocity, the output of the m'th receiving antenna element of the

ULA is given by;

$$\int_{\mathcal{D}} \boldsymbol{j}_{n\omega}(\boldsymbol{r}) \cdot \boldsymbol{E}^{(a)}_{n\omega}(\boldsymbol{r}, m)\, d\boldsymbol{r} = \int_{\mathcal{D}} \boldsymbol{E}_{n\omega}(\boldsymbol{r}) \cdot \boldsymbol{j}^{(a)}_{n\omega}(\boldsymbol{r}, m)\, d\boldsymbol{r} \tag{5.1}$$

The integral on the right hand side is propotional to the voltage output of the m'th receiver antenna

$$v^{(m)}_{n\omega} = \int_{\mathcal{D}} \boldsymbol{E}_{n\omega}(\boldsymbol{r}) \cdot \boldsymbol{j}^{(a)}_{n\omega}(\boldsymbol{r}, m)\, d\boldsymbol{r} \tag{5.2}$$

where without loss of generality, we have absorbed the proportionality constant is expressed into in the output voltage. In this study, the target is assumed to be in the far-field of the receiver antennas so that we can use the approximation

$$\boldsymbol{E}^{(a)}_{n\omega}(\boldsymbol{r}, m) \approx \boldsymbol{f}_{n\omega}(\theta_m, \phi_m) \frac{e^{ink_o|\boldsymbol{r}-\boldsymbol{r}_m|}}{|\boldsymbol{r}-\boldsymbol{r}_m|} \tag{5.3}$$

where $|\boldsymbol{r}-\boldsymbol{r}_m| = \sqrt{(x-md)^2+y^2+z^2}$, (x, y, z) are the Cartesian coordinates of the target, (θ_m, ϕ_m) are the spherical angles of the target from the m'th receiver antenna and is $\boldsymbol{f}_{n\omega}$ the far-field vector pattern of the receiver antennas at frequency $n\omega$. The final expression for the m'th receiver antenna output with measurement noise $u^{(m)}_{n\omega}$ is then given as

$$v^{(m)}_{n\omega} = \frac{e^{ink_o|\boldsymbol{r}-\boldsymbol{r}_m|}}{|\boldsymbol{r}-\boldsymbol{r}_m|} \boldsymbol{I}_{n\omega} \cdot \boldsymbol{f}^{(m)}_{n\omega} + u^{(m)}_{n\omega} \tag{5.4}$$

where $\boldsymbol{f}^{(m)}_{n\omega} = \boldsymbol{f}_{n\omega}(\theta_m, \phi_m)$, and for a well localized source with a dominant polarization$\boldsymbol{I}_{n\omega} \approx \int_{\mathcal{D}} \boldsymbol{j}_{n\omega}(\boldsymbol{r})\, d\boldsymbol{r}$. For simplicity, we will assume that the current is aligned with the $y-$axis so that $\boldsymbol{I}_{n\omega} = s_{n\omega}\widehat{\boldsymbol{y}}$. Thus,

$$v^{(m)}_{n\omega} = \frac{e^{ink_o|\boldsymbol{r}-\boldsymbol{r}_m|}}{|\boldsymbol{r}-\boldsymbol{r}_m|} \widehat{\boldsymbol{y}} \cdot \boldsymbol{f}^{(m)}_{n\omega} s_{n\omega} + u^{(m)}_{n\omega} \tag{5.5}$$

In the remainder, we will drop the subscript $n\omega$ for clarity and writing the above in a compact form for all receiver outputs leads to

$$\tilde{v} = \tilde{a}s + \tilde{u} \tag{5.6}$$

where $s = s_{n\omega}$, $\tilde{v} = \left[v_{n\omega}^{(1)}, v_{n\omega}^{(2)}, \ldots, v_{n\omega}^{(M)}\right]^T$, $\tilde{u} = \left[u_{n\omega}^{(1)}, u_{n\omega}^{(2)}, \ldots, u_{n\omega}^{(M)}\right]^T$ with superscript T denoting transpose and

$$\tilde{a} = \left[\frac{e^{ink_o|\boldsymbol{r}-\boldsymbol{r}_1|}}{|\boldsymbol{r}-\boldsymbol{r}_1|}\widehat{\boldsymbol{y}}\cdot\boldsymbol{f}_{n\omega}^{(1)},\ \frac{e^{ink_o|\boldsymbol{r}-\boldsymbol{r}_2|}}{|\boldsymbol{r}-\boldsymbol{r}_2|}\widehat{\boldsymbol{y}}\cdot\boldsymbol{f}_{n\omega}^{(2)},\ \ldots\ ,\ \frac{e^{ink_o|\boldsymbol{r}-\boldsymbol{r}_M|}}{|\boldsymbol{r}-\boldsymbol{r}_M|}\widehat{\boldsymbol{y}}\cdot\boldsymbol{f}_{n\omega}^{(M)}\right]^T \tag{5.7}$$

Image corresponding to the n'th harmonic is constructed using the Delay and Sum Beamformer (DSB), the Standard Capon Beamformer (SCB) (a.k.a. the Minimum Variance Distortionless Response (MVDR)) and the Robust Capon Beamformer (RCB). The latter two beamformers are super-resolution techniques. The image is composed of a gridded rectangular box in the $XZ-$plane as shown Figure 5.1. Grid points corresponding to pixels are defined by the coordinates $(k\delta x, l\delta z)$, $k \in 1, \ldots, P_x$, $l \in 1, \ldots, P_z$, where δx and δz are the pixel dimensions along the $x-$ and $z-$axis. Here, the DSB weights $\mathbf{w}_{dsb}$, are given by

$$\mathbf{w}_{dsb}(k,l) = [\mathbf{D}(k,l)]^{-1}\ \mathbf{s}(k,l) \tag{5.8}$$

where $\mathbf{s}(k,l) = \left[e^{ink_o\Delta r_{kl,1}}, e^{ink_o\Delta r_{kl,2}}, \ldots, e^{ink_o\Delta r_{kl,M}}\right]^T$ is the *steering vector* with $\Delta r_{kl,m} = \|\boldsymbol{r}_{kl} - \boldsymbol{r}_m\| = \sqrt{(k\delta x - md)^2 + (l\delta z)^2}$ and the diagonal matrix $\mathbf{D}$ given as

$$\mathbf{D}(k,l) = \begin{bmatrix} \boldsymbol{\ell}_n\cdot\boldsymbol{f}_n(1)/\Delta r_{kl,1} & & \cdots & 0 \\ & \boldsymbol{\ell}_n\cdot\boldsymbol{f}_n(2)/\Delta r_{kl,2} & & \vdots \\ \vdots & & \ddots & \\ 0 & \cdots & & \boldsymbol{\ell}_n\cdot\boldsymbol{f}_n(M)/\Delta r_{kl,M} \end{bmatrix}$$

It should be noted that, in principle, there is an image I_{dsb} for each harmonic. The SCB and RCB images are formed by

$$I_{scb}(k,l) = \mathbf{w}_{scb}^H(k,l)\,\mathbf{R}\,\mathbf{w}_{scb}(k,l) \tag{5.9}$$

$$I_{rcb}(k,l) = \mathbf{w}_{rcb}^H(k,l)\,\mathbf{R}\,\mathbf{w}_{rcb}(k,l) \tag{5.10}$$

where $\mathbf{R} = \left\langle \mathbf{v}\mathbf{v}^H \right\rangle$ is the covariance matrix ($\langle\cdot\rangle$ stands for ensemble average) of the ULA output voltages. The covariance matrix is approximated by the the sample covariance matrix. The SCB weight vector is the solution to the linearly constrained quadratic optimization problem

$$\min_{\mathbf{w}_{scb}} \mathbf{w}_{scb}^H(k,l)\,\mathbf{R}\,\mathbf{w}_{scb}(k,l) \qquad \text{subject to} \quad \mathbf{w}_{scb}^H(k,l)\,\mathbf{s}_f(k,l) = 1$$

This SCB optimization problem aims to select the weights so as to minimize interference in beamformer output when focused to a specific grid point by the *focusing vector* $\mathbf{s}_f(k,l) = \mathbf{D}(k,l)\,\mathbf{s}(k,l)$. The weight vector is given by

$$\mathbf{w}_{scb}(k,l) = \frac{\mathbf{R}^{-1}\,\mathbf{s}_f(k,l)}{\mathbf{s}_f^H(k,l)\,\mathbf{R}^{-1}\,\mathbf{s}_f(k,l)} \tag{5.11}$$

SCB yields good results when the focusing vector $\mathbf{s}_f$, is known but results deteriorate with uncertainty in $\mathbf{s}_f$. RCB, as the name suggests, is designed to work under uncertainty in $\mathbf{s}_f$. The RCB weight vector is the solution to the spherically constrained quadratic optimization problem

$$\min_{\mathbf{w}_{rcb}} \mathbf{w}_{rcb}^H(k,l)\,\mathbf{R}\,\mathbf{w}_{rcb}(k,l) \qquad \text{subject to} \quad \|\mathbf{w}_{rcb}^H(k,l) - \mathbf{s}_f(k,l)\|^2 \leq \epsilon$$

where ϵ is the uncertainty in $\mathbf{s}_f(k,l)$. The RCB weight vector is given by

$$\mathbf{w}_{rcb}(k,l) = \frac{\mathbf{R}^{-1}\,\hat{\mathbf{s}}_f(k,l)}{\hat{\mathbf{s}}_f^H(k,l)\,\mathbf{R}^{-1}\,\hat{\mathbf{s}}_f(k,l)} \tag{5.12}$$

where the modified focusing vector $\hat{\mathbf{s}}_f = \mathbf{s}_f - (\mathbf{I} + \lambda\mathbf{R})^{-1}\mathbf{s}_f$ and the Lagrange multiplier λ, is the unique solution to the constraint equation $|(\mathbf{I} + \lambda\mathbf{R})^{-1}\mathbf{s}_f|^2 = \epsilon$.

5.2 Experimental Analysis of Microwave Imaging for Nonlinear Scatterers Using Conventional Beamformer Techniques

In this thesis, nonlinear scatterers have been detected at standoff range in the laboratory environment. The targets used in the experimental studies are an RF Tag (NLS-1), a Schottky diode tag (NLS-2), and a doubler (NLS-3), as shown in Figure 5.2. In order to examine the response of the HBF system in the presence of a linear clutter target, a 2 m long aluminum pipe with a diameter of 6 cm

(RCS-1) and a metal cone with dimensions of 23x23x21 cm has been placed next to the nonlinear targets (RCS-2) in the measurement environment. The nonlinear elements used in this study have been placed on a 10cm stepped styrofoam foam or 10 cm high ABS material. In this section, two main points about harmonic radar are explained. Firstly, it will show that harmonic radar data can be used to generate HBF images. Secondly, it will prove experimentally that harmonic radar can suppress linear clutter when detecting nonlinear targets. Three conventional beamformer algorithms, DSB, SCB, and RCB, have been developed and employed to create an HBF image of the nonlinear scatterers. Data have been collected with targets positioned in 8 different locations on 25 pixels on the x-axis and 51 pixels on the z-axis, totaling 1275 pixels, which have been considered in order to form an NLS image in a 2-D scanning area. The transmitting and receiving antennas are separate, and the receiving antenna collects data for approximately 6 seconds before automatically moving to a new position. Each HBF measurement takes approximately 3 minutes in total.

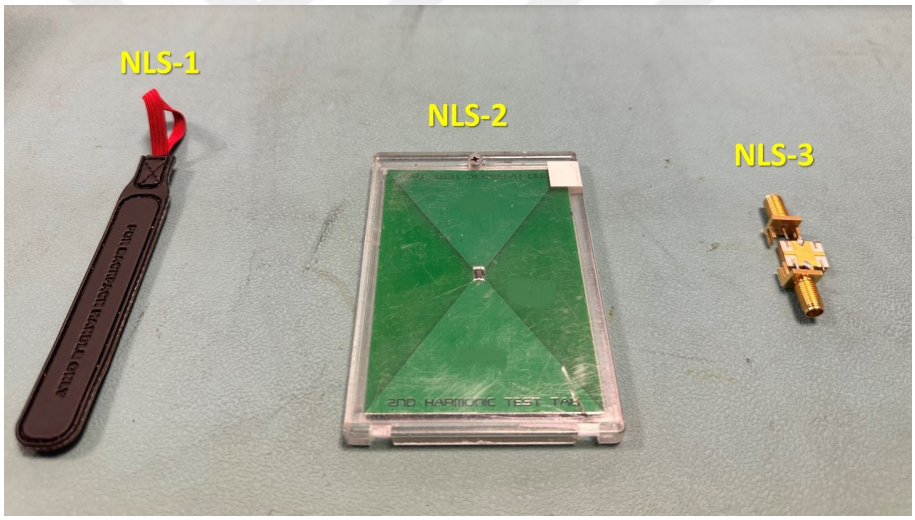


Figure 5.2 Nonlinear scatterers used in measurements

The computer-controlled motorized synthetic microwave imaging system (HBF-2) results will be presented and discussed here. The next sections illustrate the measurement results of the NLS at different beamformers, locations, and scenarios.

5.2.1 Measurement-1

The measurement-1 illustrates the HBF images in a free-space medium. The HBF data collected here uses a DSB, SCB, and RCB beamformer to create nonlinear scatterers' locations on a 2-D map. The scanning nearfield area detail can be seen in Figure 5.1.

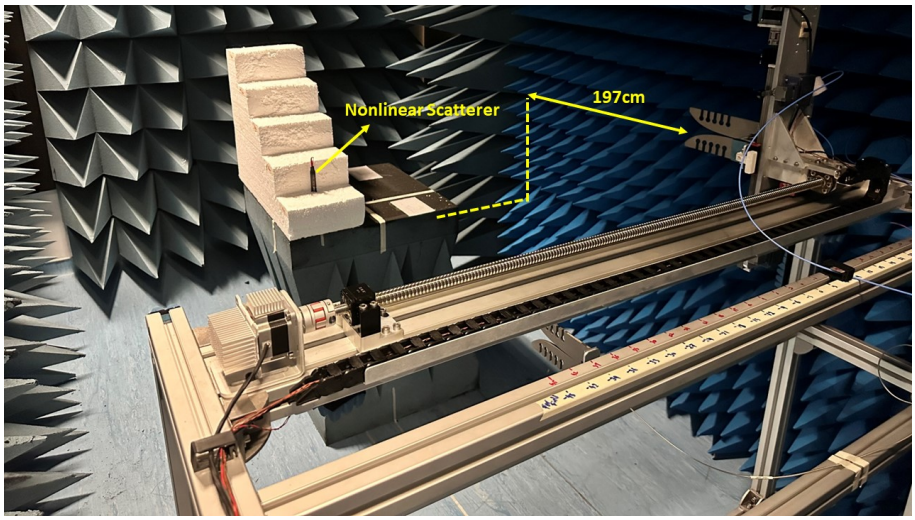


Figure 5.3 NLS-1 placement on styrofoam

Data have been collected by the HBF-2 system inside an anechoic chamber to prevent environmental effects and multipath, as shown in Figure 5.3. Herein, the receive antenna has been automatically moved along a 90cm antenna array aperture with a 3 cm step. Thus, 31 receiver antenna positions have been provided for the image formation with the HBF system. The transmitter antenna is located at the center of the HBF system. This study's HBF system is centered zero on the x-axis and spans -45 to 45 cm. The first measurement scenario contains only the NLS-1, which has been placed 197 cm on the z-axis, 0 cm (centered) on the x-axis, and 84.5 cm on the y-axis.

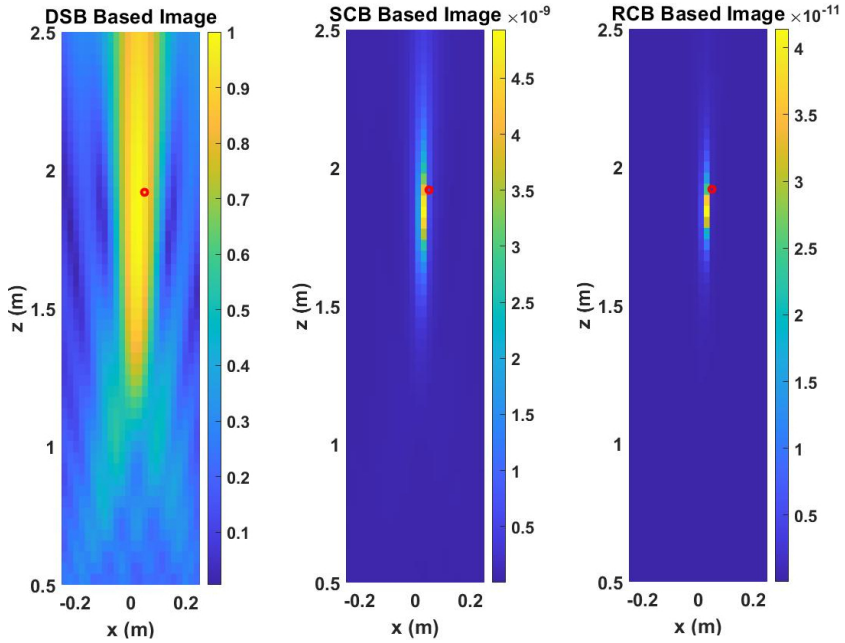


Figure 5.4 HBF results with image formation algorithm from NLS-1 at x=0cm, y=84.5cm, z=197cm

According to the image formation algorithm's results, the NLS-1 can be easily distinguished from the background, and no linear or other clutter appeared in the scene as expected. Comparing imaging algorithm results in Figure 5.4, it can be concluded that the DSB shows the poorest performance due to its limited capability of handling noise and signal interference, which leads to the DSB having the lowest resolution and localization performance and highest clouding effects. On the contrary, the SCB has improved image quality by offering better resolution and side lobe suppression, enhancing target clarity and localization. On the other hand, the Robust Capon approach showed the best image quality among the three algorithm results. RCB algorithm effectively reduces interference and noise while maintaining the integrity of the intended signal. In conclusion, the RCB algorithm is the best method in this experimental study, producing images with the best sharpness, resolution, and contrast. Although SCB and RCB provide better image quality and clarity, both shifted the NLS-1 location by 4cm on the z-axis, 193cm, and 2 cm on the x-axis.

5.2.2 Measurement-2

This section illustrates an NLS-1 with an aluminum pipe (RCS-1). The RCS-1 has the dimensions of 2 m length and diameter of 6 cm. It has been vertically aligned near the NLS-1, as seen in Figure 5.5 The NLS-1 and RCS-1 have been placed 118cm ahead of the HBF-2 system on the z-axis. The NLS-1 has been placed -17.5 cm on the x-axis and 84.5 cm on the y-axis.

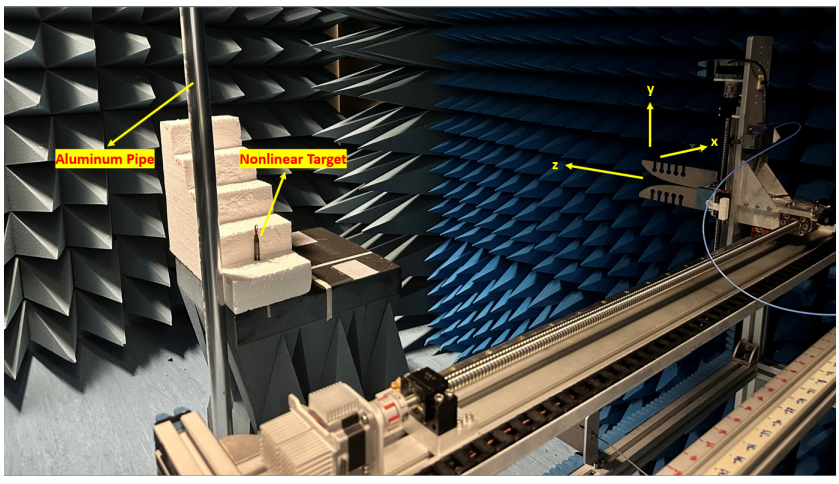


Figure 5.5 The placement of the NLS-1 and an aluminium pipe in the scanning area

In the comparative analysis of image formation algorithms, the results demonstrate a clear distinction between the performances of DSB, SCB, and RCB methods.

According to the measurement result, depicted in Figure 5.6, the NLS-1 has been successfully detected on all image formation algorithms, and no evidence of the RCS-1 has occurred, as expected. Only a negligible clouding effect has occurred on harmonic images. This phenomenon occurs because the harmonic components emanating from the tag target reflect off the aluminum pipe, thereby dispersing the focal clarity of the target.

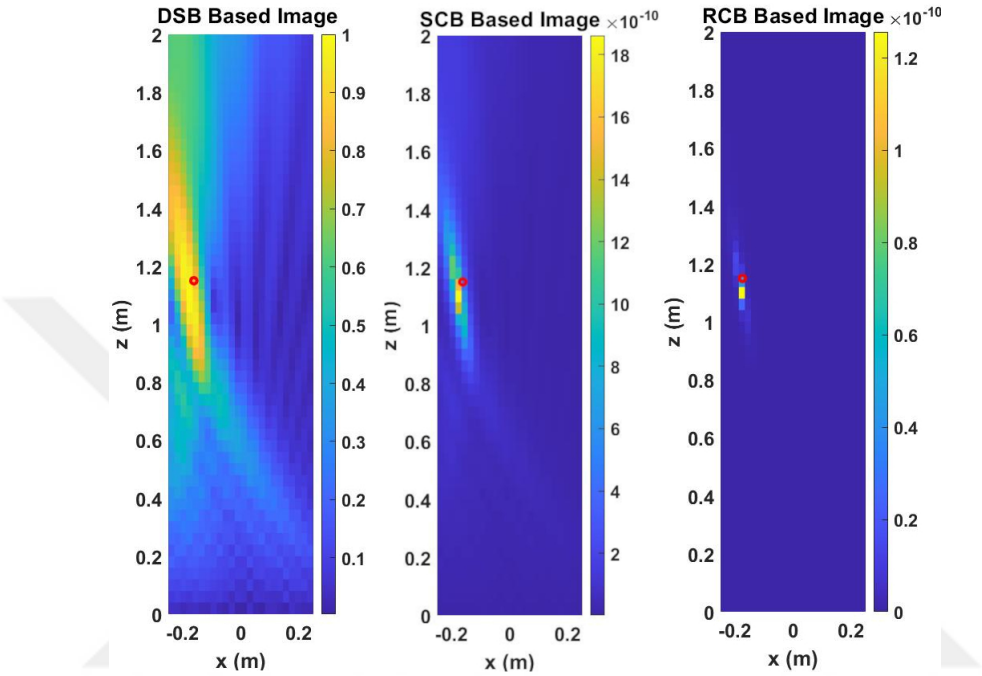


Figure 5.6 HBF results with image formation algorithm from NLS-1 at x=-17.5cm, y=84.5cm, z=118cm

The DSB exhibits the lowest resolution and localization performance in a given scenario. On the other hand, the SCB algorithm shows significantly enhanced image localization and resolution compared to DSB. However, the most notable enhancement in image quality is observed with the RCB. It shows superior resolution and contrast, which makes the RCB the most effective method in this experimental study.

5.2.3 Measurement-3

In the measurement scenario depicted in Figure 5.7, a different Radio Frequency (RF) Tag, NLS-2, is utilized. The tag comprises a Schottky diode and a bow-tie antenna. The Schottky diode has been soldered between the antenna arms. The NLS-2 has been placed 144 cm on the z-axis, 84.5 cm in height on the y-axis, and 0 cm (centered) on the x-axis.

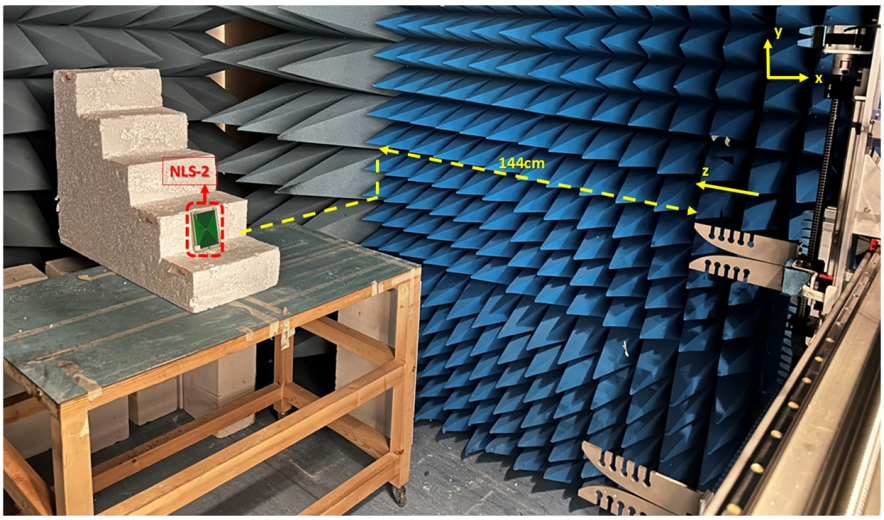


Figure 5.7 The placement of the NLS-2 in the scanning area

As illustrated in Figure 5.8, the NLS-2 has been successfully identified and localized by all three image formation algorithms. When the DSB algorithm is analyzed, it is seen that the amplitude distribution resulting from the target detection is spread over a wide range of areas. When the SCB algorithm is examined, it can be easily observed that the accuracy and resolution of the target localization have notably increased. Furthermore, the RCB algorithm further enhances the SCB algorithm by target localization and resolution. Only a negligible clutter effect is observed.

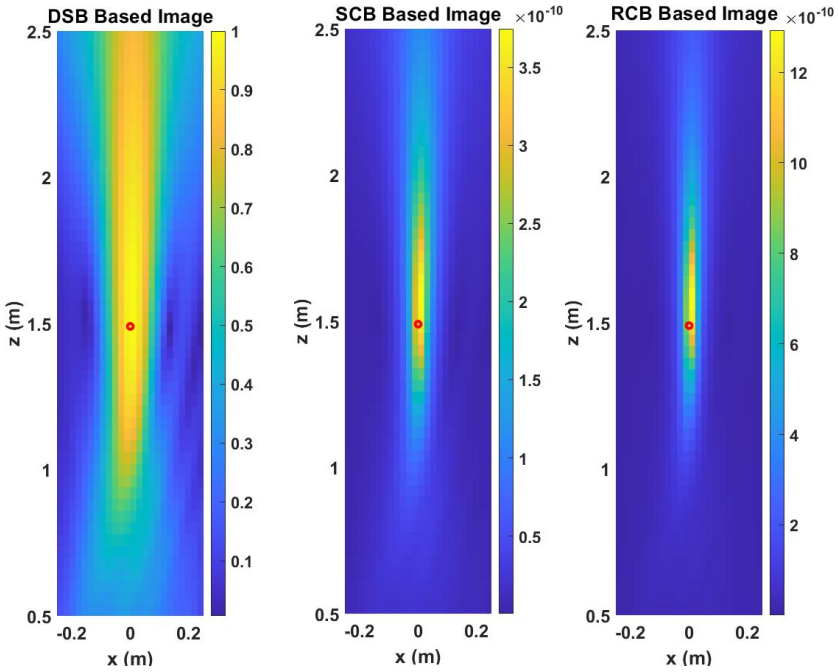


Figure 5.8 HBF results with image formation algorithm from NLS-2 at x=0cm, y=84.5cm, z=144cm

5.2.4 Measurement-4

In this measurement scenario, the NLS-1 has been placed on x=0 cm (centered) y= 84.5 cm, and z=118 cm, shown in Figure 5.9. The NLS-1 has been positioned over the ABS material, and the measurement scene contains no scatterer.

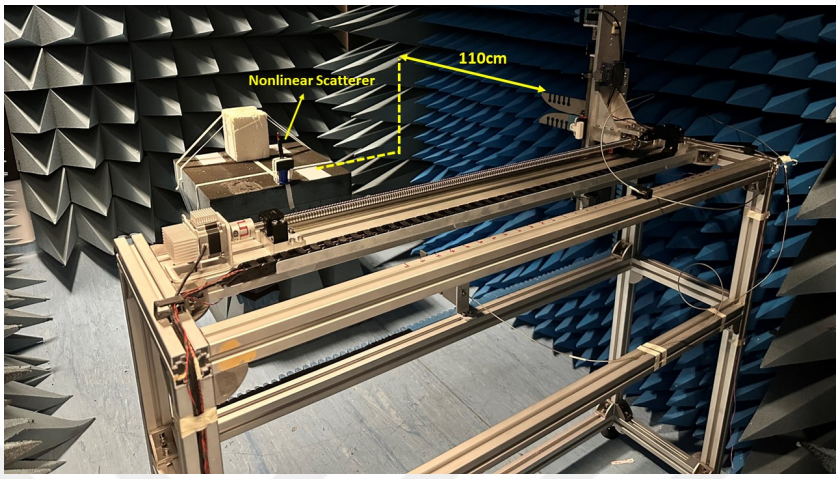


Figure 5.9 The placement of the NLS-1 in the scanning area for measurement-4

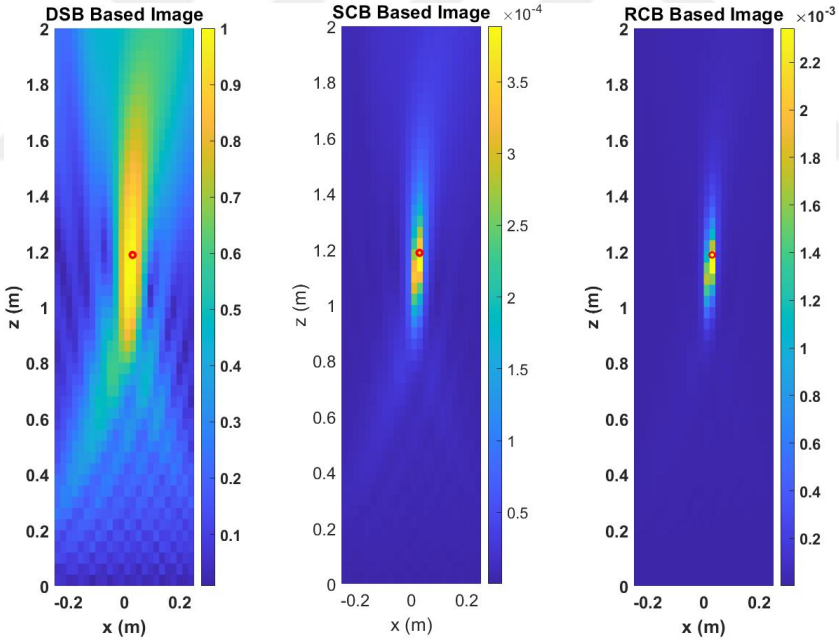


Figure 5.10 HBF results with image formation algorithm from NLS-1 at x=3cm, y=84.5cm, z=118cm

According to Figure 5.10, the NLS-1 has been successfully identified and positioned by all three image formation algorithms. Their performance varied in amplitude distribution, accuracy, and resolution. When a closer examination of the DSB algorithm is analyzed, it is stated that the amplitude distribution of the detected target spreads over a significant area and indicates a wider response; thus, a less

localized response has been provided. In contrast, the SCB beamforming technique significantly improves the accuracy and resolution of NLS-1 localization. Parallel to SCB's performance, the RCB algorithm shows excellent accuracy in accurately localizing the target and offers the benefit of little clutter-induced distortion.

5.2.5 Measurement-5

In this measurement scenario, the NLS-3 target, the minicircuit doubler, has been placed on the axis of x=-20 cm, y= 86 cm, and z= 130 cm. As shown in Figure 5.11, the NLS-3 has been placed over a wooden table with an ABS material.

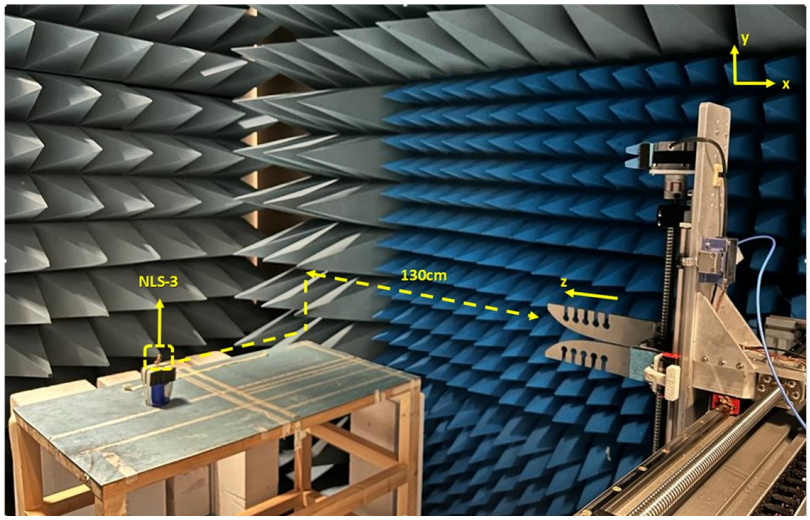


Figure 5.11 The placement of the NLS-1 in the scanning area for measurement-5

The images obtained from the measurement are shown in Figure 5.12. According to the image formation algorithm results, the DSB images show noticeable defocusing, ambiguities, and artifacts within the image. On the other hand, the results of the SCB algorithm show significant enhancements in resolution, focusing, and target localization. The RCB algorithm further elevates these aspects with better resolution and localization than the two image formation algorithms mentioned above. The SCB and RCB have been able to localize the target with a deviation of approximately 4 cm on the z-axis and 2 cm on the x-axis.

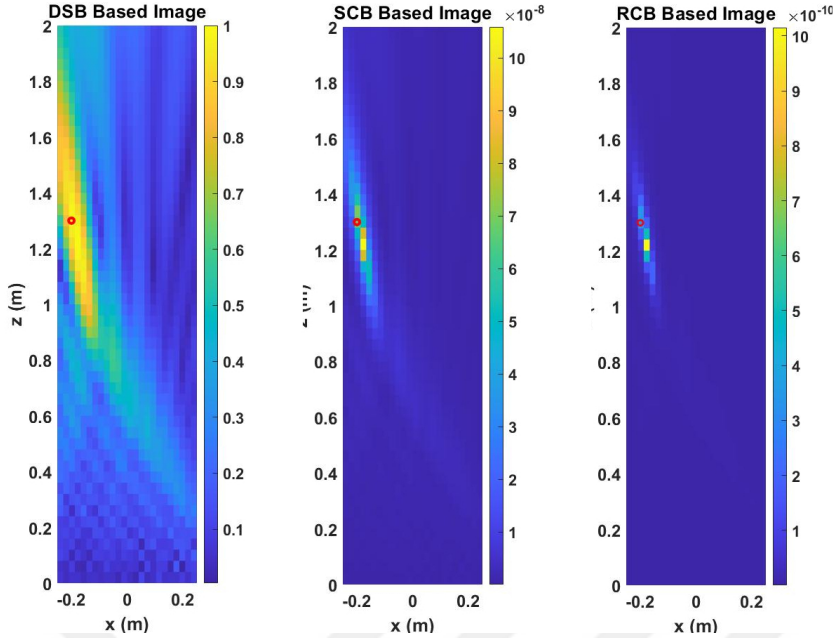


Figure 5.12 HBF results with image formation algorithm from NLS-3 at x=-20 cm, y=86 cm, z=130 cm

5.2.6 Measurement-6

In this study, the position of the NLS-3 target placed in the previous scenario is kept constant, and a linear RCS target, RCS-2, has been placed in the measurement environment, as shown in Figure 5.13. The conical aluminum target has been positioned 30 cm away on the x-axis from the NLS-3 (x=10 cm, y=86cm, and z=130 cm). As a result of this measurement, the effect of a linear clutter target on the harmonic radar has been analyzed.

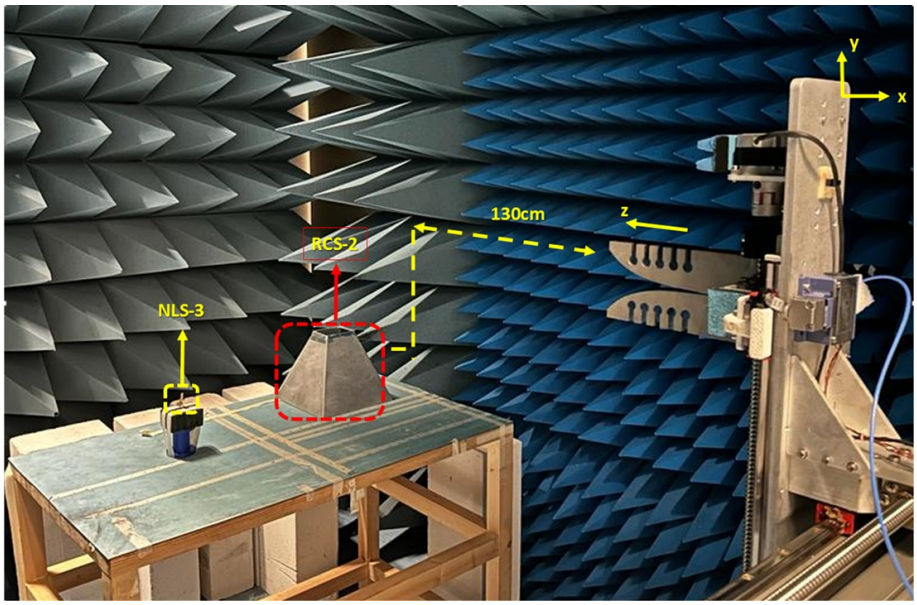


Figure 5.13 The placement of the NLS-3 and RCS-2 in the scanning area for measurement-6

When the measurement results are examined, as illustrated in Figure 5.14, it is observed that the tapered aluminum linear target has not been detected in any of the image formation algorithm results. There are negligible differences compared to the measurements performed in Measurement-5 without the tapered aluminum target. When the results of SCB and RCB algorithms were analyzed, although the target localization and resolution are good, clouding around the target has been observed.

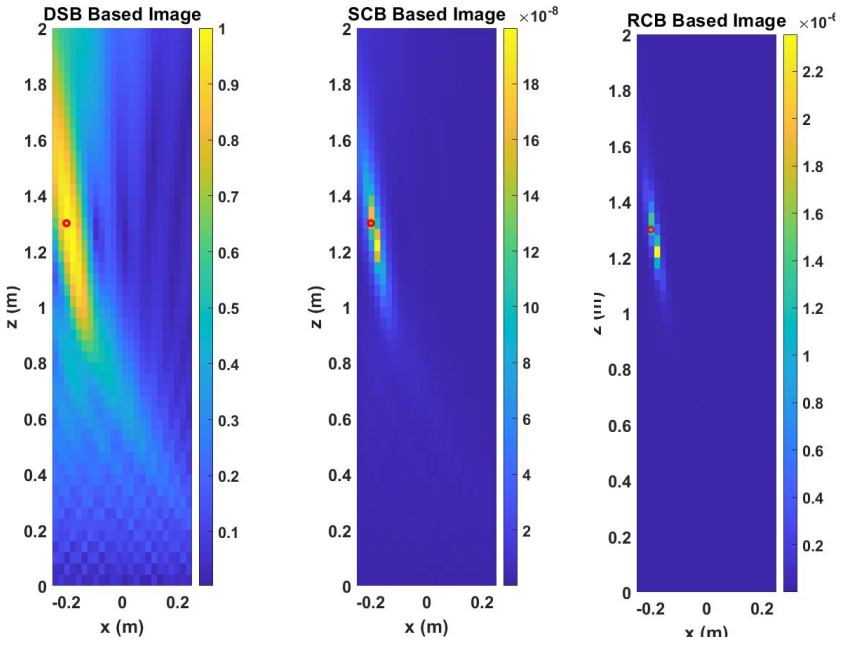


Figure 5.14 HBF results with image formation algorithm from NLS-3 at x=-20 cm, y=86 cm, z=130 cm

5.2.7 Measurement-7

As shown in Measurement-7, the NLS-1 target has been placed on a 10 cm long ABS material on a wooden table at x=10 cm, y=86 cm, and z=130 cm. As shown in Figure 5.15, there is no linear RCS target in the measurement area, only NLS-1.

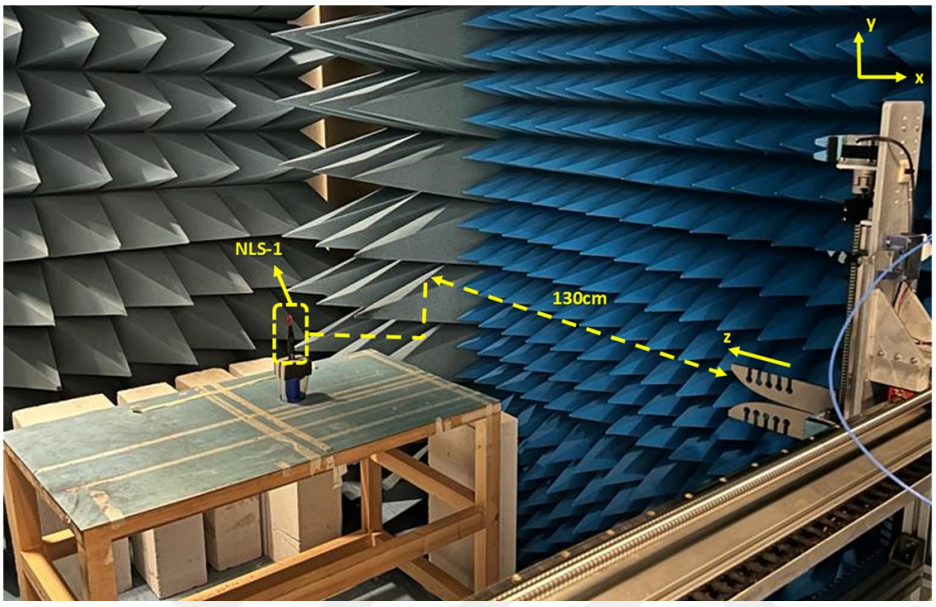


Figure 5.15 The placement of the NLS-1 in the scanning area for measurement-7

An analysis of the HBF measurement results presented in Figure 5.16 shows that while the DSB algorithm accurately positions the center of the target along the z-axis, there is a noticeable amplitude spread of approximately 60 cm in the x-axis. Regarding focusing and resolution, it is clear that the DSB algorithm underperforms compared to SCB and RCB algorithms.

Upon examining the SCB and RCB algorithms as shown in Figure 5.16, it is evident that they have provided considerably better localization and resolution than the DSB algorithm results. Although the results of the SCB algorithm outcomes slightly clouding the effect around the target, the normalized amplitude results show that the target position can be detected with a shift of approximately 4 cm in the x and z axis. A similar phenomenon is observed with the RCB algorithm's localization capabilities.

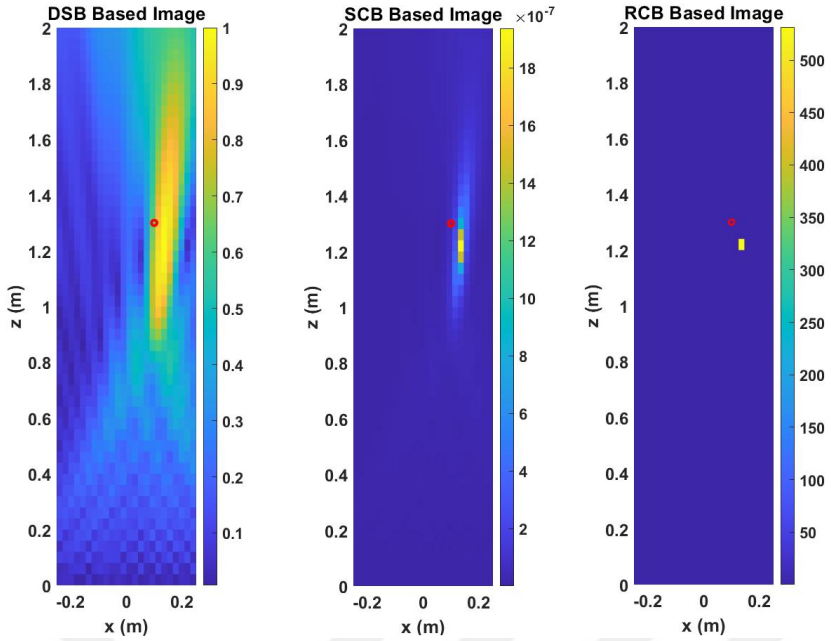


Figure 5.16 HBF results with image formation algorithm from NLS-1 at x=10cm, y=86cm, z=130cm

5.2.8 Measurement-8

In this experimental study, the NLS-1 target has been placed on a wooden table and ABS material with coordinates of x=-20 cm, y=86 cm, and z=130 cm. The environment has no linear RCS target, as illustrated in Figure 5.17.

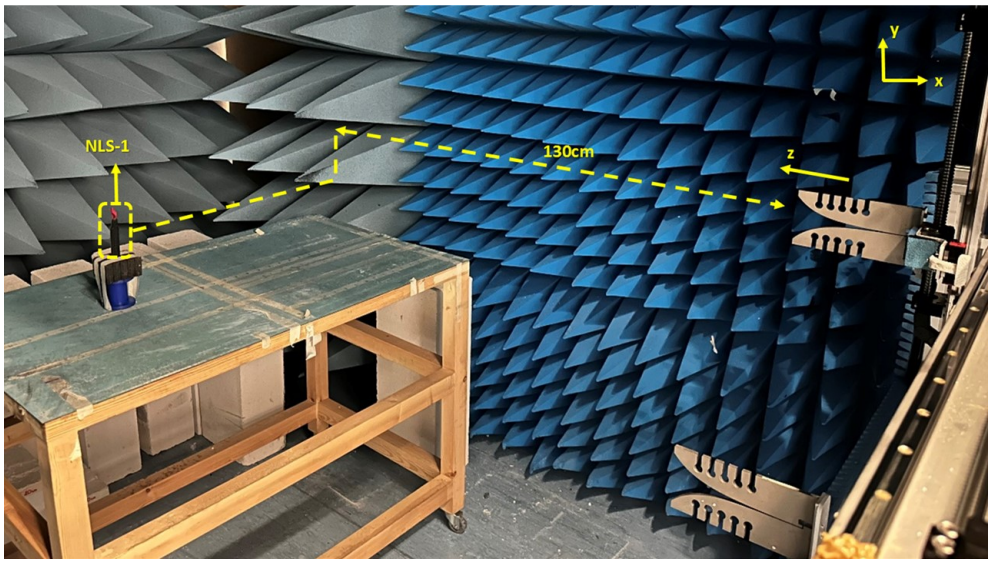


Figure 5.17 The placement of the NLS-1 in the scanning area for measurement-8

The HBF measurement results show the detection of the NLS-1 target by all tested image formation algorithms, as illustrated in Figure 5.18. It is clear that RCB and

SCB improve the localization and resolution of NLS-1. Despite the clouding effect, the normalized data shows that both algorithms could successfully detect the target position with minor axial and lateral displacement.

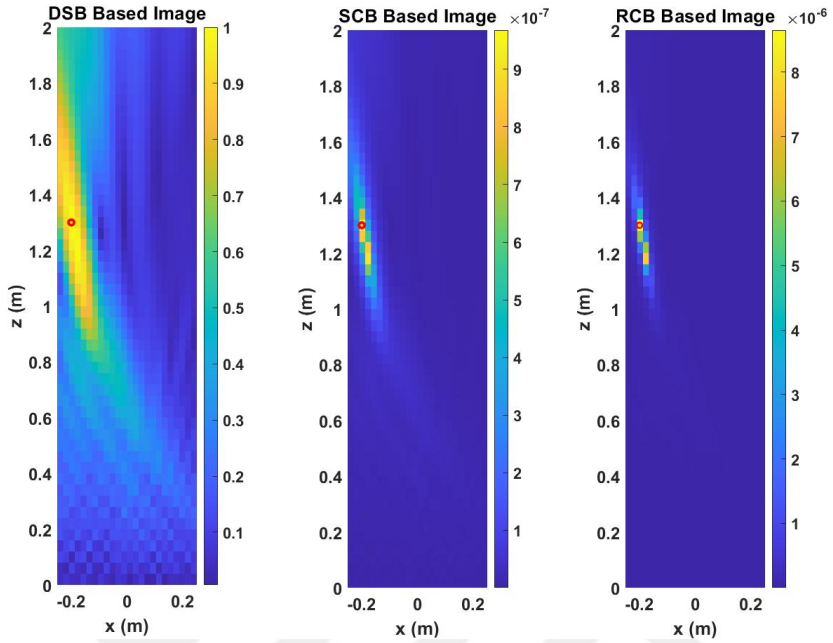


Figure 5.18 HBF results with image formation algorithm from NLS-1 at x=-20 y=88 z=130cm

5.2.9 Summary of Conventional Beamformer 2-D Image Formation Result

In this section, the summary of eight scenarios of nonlinear scatterers' 2-D images formed by conventional beamformers are investigated in terms of resolution, localization, and focusing. The measurement area has been divided into 25 pixels on the x-axis and 51 on the z-axis. 1275 pixels have been employed to form a 2-D image of nonlinear scatterers. According to the image formation results, it can be concluded that all nonlinear scatterers placed in the measurement area have been identified and localized by DSB, SCB, and RCB, respectively.

As can be seen from the experimental results, although the DSB algorithm is able to localize the target position on the x-axis accurately, it falls behind the capon-based beamformer structures in comparative results due to the wide amplitude distribution on the z-axis. Furthermore, in addition to this amplitude distribution, the clouding effect occurred in a given measurement scene and target surroundings. Therefore, the DSB beamformer performs poorly and is not as effective in accurately locating and resolving nonlinear scatterers.

5.3 Experimental Studies on RBFNN Based Microwave Imaging of Nonlinear Scatterers

In this section, the implementation of the radial basis function neural network-based beamformer architecture has been developed in order to create a 2-D HBF image of the NLS. The scenarios used in this section are the same as those used in section 5.2. Herein, only SCB and RCB beamformers have been considered due to a capon-based beamformer containing complex calculation processes like covariance matrix inversion and possible iteration processes (especially in RCBs), which are less ideal solutions for real-time applications. These algorithms can be restructured into an architecture, thereby enhancing their potential for integration into real-time systems.

The radial basis neural network is an exemplary choice for its basic architecture, and it can approximate beamformer weights with considerable precision. First, input-output relations must be determined to begin the construction of RBFNN architecture. In previous studies [60], the Wiener Solution method has been employed for the output computation of the RBFNN architecture. Although this method provides a general and acceptable approach for far-field 1-D beamforming applications, its performance metrics in terms of target resolution, localization accuracy, and noise suppression are not optimal for the more complex demands of near-field 2-D High-Resolution harmonic beamforming radar (HBF) imaging applications. Hence, in this thesis, SCB and RCB weight calculations are used as the output matrix of RBFNN.

The weights calculated by SCB and RCB are used as the output layer, and the calculated covariance R matrices are used as the input layer of the RBFNN. The input-output mapping relation is constructed by RBFNN training with P nearfield scanning point (a.k.a grid points) [61] .

$$(R^m; w^m_{\text{scb/rcb}}), \quad m = 0, 1, \ldots, P-1 \tag{5.13}$$

As shown in 4.26, the network has three layered feed-forward architecture. In the hidden layer of the RBFNN, the activation function is generally considered a Gaussian function. As given in 5.14, the supervised learning procedure has been utilized from the hidden layer to the output layer. Assume that input, hidden, and output layers have L, K, N nodes thus network output vector (w_n) is given by;

$$w_n = \sum_{k=1}^{K} \omega_{n,k} e^{-\frac{\|x-c_k\|^2}{\sigma_k^2}} \quad (n = 1, \ldots, N) \tag{5.14}$$

where $\mathbf{c}_k$ and σ_k are the center vector and the standard deviation (spread parameter) of the nth Gaussian function, respectively, and $\{\omega_{n,k}; n = 1, \ldots, N; k = 1, \ldots, K\}$ is the weight from the kth hidden node to nth output node.

To reduce the training time of RBFNN, a fast training approach is adopted, in which only the upper or lower triangular part (excluding the main diagonal) of the covariance matrix R from [61, 62] is considered in literature.

$$\boldsymbol{\kappa} = [R_{12}, R_{13}, \ldots, R_{1,M}; R_{23}, \ldots, R_{2,M}; \ldots; R_{(M-1),M}] \tag{5.15}$$

On the other hand, in this study, the first row of $M \times M$ covariance matrix R is reorganised as an input vector with $[Mx1]$ components;

$$\boldsymbol{\kappa} = [R_{12}, R_{12}, R_{13}, \ldots, R_{1M}] \tag{5.16}$$

Moreover, note that the network needs twice as many input nodes because it does not deal with complex numbers. The input vector is then normalized by its norm to unify the input parameter space.

$$\hat{\boldsymbol{\kappa}} = \frac{\kappa}{\|\kappa\|} \tag{5.17}$$

Once the required input and output set has been established, as given in (5.13), the trained RBFNN neural network can be recalled in order to respond to inputs that have never been seen before. The optimum beamformer weights are computed using an RBFNN. The optimal weights are obtained by solving this optimization problem, which requires knowledge of the covariance matrix of the received signal and the steering vector of the desired signal. For a nearfield and 2-D image construction of an NLS, the RBFNN is trained with sources randomly placed in a rectangular region in the nearfield of the ULA. In this study, 25 pixels on the x-axis and 51 pixels on the z-axis, totaling 1275 pixels, P, have been considered in order to train the RBFNN-based beamformer. Only a single source point is present for each training sample. The array output covariance matrix is computed for each source point, i.e., the training sample. Using the covariance matrix, the SCB/RCB

weights are computed for each grid point (pixel) of an image region containing the source. Each training sample contains the optimum weights for all grid points using the covariance matrix for a single source located at an image pixel and the ULA response for the source. New samples are obtained by varying the location of the source. The calculation of radial basis weights procedure could be summarized as follows;

1) Using (5.13) and (5.14), the covariance matrix R has been rearranged to vector $\hat{\boldsymbol{\kappa}}$, given in (5.17)

2) Neuron nodes has been defined manually on grid points, not by clustering algorithms (K nodes).

3) Each input vectors and neuron centers distances have been measured by gaussian activation function given as $e^{-\frac{\|x-c_k\|^2}{\sigma_k^2}}$ then the result of this layer has been used to produce design matrix, $\boldsymbol{\varphi}$, $[LxK]$.

$$\boldsymbol{\varphi w} = \boldsymbol{d} \tag{5.18}$$

4) In order to calculate the basis weights, $\boldsymbol{w}$, as in 5.18), the output matrix, $\boldsymbol{d}$, needs to be calculated by employing (5.11) or (5.12). Thus, by employing pseudo-inverse of the design matrix, $\boldsymbol{\varphi}^{\dagger}$, and multiplying this matrix by output matrix, the radial basis weights has been calculated.

In the following section, the experimental studies initially conducted in Section 5.2, which include using DSB, SCB, and RCB algorithms, are repeated experimentally with the RBFNN beamformer. The network structure has been used in both SCB and RCB beamformer approaches to train RBFNN.

5.3.1 Measurement-1

The first scenario described in Figure 5.19, the NLS-1 has been positioned in the measurement area with coordinates x=0 cm, y=84.5 cm, and z=197 cm. Compared to conventional beamformer algorithms, the results of the RBFNN beamformer have successfully localized the NLS-1 position with a high accuracy. The 2-D image results of RBFNN beamformers have been trained with RCB and SCB algorithms are shown in Figure 5.20. When compared with the delay and sum algorithm, it is seen that the RBFNN-SCB and RBFNN-RCB beamformer structures are much ahead in terms of localization and resolution of the target.

However, comparisons of image formation times are discussed in detail in the next section.

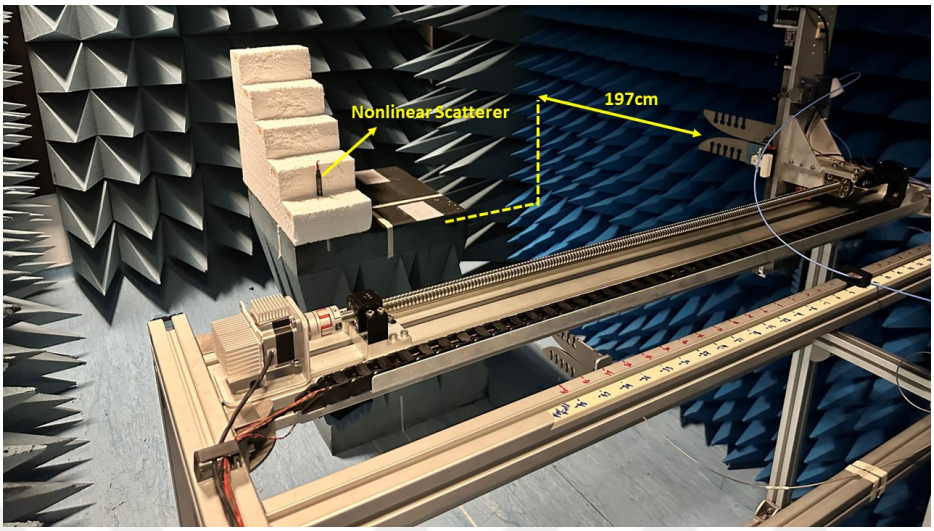


Figure 5.19 Measurement area of scenario-1 and NLS-1 at x=0 y=84.5 z=197cm

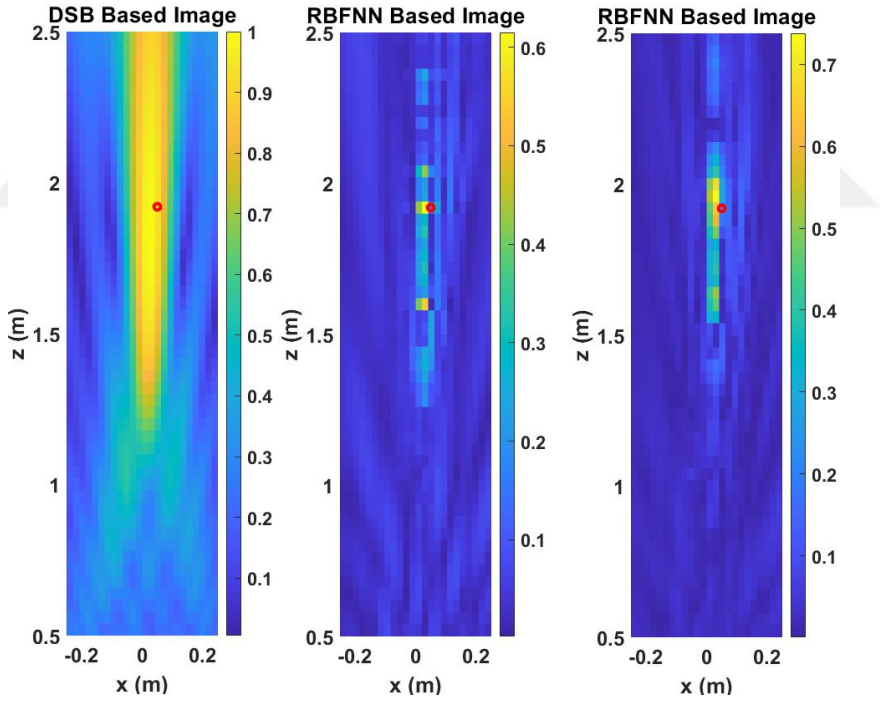


Figure 5.20 HBF Imaging Comparisons: DSB (Left), SCB (Mid) and RCB (Right) Trained RBFNN Beamformers Analyzing NLS-1 at coordinates x=0, y=84.5, z=197 cm

As can be seen in Figure 5.20, there are some amplitutes occured around the NLS-1. However, although some amplitudes are generated around the RBFNN-based images, they are considerably lower than the result of the DSB beamformer structure.

5.3.2 Measurement-2

In this scenario, as shown in Figure 5.21, the NLS-1 target has been shifted from x=0 to x=-17.5 cm and positioned 118 cm on the z-axis. In addition, the RCS-1 target has positioned vertically from the NLS-1 target so that it was right next to the x-axis. The observations in Figure 5.22 reveal that NLS-1 has successfully detected and positioned by both SCB and RCB trained Radial Basis Function Neural Network (RBFNN) beamformers. In addition, some amplitudes have generated around the target and no evidence of the RCS-1 target has found.

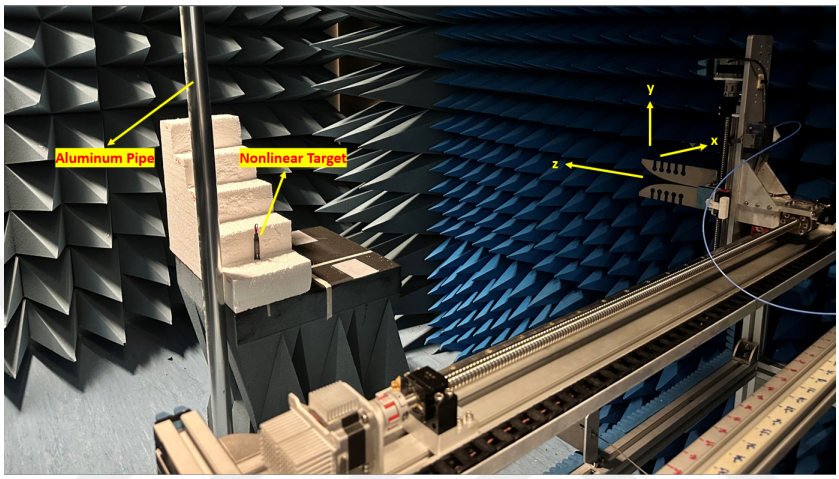


Figure 5.21 Measurement area of scenario-2 and NLS-1 and RCS-1 at x=-17.5 y=84.5 z=118 cm

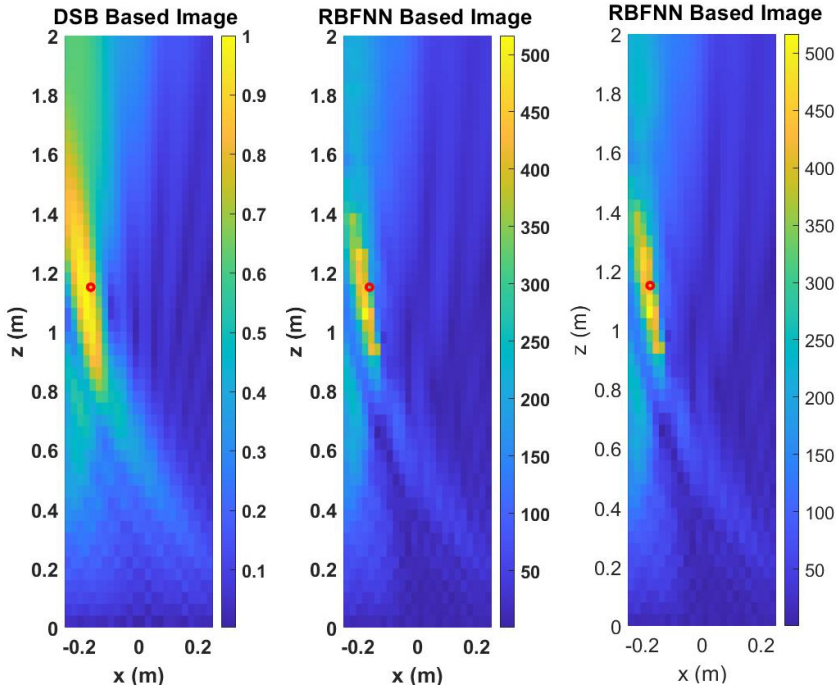


Figure 5.22 HBF Imaging Comparisons: DSB (Left), SCB (Mid) and RCB (Right) Trained RBFNN Beamformers Analyzing NLS-1 and RCS-1 at coordinates x=-17.5, y=84.5, z=118 cm

Figure 5.22, the DSB beamformer structure finds the approximate position of the NLS-1 target accurately on the x-axis but fails to locate it on the z-axis because the amplitude spread starts at 90 cm and extends up to 160 cm. However, when the RBFNN-trained beamformer results are analyzed in detail, it can be seen that RBFNN-RCB has slightly better localization on the target. While RBFNN-SCB detected NLS-1 at 110 cm, RCB-based RBFNN detected NLS-1 at 115 cm, only 3 cm offset in the z-axis. Also, both beamformers have a shift of 2 cm in the x-axis.

5.3.3 Measurement-3

This measurement scenario includes the NLS-2 target, which has been positioned at the coordinates of x=0 (centered), y=84.5, and z=144 cm. Considering the findings from the beamforming analysis in Figure 5.23 shows that all three beamformers have identified and localized the NLS-2 in a given scene.

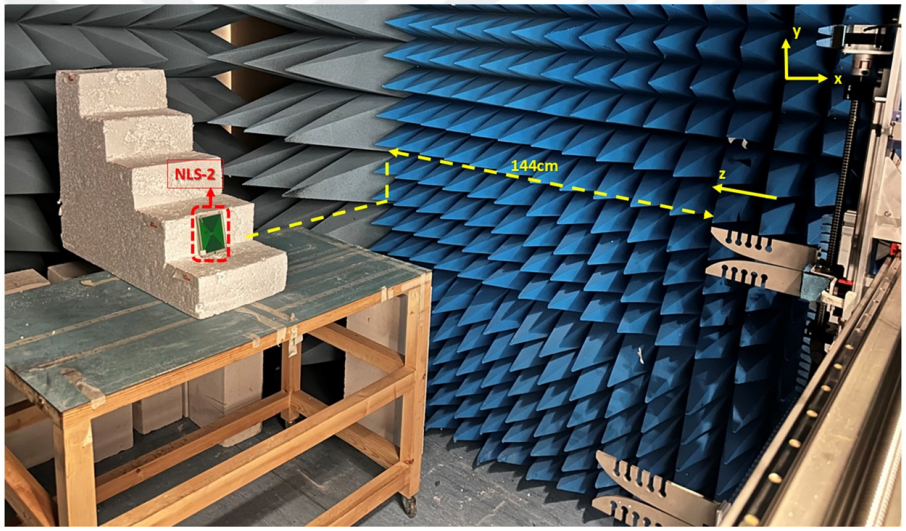


Figure 5.23 Measurement area of scenario-3 and NLS-2 at x=0 y=84.5 z=144 cm

In Figure 5.24, the DSB beamformer has correctly detected the approximate position of the NLS-2 target on the x-axis. Still, it has failed to detect it on the z-axis due to the amplitude spread starting from 110 cm and extending up to 250 cm. However, when the results of the beamformer trained with RBFNN are examined in detail, it can be seen that RBFNN-RCB has better localization on the target. Although the RBFNN-SCB beamformer found the target position on the x-axis with a shift of 2 cm, it detected the target position on the z-axis at approximately 160 cm with a shift of approximately 15 cm. On the other hand, the RCB-based RBFNN beamformer detected NLS-2 at 145 cm in the z-axis, even though amplitude spread in the z-axis.

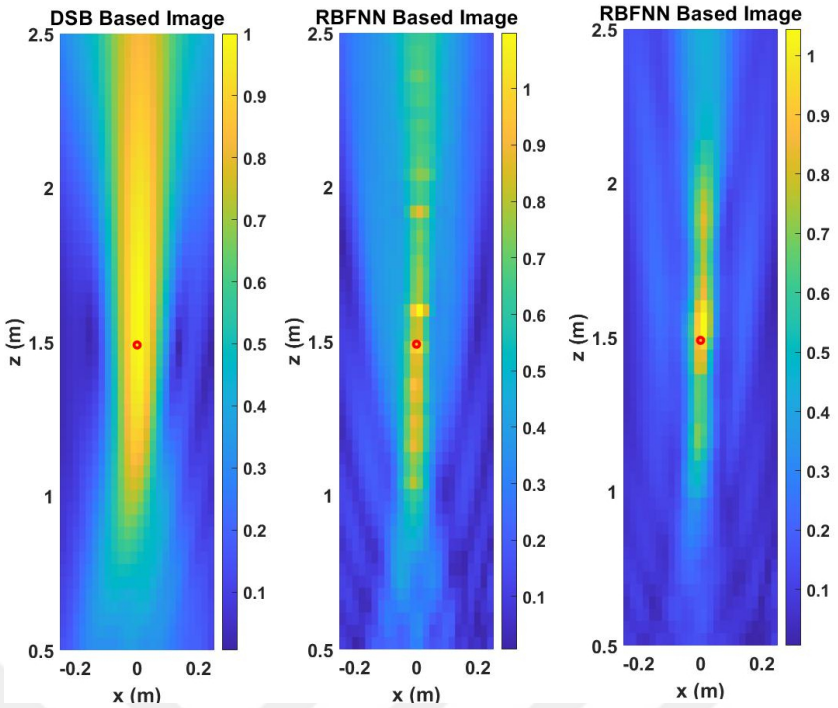


Figure 5.24 HBF Imaging Comparisons: DSB (Left), SCB (Mid) and RCB (Right) Trained RBFNN Beamformers Analyzing NLS-2 at coordinates x=0, y=84.5, z=144 cm

5.3.4 Measurement-4

In this measurement scenario, the NLS-1 target has been positioned on x= 0 cm, y= 84.5 cm, and z= 118 cm. According to Figure 5.25, the target has been identified by conventional beamformers.

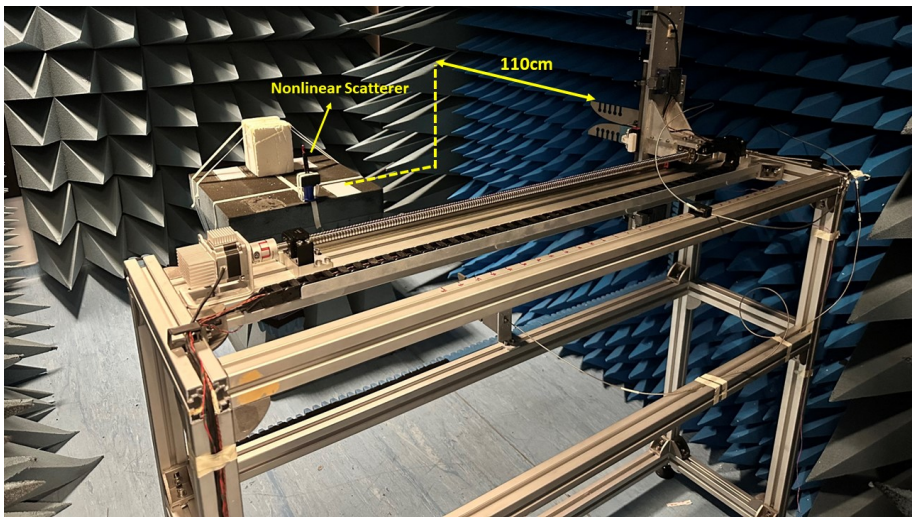


Figure 5.25 Measurement area of scenario-4 and NLS-1 at x=0 y=84.5 z=118 cm

Based on the RBFNN-trained beamformer outcomes as illustrated in Figure 5.26, it is observed that the RBFNN beamformers showed an excellent approximation of localization along the z-axis but experienced minor lateral deviations on the x-axis, 2 cm, like conventional SCB and RCB. Additionally, from the RBFNN beamformer's result, it can be concluded that the RBFNN-RCB provides a marginally improved spread of amplitudes around the target. Furthermore, once the DSB result is investigated, it can be concluded that the DSB-based beamformer localized the NLS-1 on the x-axis. Still, a significant amplitude spread over the z-axis occurred. Therefore, poor localization and resolution performance have occurred in DSB beamformers compared to RBFNN-based beamformers.

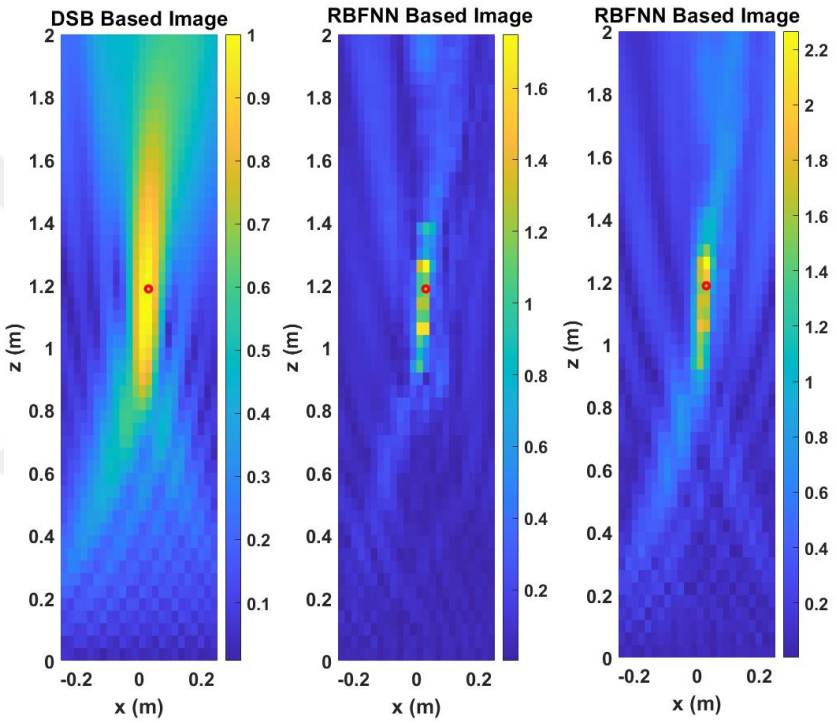


Figure 5.26 HBF Imaging Comparisons: DSB (Left), SCB (Mid) and RCB (Right) Trained RBFNN Beamformers Analyzing NLS-1 at coordinates x=0, y=84.5, z=118 cm

5.3.5 Measurement-5

In this measurement scenario, as shown in Figure 5.27, the NLS-3 is placed on a wooden table and an ABS material at coordinates x=-20, y=86, and z=130 cm.

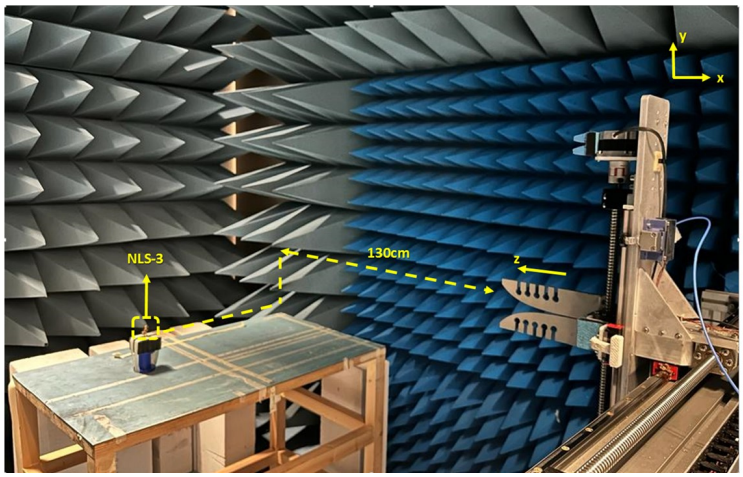


Figure 5.27 Measurement area of scenario-5 and NLS-3 at at x=-20 y=86 z=130cm

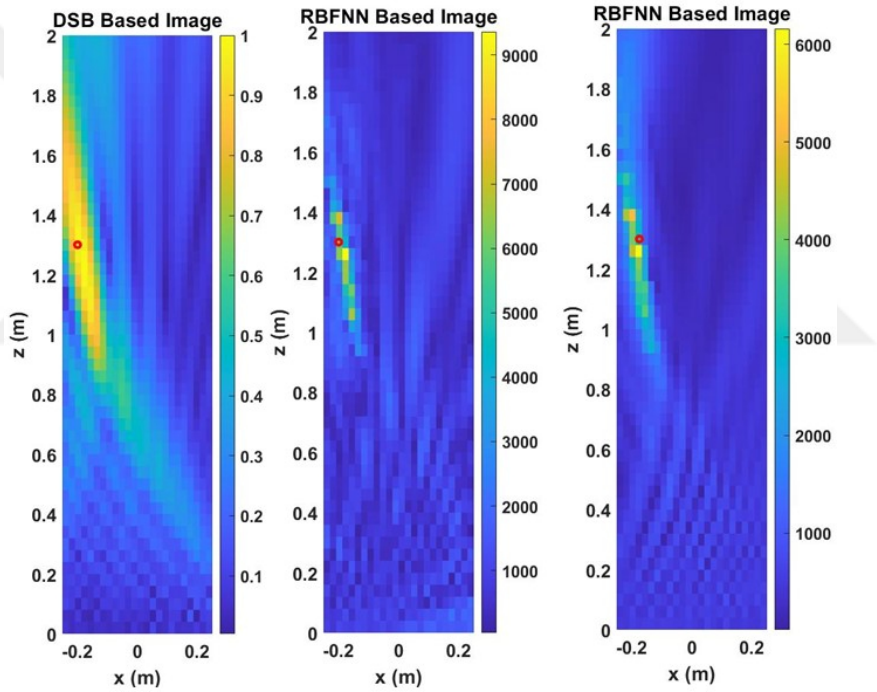


Figure 5.28 HBF Imaging Comparisons: DSB (Left), SCB (Mid) and RCB (Right) Trained RBFNN Beamformers Analyzing NLS-3 at coordinates x=-20, y=86, z=130 cm

As indicated in Figure 5.28, it is clear that the two RBFNN-based beamformers are able to detect and position the NLS-3 in a given measurement scenario. While the RBFNN-SCB and RBFNN-RCB beamformers are effective in target detection and positioning, the RBFNN-RCB beamformer is one step ahead regarding precise localization. It can detect NLS-3 with only a 1 cm deviation in the x-axis. On the other hand, the DSB beamformer has no difficulty localizing the target on the x-axis. Still, the z-axis has an amplitude distribution ranging from 90 cm to 170 cm

around the target. Therefore, the DSB beamformer performs much worse than the RBFNN-based beamformers in terms of localization and resolution.

5.3.6 Measurement-6

As seen in measurement scenario-6, the RCS-2 target has been placed 30 cm away from the NLS-3 target on the x-axis, as shown in Figure 5.29. The position of the NLS-3 target is x=-20, y=86, and z=130 cm.

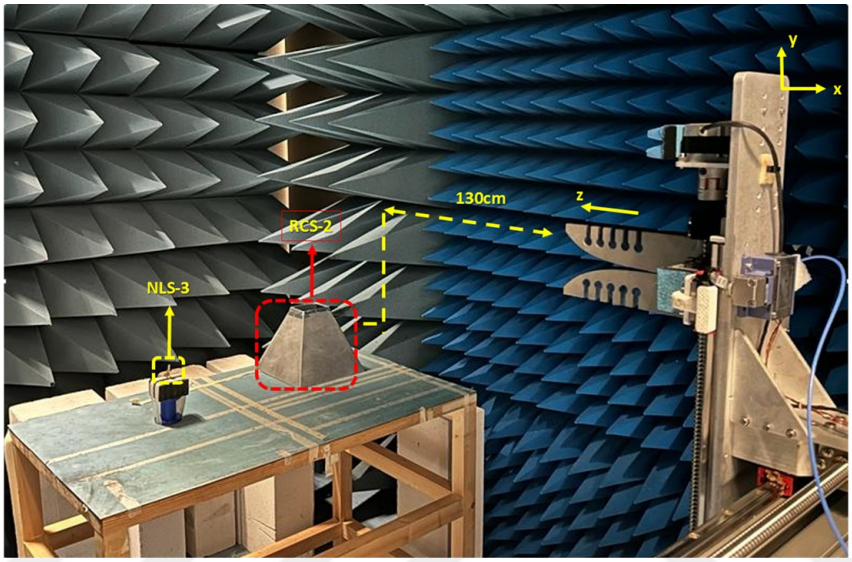


Figure 5.29 Measurement area of scenario-6 and NLS-3 and RCS-2 at x=-20 y=86 z=130cm

When examining RBFNN-based beamformer structures, it is observed in Figure 5.30 that the RBFNN-RCB achieves approximately 2 cm better positioning on the z-axis compared to the RBFNN-SCB. Furthermore, both beamformer structures have successfully located the NLS-3 target. Additionally, although some amplitude distribution is observed around the target in both RBFNN-based beamformer structures, the 2-D image of RBFNN-RCB displays slightly less amplitude distribution and a more focused image compared to the RBFNN-SCB beamformer. Despite the RCS-2 target having been located 30 cm to the right on the x-axis from the NLS-3 target, it has not exhibited any presence in the 2-D image as expected. On the other hand, when examining the DSB beamformer structure, although it has accomplished localizing on the z-axis, it shows an amplitude distribution extending from 100 cm to 180 cm on the x-axis. Therefore, regarding localization and resolution, the DSB structure is significantly inferior to the RBFNN-based structures.

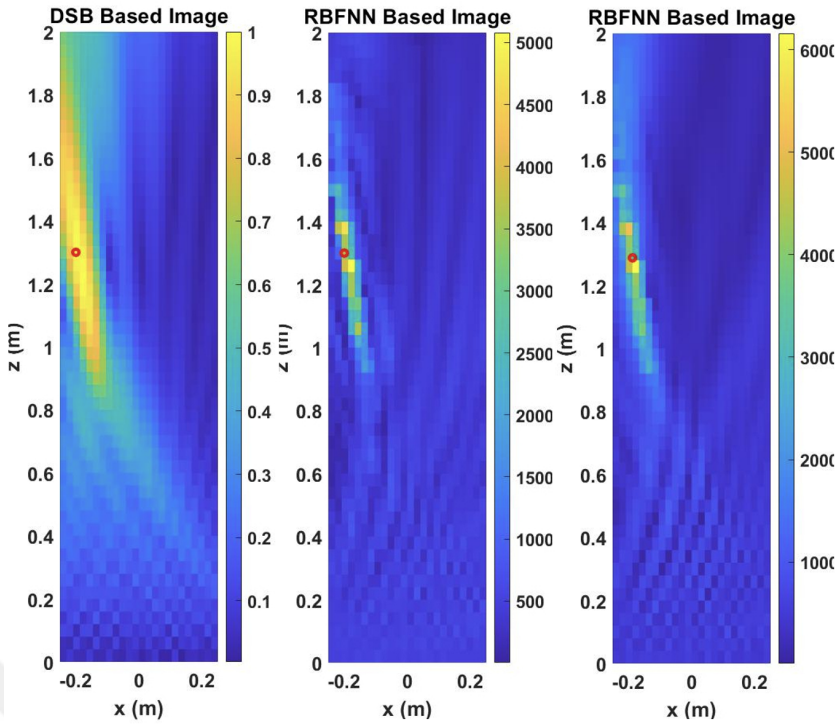


Figure 5.30 HBF Imaging Comparisons: DSB (Left), SCB (Mid) and RCB (Right) Trained RBFNN Beamformers Analyzing NLS-3 and RCS-2 at coordinates x=-20, y=86, z=130 cm

5.3.7 Measurement-7

In measurement scenario-7, the NLS-1 scatterer has been placed on a wooden table and ABS material, as shown in Figure 5.31. NLS-1 has been positioned on x=10, y=86, and z=130 cm in a given scanning area. The DSB, RBFNN-RCB, and RBFNN-SCB beamformer results have been compared in terms of localization, resolution, and amplitude spread on both axes.

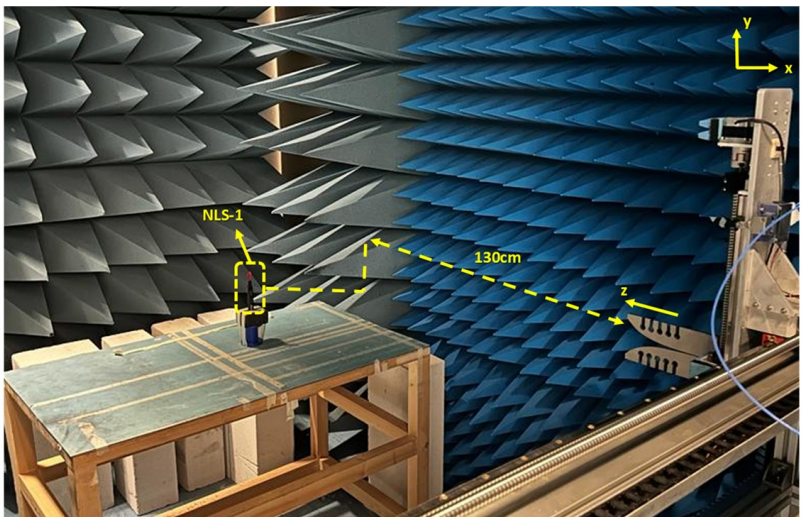


Figure 5.31 Measurement area of scenario-7 and NLS-3 at x=10 y=86 z=130cm

As observed from Figure 5.31, although the results from RBFNN-RCB and RBFNN-SCB appear similar, RBFNN-RCB leads in localization when compared to the other RBFNN-based beamformer structure. Furthermore, although artifact formation is observed at z=110 cm in both beamformer structures, its amplitude is more dominant in RBFNN-SCB than RBFNN-RCB. The RBFNN-SCB beamformer detected the target at x=12.5 cm and z=125 cm, while the RBFNN-RCB beamformer successfully located the target at x=12.5 cm and z=128 cm. A certain amount of amplitude formation around the target is observed for both beamformer structures. On the other hand, when examining the DSB beamformer, shifts are observed both on the x-axis and z-axis compared to the RBFNN-based beamformer structures. There is an approximate shift of 5 cm on the x-axis and an amplitude distribution extending from 100 cm to 170 cm on the z-axis. Therefore, in terms of localization, focus, and resolution, the DSB beamformer falls behind the RBFNN-based beamformers.

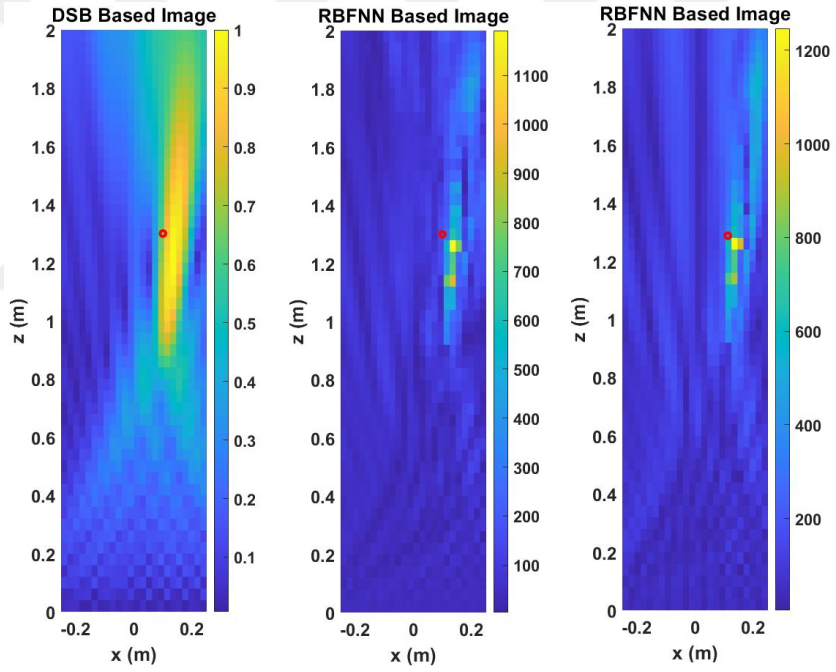


Figure 5.32 HBF Imaging Comparisons: DSB (Left), SCB (Mid) and RCB (Right) Trained RBFNN Beamformers Analyzing NLS-1 at coordinates x=10, y=86, z=130 cm

5.3.8 Measurement-8

As illustrated in Figure 5.33, measurement-8 shows that the NLS-1 has been relocated from x=10 cm to x=-20 cm in a given scenario. NLS-1 has been placed on a wooden table and an ABS material at the coordinates of x=-20, y=86, and z=130cm.

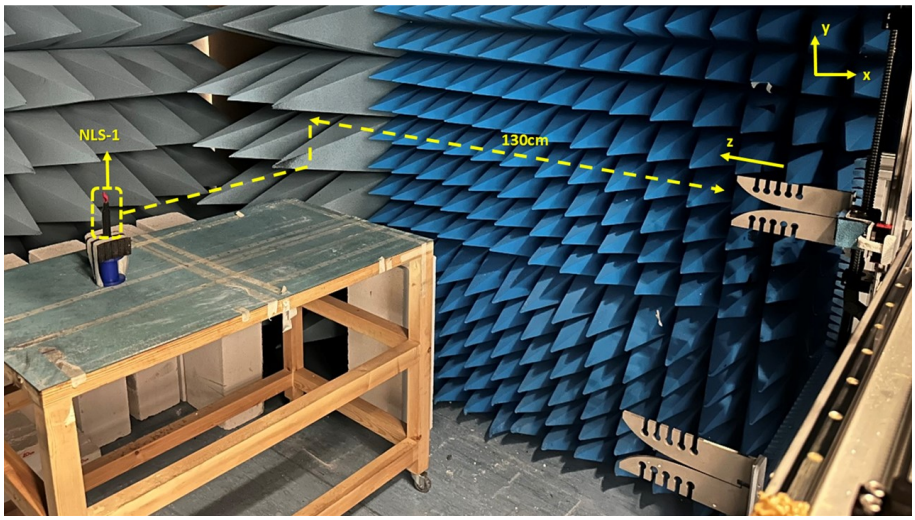


Figure 5.33 Measurement area of scenario-8 and NLS-1 at x=-20 y=86 z=130cm

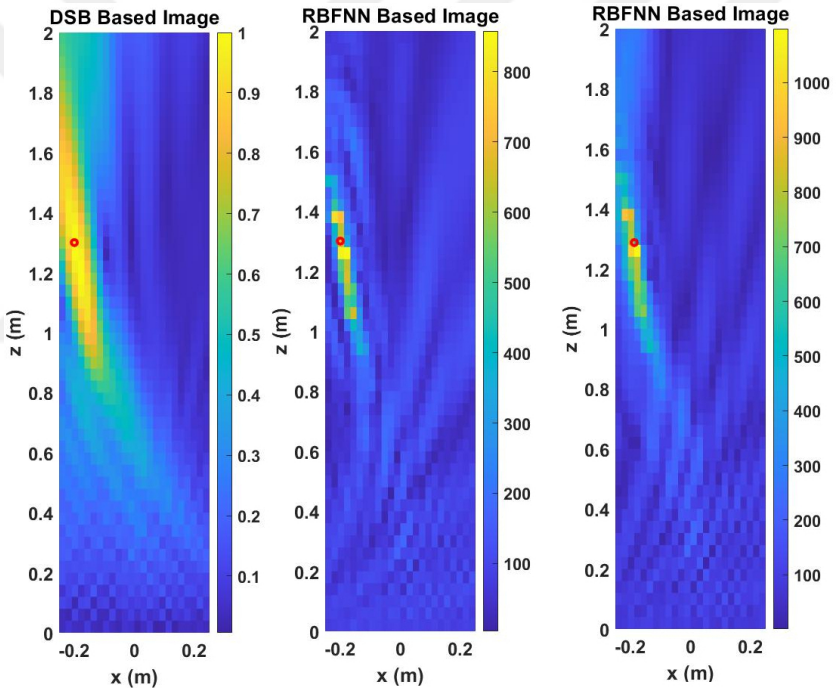


Figure 5.34 HBF Imaging Comparisons: DSB (Left), SCB (Mid) and RCB (Right) Trained RBFNN Beamformers Analyzing NLS-1 at coordinates x=-20, y=86, z=130 cm

Results from the HBF measurement, as depicted in Figure 5.34, provide the successful detection and localization of the NLS-1 target in a given scene. Compared to the DSB beamforming results, the RBFNN-SCB and RBFNN-RCB notably enhanced the localization and resolution of the target. The DSB beamformer has a wide amplitude spread along with the z-axis from 100cm to 170 cm. Thus, it does not provide the exact location of the NLS-1. The RBFNN beamformer results show that RBFNN-RCB and RBFNN-SCB exhibit a higher

degree of clouding suppression and minor deviation on target localization, estimated to be around 2 cm, both x and z-axes. It is observed that the DSB beamformer structure gives significantly worse results than the RBFNN-based beamformer structures due to localization and wide amplitude spread.

5.3.9 Summary of 2-D DSB and RBFNN Based Image Formation Results

This section details the measurement conducted with eight scenarios involving three nonlinear and two linear scatterers. In order to create a scanning area in the near-field of the antenna array, 25x51 pixels, totaling 1275 pixels, have been employed. The RBFNN-based beamformer structures (a.k.a RBFNN-SCB and RBFNN-RCB) have been developed upon these near-field scanning areas. Additionally, in order to evaluate and compare the results of the RBFNN beamformers, the conventional DSB beamformer has been employed. Due to the fast image formation timing, the DSB beamformer has been chosen. Beamformers have been compared and evaluated using the criteria of localization, resolution, and focusing parameters.

The comparison results revealed that the DSB beamformer results provide reasonable accuracy on the x-axis localization, but it suffers from significant amplitude dispersion along the z-axis. Consequently, in terms of localization, resolution, and focusing performance parameters, the DSB beamformer is markedly outperformed by the RBFNN-based beamformers. On the other hand, an in-depth analysis of the RBFNN-based beamformer structures shows certain scenarios that the RBFNN-RCB structure is better than the RBFNN-SCB structure in terms of localization and resolution in some scenarios, despite their similar performance in other cases. The RBFNN-RCB structure outperforms the RBFNN-SCB beamformer structure due to its lower amplitude dispersion around the target and ability to locate it with higher focus and resolution.

5.4 Image Formation Timing Analysis of Conventional and Neural Network Based Beamformers

This section compares beamformers' results regarding image formation and RBFNN training time. The conventional beamformers' image formation timing results for DSB, SCB, RCB, and RBFNN-based beamformers have been investigated and discussed here. Additionally, the training and image formation times of the RBFNN-based beamformer structures are analyzed at the end of the chapter.

In order to compare the image formation times accurately, each algorithm has been run 100 times, and the average time has been taken.

Table 5.1 shows the computational time required for the DSB, SCB, and RCB beamformers to form an image of NLS-1 in scenario-1 directly. The DSB beamformer gives the fastest result with 0.0067 seconds but lags behind the other two beamformers in terms of resolution and accuracy as shown in Figure 5.4. On the other hand, the SCB algorithm, which has relatively higher resolution and localization than DBS, provided a very fast solution with 0.012 seconds. When the image formation times are analyzed with RBFNN-trained beamformers, it is observed that the neural network subjected to SCB-based training, RBFNN-SCB, does not show any enhancement in image formation time. Conversely, when the RCB beamformer structure, which creates an image in 1.08 seconds with analytical calculations, is used in RBFNN training, the image formation time decreases to approximately 0.011 seconds, which means approximately 98 times speedup. As a result of this image formation timing enhancement, the RBFNN-RCB beamformer produces images of the nonlinear scatterer at speeds comparable to the DSB with notably enhanced accuracy, resolution, and localization.

Table 5.1 Scenario-1 timing results of the beamformers

Beamformer	**Image Formation Time (s)**	**Training Time (s)**
DSB	0.0067	N.A.
SCB	0.012	N.A.
RCB	1.08	N.A.
RBFNN-SCB	0.012	133.7
RBFNN-RCB	0.011	138.3

Table 5.2 presents the timing result of scenario-2's conventional and neural network-based beamformer results. The conventional beamformer results are 0.007 seconds for DSB, 0.0012 seconds for SCB, and 1.012 seconds for RCB. Despite its speed, DSB falls short in resolution and target localization accuracy. While RBFNN-based beamformers are examined, RBFNN-SCB does not give any boost on time compared to SCB algorithm results. On the contrary, a significant enhancement is observed with the RBFNN-RCB, which reduces image formation time from 1.012 seconds to 0.0009 seconds, nearly 112 times faster than the conventional RCB.

Table 5.2 Scenario-2 timing results of the beamformers

Beamformer	Image Formation Time (s)	Training Time (s)
DSB	0.007	N.A.
SCB	0.012	N.A.
RCB	1.012	N.A.
RBFNN-SCB	0.012	138.4
RBFNN-RCB	0.009	134.3

Table 5.3 shows the timing results of the image formation of both conventional and neural network-enhanced beamformers for measurement scenario 3. For conventional beamformers, the DSB beamformer completes the task in 0.0068 seconds, the SCB is 0,013 seconds, and the RCB is 1.42 seconds. Although the DSB beamformer is the fastest among these beamformers, it sacrifices accuracy and resolution in target localization. Based on the beamformer outcomes, it is observed that RBFNN-SCB does not improve processing time compared to its conventional SCB counterpart. On the other hand, RBFNN-RCB has been achieved significant improvements, such as 95 times speedup compared to conventional RCB.

Table 5.3 Scenario-3 timing results of the beamformers

Beamformer	Image Formation Time (s)	Training Time (s)
DSB	0.0068	N.A.
SCB	0.013	N.A.
RCB	1.42	N.A.
RBFNN-SCB	0.012	132.3
RBFNN-RCB	0.015	147.3

As shown in Table 5.4, the scenario-4 image formation timing results are presented. By employing conventional and RBFNN-based beamformers it can be concluded that the DSB gives the fastest results with 0.0059 seconds. However, it has the poorest results in terms of resolution, localization, and . The RBFNN-SCB structure did not improve in terms of time and image formation as in previous measurements. When examining the RBFNN-RCB timing results, it can be concluded that RBFNN-RCB has significantly enhanced the image formation process from 0.92 seconds to 0.0097 seconds, nearly 95 times faster than the conventional one.

Table 5.4 Scenario-4 timing results of the beamformers

Beamformer	Image Formation Time	Training Time
DSB	0.0059	N.A.
SCB	0.011	N.A.
RCB	0.92	N.A.
RBFNN-SCB	0.010	144.1
RBFNN-RCB	0.0097	128.8

The data presented in Table 5.5 shows that the DSB beamformer still has the best image formation time result compared to the SCB and RCB conventional beamformers. Furthermore, the SCB beamformer result is 0.010, and the RCB is 1.02 seconds in time result. Analyzing the images generated from RBFNN-based training, the RBFNN-RCB beamformer structure is considerably faster than the conventional RCB structure and completes the image generation in 0.010 seconds.

Table 5.5 Scenario-5 timing results of the beamformers

Beamformer	Image Formation Time (s)	Training Time (s)
DSB	0.0056	N.A.
SCB	0.010	N.A.
RCB	1.020	N.A.
RBFNN-SCB	0.010	141.2
RBFNN-RCB	0.010	119.1

When the image formation time for scenario-6 presented in Table 5.6 is analyzed, it is seen that the DSB algorithm completed the image formation in just 0.0052 seconds. This is closely followed by the SCB, which takes a marginally longer 0.0097 seconds. The RCB beamformer result is significantly slower, with an image formation time of 1.02 seconds.

When the neural network-enhanced beamformers are employed, they show timing results comparable to their conventional counterparts. Once the RBFNN-SCB beamformer results are investigated, it can be concluded that it has nearly the same timing result as its conventional counterpart, which is 0.0098 seconds. On the other hand, the image formation time result of the RBFNN-RCB indicates that despite the conventional RCB beamformer result's slow speed, the integration of RCB to a neural network-enhanced beamformer, RBFNN-RCB yields an image formation time nearly comparable to that of the DSB beamformer nearly 0.010 seconds.

Table 5.6 Scenario-6 timing results of the beamformers

Beamformer	Image Formation Time (s)	Training Time (s)
DSB	0.0052	N.A.
SCB	0.0097	N.A.
RCB	1.02	N.A.
RBFNN-SCB	0.0098	140.7
RBFNN-RCB	0.010	129.9

Considering the image formation time for scenario-7 as detailed in Table 5.7, it can be seen that the DSB beamformer accomplishes 0.006 seconds to complete a 2-D image of the NLS. The SCB follows this result by 0.0098 seconds, and the RCB beamformer has the slowest image formation time by 0.96 seconds.

It is apparent from the results that the RCB beamformer achieves a notably faster image formation time when coupled with an RBFNN training as RBFNN-RCB, which significantly accelerates its image formation to 0.010 seconds approaches the fast performance of the DSB beamformer. On the other hand, even if SCB is trained as RBFNN-SCB, there is no enhancement in image formation time.

Table 5.7 Scenario-7 timing results of the beamformers

Beamformer	Image Formation Time (s)	Training Time (s)
DSB	0.006	N.A.
SCB	0.0098	N.A.
RCB	0.96	N.A.
RBFNN-SCB	0.0097	140.7
RBFNN-RCB	0.010	129.9

Upon reviewing the image formation time for scenario-8 outlined in Table 5.8, the RCB beamformer has the slowest timing results with 1.09 seconds of image formation. On the other hand, when the image formation results of the other two conventional beamformer structures are analyzed, it is seen that the SCB beamformer has an image formation speed of 0.0094 seconds, and the DSB beamformer has an image formation speed of 0.0062 seconds. Furthermore, when the SCB-based neural network structure, called RBFNN-SCB, is investigated, it does not provide any enhancement in image formation timing. The RCB algorithm is relatively falls behind regarding image formation timing, it significantly improved the timing of image formation from 1.09 to 0.0098 seconds when trained with an RBFNN-based neural network structure. It can be concluded from this result that it is nearly 112 times faster than the conventional counterpart.

Once the RCB is enhanced by RBFNN training, it can rival the image formation speed of the DSB beamformer timing results.

Table 5.8 Scenario-8 timing results of the beamformers

Beamformer	Image Formation Time (s)	Training Time (s)
DSB	0.0062	N.A.
SCB	0.0094	N.A.
RCB	1.09	N.A.
RBFNN-SCB	0.0095	139.6
RBFNN-RCB	0.0098	141.9

5.4.1 Summary of 2-D Conventional and RBFNN Based Beamformer Timing Results

This section compares and evaluates the time required by conventional and RBFNN-based beamformers to form an NLS image within a specified 2-D scanning area. The conventional beamformer results reveal that the DSB beamformer gives the fastest result across all tested scenarios. Additionally, capon-based beamformers have been studied in this thesis, and the time taken to form an NLS image is noted.

In order to construct the covariance matrix of the measured RF signal, the SCB and RCB use different methodologies. The RCB beamformer uses iterative algorithms to calculate the beamformer weights instead of using a direct solution, as in the SCB beamformer. While the SCB beamformer employs a simpler and less computationally extensive methodology, the RCB employs a more complex and robust methodology. Additionally, the RCB has the ability to withstand array calibration errors and steering vector uncertainties. These computational differences increase the final image formation time. Thus, while the SCB beamformer structure provides a faster solution under ideal signal conditions, the RCB algorithm comes at the expense of increased computational time and requirements to design for robust performance in uncertain environments. Therefore, the RCB structure requires considerably more time and resources than the SCB structure.

When the RCB beamformer 2-D image formation results are analyzed, it is seen that the images formed with the RCB beamformer structure are significantly ahead of the images formed with the SCB and DSB structures in terms of localizing, resolution, and focusing performance. Therefore, one of the main objectives of this study is to accelerate the RCB beamformer-generated image with the minimum possible loss in performance. One of the most effective ways to achieve this is to calculate the RCB beamformer coefficients using a neural network.

When the RBFNN-based RBFNN-SCB and RBFNN-RCB structures are analyzed, no change in time is observed in the RBFNN-SCB structure compared to its conventional counterpart. On the other hand, the RBFNN-RCB structure is considerably faster than the conventional RCB structure. In all tested scenarios, an acceleration of up to approximately 100 times has been observed. This significant acceleration in the RBFNN-RCB beamformer underscores the effectiveness of integrating the RBFNN methodology into beamforming. This advancement provides an effective and efficient way to form an image in real-time applications.

In this study, it can be concluded that the RBFNN-based methods offer innovative solutions that improve efficiency and performance in time-critical applications such as high-speed data processing and image formation. They have great potential to shape complex signal processing and beamforming applications.

6
CONCLUSION

In this thesis, we have designed and constructed a beamforming radar system based on harmonic radar technology. Designing and constructing a reliable measurement system is a crucial task of this study to get precise imaging results of the NLS. The constructed HBF systems can transmit up to 40 dBm and suppress harmonics of the transmitted fundamental frequency over 120 dB. First, the measurements were acquired by a wide-band oscilloscope and signal generator-based system, HBF-1, to reveal the performance of the designed harmonic beamforming measurement system. Subsequent to the identification of NLS targets in a given scene and HBF-1's measurement performance verification, an SDR-based motor-controlled scanning system, the HBF-2, has been developed to make the system more portable and cost-effective.

By employing the HBF-2 measurement system, data have been collected from three different nonlinear scatterers and two linear RCS targets in eight scenarios. Contrary to literature Harmonic SAR studies, the transmit antenna has been fixed, and the receive antenna moved 3 cm apart during experimental studies. The linear targets have been used near the NLS targets to prove that the HBF system can suppress the fundamental frequency clutter.

Besides the measurement system verification studies, conventional algorithms delay and sum, Capon, and Robust Capon-based beamformers have been employed in order to form the 2-D images of the measured nonlinear scatterers in this study. All formed 2-D nonlinear scatterers images have been compared regarding resolution, localization, and focusing properties.

According to the experimental studies, Capon-based algorithms are superior to that of Delay and Sum algorithms in terms of resolution, amplitude distribution, and localization parameters. On the other hand, the Capon-based beamformers fall behind compared to real-time applications due to the extensive computational requirement. Within the scope of this thesis, an algorithm that forms a nonlinear

scatterer image close to the image formation speed of the Delay and Sum algorithm and the performance of the Capon algorithm has been studied. A neural network-based beamformer structure, which has made a considerable breakthrough in this field in recent years, has provided significant gains in terms of performance. The radial basis neural network (RBFNN) beamformer structure offers an unprecedented advantage in 2-D nonlinear scatterer image formation studies. The RBFNN-based beamformer structure developed in this study has been trained with standard and robust capon algorithms and compared with its conventional counterparts. As can be seen from the results, very close results have been obtained regarding performance criteria for conventional beamformer structures. On the other hand, when the image formation times are analyzed, the RBFNN structure trained with standard capon, RBFNN-SCB, has shown almost identical to its conventional counterpart. The RBFNN beamformer algorithm trained with robust capon, RBFNN-RCB, provided an average speedup of 100 times in all measurement scenarios. This thesis obtained a beamformer structure close to the DSB algorithm regarding image formation times and close to the RCB algorithm regarding resolution, localization, and focusing criteria. These results indicate that a neural network-based beamforming approach could be applied to form an image of NLS.

As a result, an in-depth analysis of microwave imaging in the near-field region for nonlinear scatterers have been conducted by employing a narrowband single-tone harmonic beamformer measurement radar system. The study comprehensively covers the theoretical background of the HBF microwave imaging system and experimental results. Three conventional and two neural network-based beamformer techniques have been investigated, developed, and employed to form 2-D microwave images of nonlinear scatterers in given scenarios. The findings from this research show that the developed HBF measurement system, conventional and RBFNN-based beamforming algorithms have a promising potential in 2-D microwave imaging of nonlinear scatterers.

In this study, all experimental studies were carried out in free space. In order to investigate the medium effects, the nonlinear scatterers need to be inserted or placed behind the dielectric medium (wall etc.) in the near field of the beamforming system.

The 2-D HBF measurement system needs to be investigated. This thesis limited its scope to a 1-D scanning system. Therefore, there is a need to investigate the potential benefits and insights gained from adding y-axis scanning in harmonic microwave imaging studies.

Various neural network structures like CNN could improve the results of the RBFNN-based beamforming algorithm. It needs to be investigated.

The virtual array technique could be implemented to get a wider scanning area without implementing additional hardware, higher azimuth/elevation resolution, and enhanced image formation capabilities. Furthermore, the compressed sensing technique could also be implemented to get high-resolution images from limited or incomplete data sets.

REFERENCES

[1] M. S. Siderhurst, K. M. Murman, K. T. Kaye, M. S. Wallace, M. F. Cooperband, "Radio telemetry and harmonic radar tracking of the spotted lanternfly, lycorma delicatula (white) (hemiptera: Fulgoridae)," *Insects*, vol. 15, 1 Jan. 2024, issn: 20754450. doi: 10.3390/insects15010017.

[2] R. Ala, C. D. Rouse, B. G. Colpitts, "An extra low-mass harmonic radar transponder for insect tracking applications," *IEEE Transactions on Radar Systems*, vol. 1, pp. 146–154, 2023. doi: 10.1109/TRS.2023.3286270.

[3] L. Chioukh, H. Boutayeb, D. Deslandes, K. Wu, "Noise and sensitivity of harmonic radar architecture for remote sensing and detection of vital signs," *IEEE Transactions on Microwave Theory and Techniques*, vol. 62, pp. 1847–1855, 9 Sep. 2014, issn: 0018-9480. doi: 10.1109/TMTT.2014.2343934.

[4] B. Kubina, J. Romeu, C. Mandel, M. Schüßler, R. Jakoby, "Design of a quasi-chipless harmonic radar sensor for ambient temperature sensing," in *SENSORS, 2014 IEEE*, 2014, pp. 1567–1570. doi: 10.1109/ICSENS.2014.6985316.

[5] B. Kubina, J. Romeu, C. Mandel, M. Schüßler, R. Jakoby, "Quasi-chipless wireless temperature sensor based on harmonic radar," *Electronics Letters*, vol. 50, pp. 86–88, 2 Jan. 2014, issn: 0013-5194. doi: 10.1049/el.2013.3061.

[6] V. V. Bereka, V. V. Rudenko, O. V. Zayets, O. Pastushenko, "Radar method for the remote monitoring of the corrosion state of reinforced-concrete structures," *Materials Science*, vol. 58, pp. 54–60, 1 Jul. 2022, issn: 1068-820X. doi: 10.1007/s11003-022-00630-w.

[7] T. Harzheim, M. Mühmel, H. Heuermann, "A sfcw harmonic radar system for maritime search and rescue using passive and active tags," *International Journal of Microwave and Wireless Technologies*, vol. 13, pp. 691–707, 7 2021, issn: 1759-0787. doi: 10.1017/S1759078721000520.

[8] H. Heuermann, T. Harzheim, M. Muhmel, "A maritime harmonic radar search and rescue system using passive and active tags," in *2020 17th European Radar Conference (EuRAD)*, IEEE, Jan. 2021, pp. 73–76, isbn: 978-2-87487-061-3. doi: 10.1109/EuRAD48048.2021.00030.

[9] H. Aniktar, D. Baran, E. Karav, E. Akkaya, Y. S. Birecik, M. Sezgin, "Getting the bugs out: A portable harmonic radar system for electronic countersurveillance applications," *IEEE Microwave Magazine*, vol. 16, pp. 40–52, 10 2015, issn: 1557-9581. doi: 10.1109/MMM.2015.2465591.

[10] J. Shefer, R. J. Klensch, "Harmonic radar helps autos avoid collisions," *IEEE Spectrum*, vol. 10, pp. 38–45, 5 1973. doi: 10.1109/MSPEC.1973.5217022.

[11] G. J. Mazzaro, A. F. Martone, "Multitone harmonic radar," in *Proc. SPIE*, vol. 8714, May 2013, 87140E. doi: 10.1117/12.2014241.

[12] G. J. Mazzaro, A. F. Martone, D. M. McNamara, "Detection of rf electronics by multitone harmonic radar," *IEEE Transactions on Aerospace and Electronic Systems*, vol. 50, pp. 477–490, 1 2014, issn: 1557-9603. doi: 10.1109/TAES.2013.120798.

[13] G. J. Mazzaro, K. A. Gallagher, A. F. Martone, K. D. Sherbondy, R. M. Narayanan, "Short-range harmonic radar: Chirp waveform, electronic targets," in *Proc.SPIE*, vol. 9461, May 2015, p. 946 108. doi: 10.1117/12.2177311.

[14] G. J. Mazzaro, K. A. Gallagher, A. R. Owens, K. D. Sherbondy, R. M. Narayanan, *Ultra-wideband harmonic radar for locating radio-frequency electronics*, 2015.

[15] T. Berger, S.-E. Hamran, "Harmonic synthetic aperture radar processing," *IEEE Geoscience and Remote Sensing Letters*, vol. 12, pp. 2066–2069, 10 Oct. 2015, issn: 1545-598X. doi: 10.1109/LGRS.2015.2447517.

[16] F. Bischeltsrieder, E. Schreiber, M. Peichl, A. Heinzel, M. Jirousek, "High resolution harmonic radar imaging for safety and security applications," in *Radar Sensor Technology XXIII*, SPIE, May 2019, p. 16, isbn: 9781510626713. doi: 10.1117/12.2518589.

[17] Z. Shi, J. Yi, Z. Gong, X. Wan, "A spatial variation compensation imaging algorithm for harmonic sar," *IEEE Transactions on Geoscience and Remote Sensing*, vol. 61, pp. 1–14, 2023, issn: 1558-0644. doi: 10.1109/TGRS.2023.3268318.

[18] K. A. Gallagher, R. M. Narayanan, G. J. Mazzaro, A. F. Martone, K. D. Sherbondy, "Static and moving target imaging using harmonic radar," *Electronics*, vol. 6, 2 2017, issn: 2079-9292. doi: 10.3390/electronics6020030.

[19] C. Hilton, J. A. Nanzer, "Narrowband passive rf tags for frequency-selective harmonic doppler radar tracking," *IEEE Transactions on Antennas and Propagation*, vol. 71, pp. 1216–1222, 2 2023, issn: 1558-2221. doi: 10.1109/TAP.2022.3220489.

[20] H. Ilbegi, H. T. Hayvaci, I. S. Yetik, A. E. Yilmaz, "Distinguishing electronic devices using harmonic radar," in *2017 IEEE Radar Conference (RadarConf)*, IEEE, May 2017, pp. 1527–1530, isbn: 978-1-4673-8823-8. doi: 10.1109/RADAR.2017.7944449.

[21] O. J. Ragira, "Design of radar to detect a target at an arbitrary standoff range," *International Journal of Engineering Trends and Technology*, vol. 46, 2017, issn: 2231-5381. doi: 10.14445/22315381/IJETT-V46P265.

[22] A. Mishra, C. Li, "A third-order harmonic radar design for mm-wave frequencies," in *Radar Sensor Technology XXV*, vol. 11742, SPIE, 2021, 117421A. doi: 10.1117/12.2586111.

[23] S. Y. Oh, K. H. Cha, H. Hong, H. Park, S. K. Hong, "Measurement of nonlinear rcs of electronic targets for nonlinear detection," *J. Electromagn. Eng. Sci*, vol. 22, pp. 447–451, 4 2022. doi: 10.26866/jees.2022.4.r.108.

[24] K. A. Gallagher, "Harmonic radar: Theory and applications to nonlinear target detection, tracking, imaging, and classification," Dept. Elect. Eng., Ph.D. dissertation, Penn State University, State College, PA, 2015.

[25] K. A. Gallagher, G. J. Mazzaro, A. F. Martone, K. D. Sherbondy, R. M. Narayanan, "Derivation and validation of the nonlinear radar range equation," vol. 9829, SPIE, 2016, 98290P. doi: 10.1117/12.2224478.

[26] O. Ari, A. Kizilay, "Broadband all-metal vivaldi antenna with rexolite inserted slot edge," *Microwave and Optical Technology Letters*, vol. 64, pp. 778–788, 4 2022. doi: 10.1002/mop.33177.

[27] P. J. Beasley, M. A. Ritchie, "Bladerad: Development of an active and passive, multistatic enabled, radar system," in *2021 18th European Radar Conference (EuRAD)*, 2022, pp. 98–101. doi: 10.23919/EuRAD50154.2022.9784498.

[28] Nuand, *Bladerf 2.0 micro*, [Online]. Available: https://www.nuand.com/bladerf-2-0-micro/ [Accessed: 2024], 2018.

[29] J. W. Bowen, "Astigmatism in tapered slot antennas," *International Journal of Infrared and Millimeter Waves*, vol. 16, pp. 1733–1756, 10 1995, issn: 1572-9559. doi: 10.1007/BF02068685.

[30] E. W. Reid, L. Ortiz-Balbuena, A. Ghadiri, K. Moez, "A 324-element vivaldi antenna array for radio astronomy instrumentation," *IEEE Transactions on Instrumentation and Measurement*, vol. 61, pp. 241–250, 1 2012. doi: 10.1109/TIM.2011.2159414.

[31] I.-S. Kim, C.-H. Lee, S.-Y. Choi, J.-Y. Kim, "Single-polarized wideband array antenna of all-metal structure with modified tsa elements," *Microwave and Optical Technology Letters*, vol. 59, pp. 2445–2449, 10 2017. doi: https://doi.org/10.1002/mop.30753.

[32] R. Corporation, *Microwave impedance calculator*, https://rogerscorp.com/blog/2020/new-online-microwave-impedance-calculator, [Online; accessed October 2020], 2020.

[33] X.-Q. Li, Q.-X. Liu, X.-J. Wu, L. Zhao, J.-Q. Zhang, Z.-Q. Zhang, "A gw level high-power radial line helical array antenna," *IEEE Transactions on Antennas and Propagation*, vol. 56, pp. 2943–2948, 9 2008. doi: 10.1109/TAP.2008.928781.

[34] F. Paschen, "Ueber die zum funkenübergang in luft, wasserstoff und kohlensäure bei verschiedenen drucken erforderliche potentialdifferenz," *Annalen der Physik*, vol. 273, pp. 69–96, 5 1889. doi: https://doi.org/10.1002/andp.18892730505. [Online]. Available: https://onlinelibrary.wiley.com/doi/abs/10.1002/andp.18892730505.

[35] R. W. Kindt, W. R. Pickles, "Ultrawideband all-metal flared-notch array radiator," *IEEE Transactions on Antennas and Propagation*, vol. 58, pp. 3568–3575, 11 2010. doi: 10.1109/TAP.2010.2071360.

[36] E. G. Tianang, M. A. Elmansouri, D. S. Filipovic, "Ultra-wideband lossless cavity-backed vivaldi antenna," *IEEE Transactions on Antennas and Propagation*, vol. 66, pp. 115–124, 1 2018. doi: 10.1109/TAP.2017.2775286.

[37] C. L. Prasanna, M. B. Lakshmi, N. N. Sastry, "A parametric analysis & design of all metal vivaldi antenna covering 3.0-18 ghz for df and phased array applications," *Progress In Electromagnetics Research C*, vol. 92, pp. 57–69, 2019. doi: 10.2528/PIERC19020601.

[38] M. Moosazadeh, S. Kharkovsky, J. T. Case, B. Samali, "Antipodal vivaldi antenna with improved radiation characteristics for civil engineering applications," *IET Microwaves, Antennas & Propagation*, vol. 11, pp. 796–803, 6 2017. doi: https://doi.org/10.1049/iet-map.2016.0720.

[39] H. Sato, Y. Takagi, K. Sawaya, "High gain antipodal fermi antenna with low cross polarization," *IEICE Transactions on Communications*, vol. E94.B, pp. 2292–2297, 8 2011. doi: 10.1587/transcom.E94.B.2292.

[40] S. Pan, W. Shen, Y. Feng, Z. Liu, P. Xiao, G. Li, "Miniaturization and performance enhancement of vivaldi antenna based on ultra-wideband metasurface lens," *AEU - International Journal of Electronics and Communications*, vol. 134, p. 153 703, 2021, issn: 1434-8411. doi: https://doi.org/10.1016/j.aeue.2021.153703.

[41] A. Molaei, M. Kaboli, S. A. Mirtaheri, M. S. Abrishamian, "Dielectric lens balanced antipodal vivaldi antenna with low cross-polarisation for ultra-wideband applications," *IET Microwaves, Antennas & Propagation*, vol. 8, pp. 1137–1142, 14 2014. doi: https://doi.org/10.1049/iet-map.2014.0207.

[42] J. Wu, Z. Zhao, Q.-H. Liu, "A novel vivaldi antenna with extended ground plane stubs for ultrawideband applications," *Microwave and Optical Technology Letters*, vol. 57, pp. 983–987, 4 2015. doi: https://doi.org/10.1002/mop.28955.

[43] R. Natarajan, J. V. George, M. Kanagasabai, A. K. Shrivastav, "A compact antipodal vivaldi antenna for uwb applications," *IEEE Antennas and Wireless Propagation Letters*, vol. 14, pp. 1557–1560, 2015. doi: 10.1109/LAWP.2015.2412255.

[44] L. Juan, F. Guang, Y. Lin, F. Demin, "A modified balanced antipodal vivaldi antenna with improved radiation characteristics," *Microwave and Optical Technology Letters*, vol. 55, pp. 1321–1325, 6 2013. doi: https://doi.org/10.1002/mop.27558.

[45] T. H. Lim, S. Park, C. S. Lee, J.-R. Park, H. Choo, "A broadband dual-slant polarized metal vivaldi antenna for a high-power jammer," in *2020 International Symposium on Antennas and Propagation (ISAP)*, IEEE, Jan. 2021, pp. 485–486, isbn: 978-4-88552-326-7. doi: 10.23919/ISAP47053.2021.9391471.

[46] Z. Wang, J. Yi, Z. Gong, X. Wan, "Mechanism and characteristic of nonlinear clutter in harmonic radar with frequency-modulated waveform," *IEEE Transactions on Aerospace and Electronic Systems*, vol. 59, pp. 4240–4249, 4 2023, issn: 1557-9603. doi: 10.1109/TAES.2023.3237659.

[47] X. Lan, *Beamforming and Direction of Arrival Estimation Based on Vector Sensor Arrays*. University of Sheffield, 2019. [Online]. Available: https://books.google.com.tr/books?id=gN4aywEACAAJ.

[48] H. Cox, R. Zeskind, M. Owen, "Robust adaptive beamforming," *IEEE Transactions on Acoustics, Speech, and Signal Processing*, vol. 35, no. 10, pp. 1365–1376, 1987. doi: 10.1109/TASSP.1987.1165054.

[49] L. R. Fuchs, A. Maki, A. Gällström, "Optimization method for wide beam sonar transmit beamforming," *Sensors*, vol. 22, p. 7526, 19 Oct. 2022, issn: 1424-8220. doi: 10.3390/s22197526.

[50] N. S. N. Anwar, M. Z. Abdullah, "Clutter suppression in through-the-wall radar imaging using enhanced delay-and-sum beamformer," in *2014 IEEE International Conference on Imaging Systems and Techniques (IST) Proceedings*, IEEE, Oct. 2014, pp. 179–183, isbn: 978-1-4799-5220-5. doi: 10.1109/IST.2014.6958469.

[51] T. Reimer, M. Solis-Nepote, S. Pistorius, "The application of an iterative structure to the delay-and-sum and the delay-multiply-and-sum beamformers in breast microwave imaging," *Diagnostics*, vol. 10, p. 411, 6 Jun. 2020, issn: 2075-4418. doi: 10.3390/diagnostics10060411.

[52] D. Byrne, I. J. Craddock, "Time-domain wideband adaptive beamforming for radar breast imaging," *IEEE Transactions on Antennas and Propagation*, vol. 63, pp. 1725–1735, 4 Apr. 2015, issn: 0018-926X. doi: 10.1109/TAP.2015.2398125.

[53] T. S. Kiong, S. B. Salem, J. K. S. Paw, K. P. Sankar, S. Darzi, "Minimum variance distortionless response beamformer with enhanced nulling level control via dynamic mutated artificial immune system," *The Scientific World Journal*, vol. 2014, p. 164 053, 2014, issn: 2356-6140. doi: 10.1155/2014/164053. [Online]. Available: https://doi.org/10.1155/2014/164053.

[54] J. Li, P. Stoica, Z. Wang, "On robust capon beamforming and diagonal loading," *IEEE Transactions on Signal Processing*, vol. 51, pp. 1702–1715, 7 2003. doi: 10.1109/TSP.2003.812831.

[55] P. Stoica, Z. Wang, J. Li, "Robust capon beamforming," in *Conference Record of the Thirty-Sixth Asilomar Conference on Signals, Systems and Computers, 2002.*, vol. 1, 2002, 876–880 vol.1. doi: 10.1109/ACSSC.2002.1197303.

[56] S. Çaylar, "A novel neural network based approach for direction of arrival estimation," Ph.D. dissertation, Middle East Technical University, 2007.

[57] H. L. Southall, J. A. Simmers, T. H. O'Donnell, "Direction finding in phased arrays with a neural network beamformer," *IEEE Transactions on Antennas and Propagation*, vol. 43, pp. 1369–1374, 12 1995, issn: 1558-2221. doi: 10.1109/8.475924.

[58] A. H. E. Zooghby, C. G. Christodoulou, M. Georgiopoulos, "Performance of radial-basis function networks for direction of arrival estimation with antenna arrays," *IEEE Transactions on Antennas and Propagation*, vol. 45, pp. 1611–1617, 11 1997, issn: 1558-2221. doi: 10.1109/8.650072.

[59] A. H. E. Zooghby, C. G. Christodoulou, M. Georgiopoulos, "A neural network-based smart antenna for multiple source tracking," *IEEE Transactions on Antennas and Propagation*, vol. 48, pp. 768–776, 5 2000. doi: 10.1109/8.855496.

[60] T. Sallam, A. B. Abdel-Rahman, M. Alghoniemy, Z. Kawasaki, T. Ushio, "A neural-network-based beamformer for phased array weather radar," *IEEE Transactions on Geoscience and Remote Sensing*, vol. 54, pp. 5095–5104, 9 2016, issn: 1558-0644. doi: 10.1109/TGRS.2016.2554116.

[61] T. Sallam, A. M. Attiya, "Convolutional neural network for 2d adaptive beamforming of phased array antennas with robustness to array imperfections," *International Journal of Microwave and Wireless Technologies*, vol. 13, pp. 1096–1102, 10 2021, issn: 1759-0787. doi: DOI : 10 . 1017 / S1759078721001070. [Online]. Available: https : / / www . cambridge . org / core / product / AE904B5D3851864A5C4E22A879C50119.

[62] K.-L. Du, K. Cheng, M. Swamy, "A fast neural beamformer for antenna arrays," in *2002 IEEE International Conference on Communications. Conference Proceedings. ICC 2002*, IEEE, pp. 139–144, isbn: 0-7803-7400-2. doi: 10.1109/ICC.2002.996833.

PUBLICATIONS FROM THE THESIS

Papers

1. Ari, O, Kizilay, A. Broadband all-metal Vivaldi antenna with Rexolite inserted slot edge. Microw Opt Technol Lett. 2022; 778-788. doi:10.1002/mop.33177

2. Utku, C., Ari, O, Kizilay, A., "Near-Field Through-the-Wall Harmonic Radar Imaging of Nonlinear Scatterers" *IEEE Access*, Access-2024-12151, submitted.